MUTUAL COUPLING COMPENSATED MULTIBAND LINEAR ANTENNA ARRAYS FOR RADIO FREQUENCY ENERGY HARVESTING/TRANSMITTING

A Thesis

by

CHAO-HSIUAN TSAY

Submitted to the Office of Graduate and Professional Studies of
Texas A&M University
in partial fulfillment of the requirements for the degree of

MASTER OF SCIENCE

Chair of Committee,	Edgar Sánchez-Sinencio
Co-Chairs of Committee,	Kamran Entesari
Committee Members,	Pao-Tai Lin
	Je-Chin Han
Head of Department,	Miroslav Begovic

August 2017

Major Subject: Electrical Engineering

Copyright 2017 Chao-Hsiuan Tsay

ABSTRACT

RF energy transmitting is an approach to deliver charging energy wirelessly, while RF energy harvesting is an approach to re-charge battery by capturing ambient RF energy. A multiband system composed of mutual coupling compensated linear antenna arrays and output LC matched RF-DC rectifier is proposed for RF energy harvesting and transmitting. The designed system operates in standard communication bands such as GSM850, GSM900, GSM1800, GSM1900, WiFi, Bluetooth, and LTE since ample RF ambient signals are present and numerous IoT sensors operates in these frequency bands.

The design starts from a highly efficient double-ring monopole antenna. The proposed antenna has both wideband and multiband features to cover the target operating frequencies. According to Friis transmission equation, the captured/radiated RF power is proportional to the antenna gain, thus antenna array composed of double-ring monopoles is investigated to increase antenna gain. In the proposed four-element antenna array, a four-way RF energy combiner with optimum power combining efficiency is implemented to connect four antennas. Triple-band radiation patterns are synthesized by by mutual coupling compensation structure. The proposed output LC matched RF-DC rectifier is connected to antenna array to convert RF power to DC energy. The rectifier sensitivity and power conversion efficiency is boosted with dual frequency tones.

System measurement results state that not only the antenna gain but also the radiation pattern of antenna array affects the total captured RF power. Antenna array is preferable to be installed at the transmitting side for RF energy transfer, while the single antenna is preferable to be installed at the receiving side for RF energy harvesting. If the receiving area is not limited, then the rectenna array composed of antenna arrays and RF-DC rectifiers can be applied for RF energy harvesting.

DEDICATION

感謝父母不間斷的經濟支持, 感謝妹妹的鼓勵,

感謝叔叔和嬸嬸平常的關心, 感謝爺爺奶奶對我的驕傲,

感謝我老婆及娘家無條件的疼愛與照顧,

最後要感謝所有默默幫助我的好朋友和前輩們,

這本論文的文字背後, 是您們點點滴滴的支持

ACKNOWLEDGMENTS

I will not be able to complete my graduate study without many people's supports. First of all, I would like to thank my advisor, Dr. Edgar Sánchez-Sinencio, for his immeasurable passion and limitless creativity in research. I always remind myself to work harder and embrace challenges without hesitation like him. I am very honored that I can join Dr. Sánchez's research group and have the opportunity to take all courses from Dr. Sánchez.

I would also like to thank my co-advisor, Dr. Kamran Entesari, for all detailed technical advice and comprehensive paper revisions from him. Dr. Entesari's rigorous reasoning polishes my skills to professionally compose manuscripts and logically present results. I had read Dr. Entesari's papers before I came to Texas A&M, and I cannot imagine that one day I will hold biweekly meetings with him and Dr. Sánchez.

My committee members, Dr. Pao-Tai Lin and Dr. Je-Chin Han, generously give me their hands whenever I face problems. It is very touching that Dr. Lin and Dr. Han always put students to the highest priority. I would also like to thank Dr. Jerald Caton for his interest in my final defense.

Moreover, I am truly grateful to Dr. Gregory Huff and Steven Yeh for precious chamber access and continual supports on time-consuming radiation pattern measurements. Their unconditional assistants make this thesis possible.

I may not be able to smoothly pass graduate study without all my friends in analog and mixed signal group for incisive academic discussions and innovative research feedback, especially Ali Pourghorban Saghati, Dr. Mohamed A. Abouzied, and Zizhen Zeng in my submitted TMTT author list.

Finally, I would like to thank my family and my wife's family, to be at my side in sickness and in health, in good times and in bad, and in sorrow as well as in joy.

CONTRIBUTORS AND FUNDING SOURCES

Contributors

Part 1, faculty committee recognition

This work was supported by a thesis (or) dissertation committee consisting of Professor Edgar Sánchez-Sinencio [advisor], Kamran Entesari [co-advisor], and Pao-Tai Lin of the Department of Electrical & Computer Engineering and Professor Je-Chin Han of the Department of Mechanical Engineering.

The research aspect and entire cost were conducted by Professor Edgar Sánchez-Sinencio. The design methodology depicted in Chapter 2 and Chapter 4 were advised by Professor Kamran Entesari.

Part 2, student/collaborator contributions

The simulation and layout for Chapter 2 were instructed by Ali Pourghorban Saghati. The radiation patterns measured for Chapter 2 and Chapter 4 were conducted by Steven Yeh. The efficiency measurement for Chapter 3 and the system measurement for Chapter 6 were assisted by Zizhen Zeng.

All other work conducted for the thesis (or) dissertation was completed by the student independently.

Funding Sources

Graduate study was supported by Texas Public Education Grant International from Texas A&M University, Departmental Graduate Merit Scholarship from Texas A&M University, Excellence Fund for Analog Design and Engineering from Texas Instruments, Graduate Assistant Teaching from Texas A&M University, and funding from my family.

TABLE OF CONTENTS

Page

ABSTRACT ii

DEDICATION iii

ACKNOWLEDGMENTS iv

CONTRIBUTORS AND FUNDING SOURCES v

TABLE OF CONTENTS vi

LIST OF FIGURES viii

LIST OF TABLES xiii

1. INTRODUCTION 1

1.1 Radio Frequency (RF) Energy Harvesting/Transfer Technique 1
1.1.1 RF Energy Harvesting 1
1.1.2 RF Energy Transfer 3
1.2 Proposed Solution 4

2. A COMPACT MULTIBAND DOUBLE-RING MONOPOLE ANTENNA . . . 6

2.1 Introduction 6
2.2 Multiband Monopole Antenna Design 7
2.3 Fabrication and Experimental Results 14
2.4 Conclusions 18

3. A FOUR-WAY BROADBAND RF ENERGY COMBINER 20

3.1 Introduction 20
3.2 Conventional Power Combiners 21
3.2.1 Wilkinson Power Combiner 21
3.2.2 Rat-Race Coupler 26
3.2.3 Performance Comparison 28
3.3 Proposed Four-Way Broadband RF Energy Combiner 30
3.4 Fabrication and Experimental Results 36
3.5 Conclusions 39

4. MUTUAL COUPLING COMPENSATED MULTIBAND LINEAR ANTENNA ARRAYS OF DOUBLE-RING MONOPOLES 40

4.1 Introduction 40
4.2 Mutual Coupling Compensated Linear Antenna Array of Two Double-Ring Monopoles 43
4.2.1 Mutual Coupling Compensation 43
4.2.2 Effective Directivity 46
4.2.3 Return Loss Matching 48
4.2.4 Radiation Patterns 51
4.3 Mutual Coupling Compensated Linear Antenna Array of Four Double-Ring Monopoles 53
4.3.1 Mutual Coupling Compensation 53
4.3.2 Effective Directivity 56
4.3.3 Return Loss Matching 57
4.3.4 Radiation Patterns 60
4.4 Fabrication and Experimental Results 62
4.5 Conclusions 68

5. A SIX-STAGE TRIPLE-BAND AND WIDEBAND RF-DC RECTIFIER . . . 69

5.1 Circuit Design 69
5.2 Fabrication and Measurement Results 74
5.3 Conclusions 78

6. DEMONSTRATION OF MULTIBAND RF ENERGY HARVESTING AND TRANSFER 79

6.1 Experimental Results 79
6.2 Conclusions 85

7. SUMMARY AND FUTURE WORK 86

REFERENCES 88

LIST OF FIGURES

FIGURE Page

1.1 RF energy harvesting overview. 1

1.2 Adapted from [1] ambient RF source availability. 2

1.3 (a) Bridge is in normal condition, and (b) bridge is damaged. 3

1.4 RF energy transfer overview. 3

1.5 Diagram of a multiband RF energy harvesting system. 5

2.1 Design consideration of an antenna. 7

2.2 (a) Rectangular patch antenna, (b) dipole antenna, and (c) circular monopole antenna. 8

2.3 Return loss (S_{11}) bandwidth comparison of typical patch, dipole, and monopole antenna. 9

2.4 (a) Circular monopole, and (b) annular ring monopole. 10

2.5 (a) return loss bandwidth, and (b) efficiency of the annular ring monopole at 870-MHz resonance. 11

2.6 (a) double-ring monopole, (b) proposed double-ring monopole with notched ground. 12

2.7 Input return loss comparison. 12

2.8 (a) Top view and (b) $A-A'$ cross section view of the proposed double-ring monopole antenna, and (c) photograph of the fabricated antenna. 13

2.9 Simulated surface current distribution at (a) 870 MHz, (b) 1.8 GHz, and (c) 2.44 GHz. 14

2.10 Simulated and measured return loss. 15

2.11 Normalized measured H-plane and simulated E-plane radiation patterns at 880 MHz, 1.7 GHz, and 2.44 GHz 16

3.1 Diagram of a RF energy harvesting system with (a) a DC energy combiner, and (b) a RF energy combiner. 21

3.2 Diagram of a two-way power combiner. 22

3.3 Schematic of (a) a two-way Wilkinson power combiner, and (b) a two-way broadband Wilkinson power combiner. 23

3.4 Layout of (a) a two-way Wilkinson power combiner, and (b) a two-way broadband Wilkinson power combiner. 25

3.5 (a) schematic and (b) layout of a rat-race coupler. 26

3.6 Antenna array with a Wilkinson type power combiner. 27

3.7 Antenna array with a rat-race type power combiner. 27

3.8 Comparison of (a) return loss at output port and (b) return loss at input port in different power combiners. 28

3.9 Comparison of (a) isolation between input ports, and (b) phase imbalance at output port in different power combiners. 29

3.10 Comparison of power combining efficiency in different power combiners. 30

3.11 Adapted from [3] schematic of the four-way Wilkinson power divider by interconnecting three two-way Wilkinson power dividers 31

3.12 Structure of the proposed four-way broadband RF energy combiner. . . . 33

3.13 Layout with $\theta = \pi/2$ and (a) $(N_1,\ N_2) = (1,\ 1)$, (b) $(N_1,\ N_2) = (1,\ 4)$, (c) $(N_1,\ N_2) = (4,\ 1)$, and (d) $(N_1,\ N_2) = (4,\ 4)$. 33

3.14 Efficiency simulation results with $\theta = \pi/2$. 34

3.15 (a) S_{11}, (b) S_{22}, (c) S_{23}, and (d) S_{24} simulation results with $\theta = \pi/2$. . . . 34

3.16 Layout with $(N_1,\ N_2) = (1,\ 4)$ and (a) $\theta = \pi/6$, (b) $\theta = \pi/2$, and (c) $\theta = \pi$. 35

3.17 Efficiency simulation results with $(N_1,\ N_2) = (1,\ 4)$. 35

3.18 (a) Schematic, and (b) photograph of the fabricated four-way broadband RF energy combiner. 37

3.19 (a) Output return loss, (b) input return loss, (c) insertion loss between input and output ports, (d) isolation between adjacent input ports, (e) isolation between non-adjacent input ports, and (f) efficiency of the proposed four-way RF energy combiner. 38

4.1 Antenna array of two double-ring monopoles (a) without ground baffle, and (b) with ground baffle. 43

4.2 Insertion loss (S_{12}) of array of two double-ring monopoles. (D=120 mm, and E=10 mm) 44

4.3 Directivity of array of two double-ring monopoles (a) without ground baffle, and (b) with ground baffle at 860, 1800, and 2440 MHz. (E=10 mm) . 45

4.4 Return loss (S_{11}) of array of two double-ring monopoles. (D=120 mm, and E=10 mm) 46

4.5 (a) return loss (S_{11}) and (b) directivity at 2440 MHz operating frequency of array of two double-ring monopoles with ground baffle. (D=120 mm) . 46

4.6 Additional transmission line due to different antenna spacing. 47

4.7 Effective directivity versus antenna spacing of array of two double-ring monopoles with ground baffle. (E=10 mm) 48

4.8 Schematic of the proposed two-way multiband matching network. 49

4.9 Layout of the proposed array of two double-ring monopoles. 49

4.10 Return loss matching flow in (a) 820−920 MHz, (b) 1.7−1.9 GHz, and (c) 2.40−2.48 GHz frequency ranges 50

4.11 Return loss of the proposed array of two double-ring monopoles. 50

4.12 Realized gain at 860 MHz in (a) XZ plane, (b) YZ plane, and (c) XY plane 52

4.13 Realized gain at 1800 MHz in (a) XZ plane, (b) YZ plane, and (c) XY plane 52

4.14 Realized gain at 2440 MHz in (a) XZ plane, (b) YZ plane, and (c) XY plane 52

4.15 Linear antenna array of four double-ring monopoles (a) without ground baffle, and (b) with ground baffle. 53

4.16 Insertion loss of four double-ring monopoles in a linear array at (a) port 1, and (b) port 2. (D=120 mm, and E=10 mm) 54

4.17 Return loss at port 1 and port 2 of four double-ring monopoles in a linear array. (D=120 mm) 55

4.18 Directivity difference between linear array of four double-ring monopoles with and without ground baffle. 56

4.19 Effective directivity of array of four double-ring monopoles with ground baffle. (E=10 mm) 57

4.20 Effective directivity of mutual coupling compensated arrays of two (n=2) and of four (n=4) double-ring monopoles. (E=10 mm) 57

4.21 Schematic of the proposed four-way multiband matching network. 58

4.22 Layout of the proposed linear array of four double-ring monopoles. 59

4.23 Return loss of the proposed array of four double-ring monopoles with multiband matching. 59

4.24 Realized gain at 860 MHz in (a) XZ plane, (b) YZ plane, and (c) XY plane 61

4.25 Realized gain at 1800 MHz in (a) XZ plane, (b) YZ plane, and (c) XY plane. 61

4.26 Realized gain at 2440 MHz in (a) XZ plane, (b) YZ plane, and (c) XY plane. 61

4.27 Photographs of (a) the proposed array of two elements, and (b) the proposed linear array of four elements. 62

4.28 Measured return loss of (a) the proposed array of two elements, and (b) the proposed linear array of four elements. 63

4.29 Normalized XZ-plane and YZ-plane radiation patterns of two-element array at 860 MHz, 1.8 GHz, and 2.44 GHz 65

4.30 Normalized XZ-plane and YZ-plane radiation patterns of four-element array at 860 MHz, 1.8 GHz, and 2.44 GHz 66

5.1 (a) Two-stage Dickson charge pump with LC matching, and (b) proposed Dickson charge pump topology with LC matching. 70

5.2 (a) Triple resonances design flow without C_2, and (b) comparison of triple resonances with and without C_2. 71

5.3 Schematic of the proposed six-stage triple-band and wideband RF-DC rectifier. 72

5.4 (a) Return loss, and (b) efficiency with and without matching. 73

5.5 (a) Layout, and (b) photograph of the fabricated rectifier. 74

5.6 (a) Measured return loss, and measured efficiency at (b) 860 MHz, (c) 1800 MHz, and (d)2440 MHz. 75

5.7 (a) Measured return loss, and measured efficiency at (b) 860 MHz, (c) 1800 MHz, and (d)2440 MHz. 76

6.1 Measurement setup. 80

LIST OF TABLES

TABLE Page

2.1 Performance comparison of typical antennas. 9

2.2 Geometries of the Proposed Double-Ring Monopole Antenna 13

2.3 Measured efficiency of the proposed antenna 17

2.4 Comparison of Related Works in Literature 18

3.1 Adapted from [4] normalized design parameters of the two-way broadband Wilkinson power combiner 23

3.2 Characteristic impedance and interconnecting resistor values of the Wilkinson and broadband Wilkinson power combiners. 25

3.3 Microstrip line width and length values of the Wilkinson and broadband Wilkinson power combiners. 25

3.4 Simulated 50Ω line loss on FR4 substrate. 32

3.5 Parameters of the proposed four-way RF energy combiner. 36

4.1 Parameters of the two-way multiband matching network. 49

4.2 Simulated performance of the proposed array of two double-ring monopoles. 51

4.3 Parameters of the four-way multiband matching network. 59

4.4 Simulated performance of the proposed array of four double-ring monopoles. 60

4.5 Realized Gain of Single Double-Ring Monopole, Array of Two Double-Ring Monopoles, and Linear Array of Four Double-Ring Monopoles . . . 67

4.6 Efficiency of Single Double-Ring Monopole, Array of Two Double-Ring Monopoles, and Linear Array of Four Double-Ring Monopoles 67

5.1 LC values of the 3-stage Dickson charge pump. 70

5.2 Component values of the proposed six-stage RF-DC rectifier. 74

5.3 Measured efficiency and sensitivity at V_{out} = 1 V. 77

6.1 Performance of RF Energy Harvesting/Transfer 81

6.2 Comparison with Previously Published Works 84

1. INTRODUCTION

1.1 Radio Frequency (RF) Energy Harvesting/Transfer Technique

According to the prediction in 2013 by Gartner [5], the number of Internet of Things (IoT) installed devices will grow to 26 billion units by 2020. Riding on the trend of IoT development, the importance of self-powering technique manifests itself due to the battery charging difficulty in the wireless IoT device.

1.1.1 RF Energy Harvesting

RF energy harvesting is an approach to re-charge battery by capturing ambient RF energy. Fig. 1.1 gives a brief overview of RF energy harvesting technique. In Fig. 1.1, the antenna harvests energy from various ambient RF signal sources, and the summed RF signal is converted to DC voltage through the RF rectifier. The converted DC voltage is regulated by the power management unit (PMU) and then delivered to power the IoT load. Recharge the battery by RF energy harvesting has been consolidated by the ambient RF spectrum measurement results [6, 1, 7]. Because ambient RF signals are mainly from the standard communication bands, the operating frequency of many RF energy harvesting works are below 3 GHz.

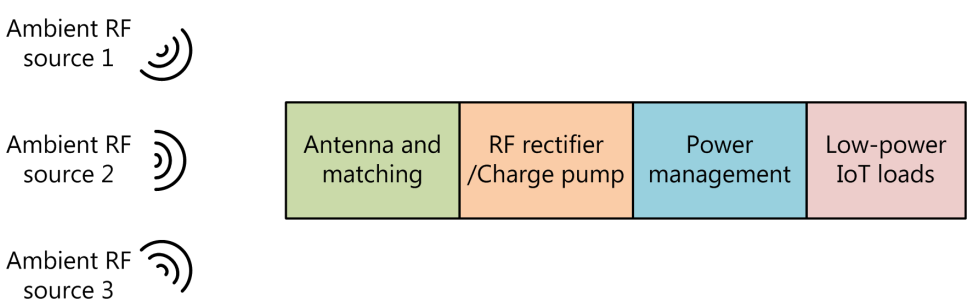

Figure 1.1: RF energy harvesting overview.

Fig. 1.2 adapted from [1] shows the measured ambient RF source availability. Digital TV signals locate in 470−692 MHz range, while mobile signals locates in more than one frequency bands with lowest frequency around 800 MHz. Power density from mobile signal is weaker than digital TV signal, but mobile antenna is at least 1.8 times compact than digital TV antenna. As a result, the works at Texas A&M University focus on mobile signals instead.

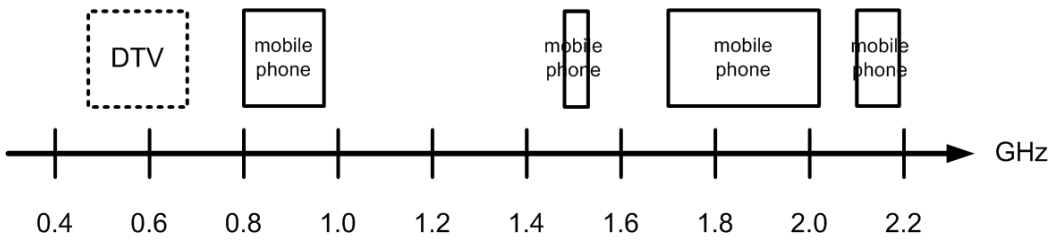

Figure 1.2: Adapted from [1] ambient RF source availability.

RF energy harvesting has numerous applications. One of the most well-known applications is to monitor the construction where it is hard to replace the battery, or is difficult or risky to access. Fig. 1.3 depicts the RF energy harvesting application on bridge monitoring. When the bridge is in normal condition as shown in Fig. 1.3a, the RF energy harvesting system is in sleeping mode and stores energy continuously. When the bridge is damaged as shown in Fig. 1.3b, the RF energy harvesting system is activated and sends out the information to the monitor center. This application requires vast amounts of sensors installed on the bridge, but it saves the labor cost and removes all wired networks. The charging speed from RF energy harvesting is usually very low (1−100 μW), but it is the continual power, and the system is normally turned-off or turned-on in a short period.

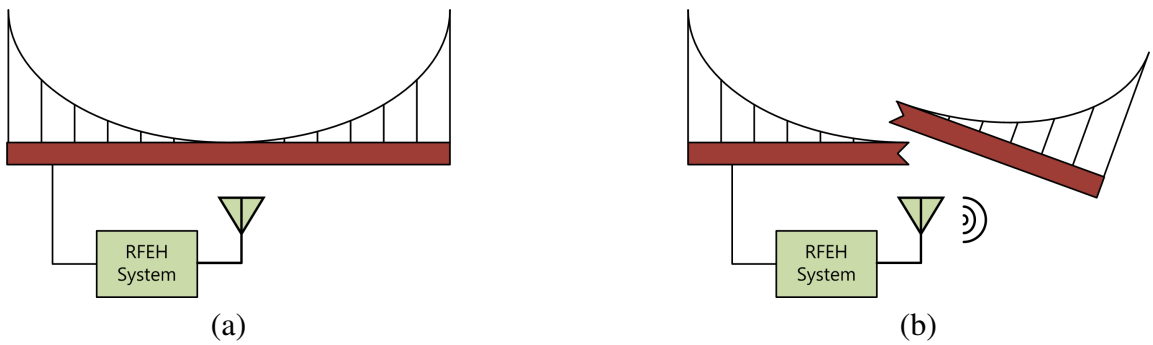

Figure 1.3: (a) Bridge is in normal condition, and (b) bridge is damaged.

1.1.2 RF Energy Transfer

RF energy transfer is an approach to deliver charging energy wirelessly [2]. Fig. 1.4 depicts the overview of RF energy transfer . A RF energy transmitter detects the location of each sensor and transmits the charging energy to the sensors whenever any sensor has low battery. In order to receive the charging energy from RF energy transmitter, each sensor must be equipped with RF energy harvesting function. As a result, the works at Texas A&M University focus on the entire energy flow from RF energy transmitter to local IoT sensors.

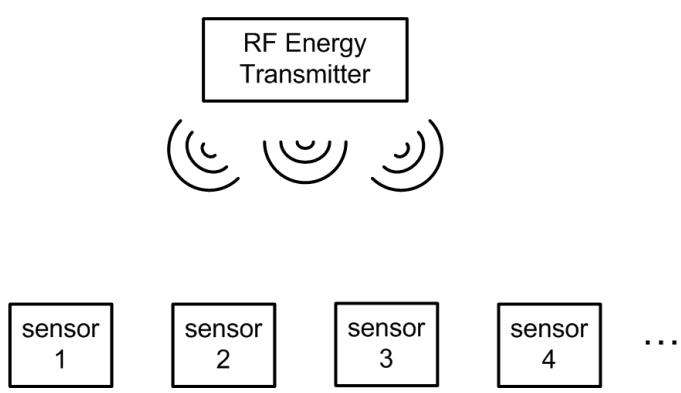

Figure 1.4: RF energy transfer overview.

1.2 Proposed Solution

Fig. 1.5 demonstrates the proposed multiband RF energy harvesting/transfer system. The main beam of antenna array is synthesized by antenna elements, and the direction of main beam is controlled by phase shifters. The beam steering control circuit adjusts the phase delay of each phase shifter to steer array main beam toward the desired direction. The receiver (RX) is used to sense the charging request signal from IoT sensors, while the transmitter chain (TX + OSC) is used to generate charging energy. The RF rectifier together with the power management unit (PMU) form the auxiliary system to take advantage of ambient RF energy sources. In RF energy transfer mode, the array beam is swept continuously by antenna array, phase shifters, and beam steering control circuit. When the charging request from IoT sensor is received and amplified by the receiver, the beam steering control circuit records the location of IoT sensor in terms of the particular phase delay of each phase shifter. The battery powers the oscillator to generate charging waveform, and the charging waveform is amplified through the transmitter. In the mean time the beam steering control circuit fixes the particular phase delay of each phase shifter to synthesize array beam toward the IoT sensor. The amplified charging waveform is then radiated by antenna array to charge IoT sensor. In RF energy harvesting mode, the array beam is steered for one time to identify the location with the strongest RF ambient energy by comparing the rectified voltage of RF rectifier in power management unit, then the array beam is synthesized toward the direction with the strongest RF ambient energy to recharge the battery. In [8], a zero DC power consumption IC composed of beam-steering control and phase shifters is proposed, which consolidates the development of the proposed RF energy harvesting/transfer system.

This thesis presents the implementation of antenna arrays, RF energy combiner, and RF rectifier for RF energy transfer/harvesting demonstration. All the proposed circuits are

designed on standard FR4 material ($\epsilon_r = 4.4$, $tan\delta = 0.021$), and the substrate thickness h is 1.6 mm. The future work will be the integration with phase shifter and beam steering control circuit.

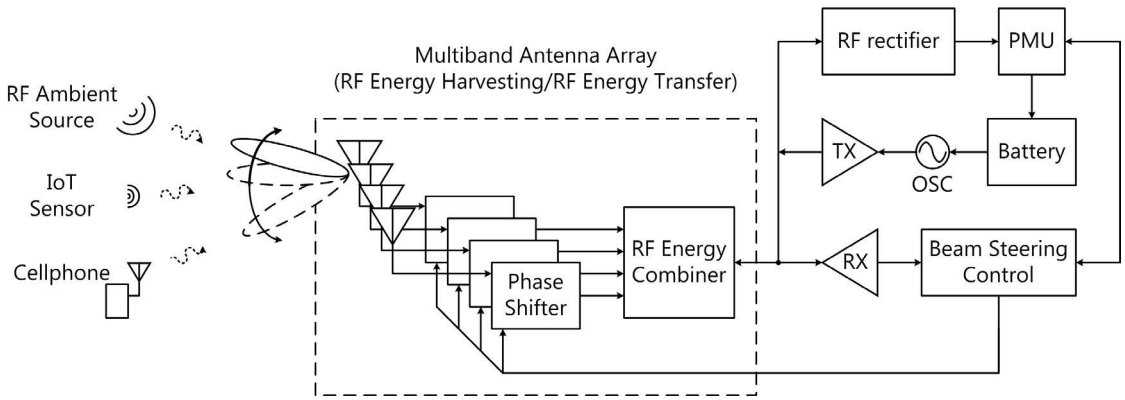

Figure 1.5: Diagram of a multiband RF energy harvesting system.

2. A COMPACT MULTIBAND DOUBLE-RING MONOPOLE ANTENNA

2.1 Introduction

The trend of RF energy harvesting antenna design is to achieve multiband and wideband features. It has been studied in [9, 10] that the harvested power will increase in a multitone environment. Because the ambient RF signal frequency is not a fixed value, the antenna bandwidth should cover all communication channels of interest. Several types of antennas have been investigated [10, 11, 12, 13, 14], but among various antenna topologies, monopole attracted more attentions due to the broader return loss bandwidth, stable omnidirectional radiation patterns, and compact size. In [10], a triple-band meandered monopole operating at 900, 1900 and 2400 MHz is proposed, but the return loss bandwidth is limited. In [11], a inkjet-printed wideband monopole on cardboard is presented with return loss bandwidth of 900 MHz, but the WiFi band is not included. In [12], a broadband bent triangular monopole with VSWR < 2 in 850 MHz$-$1.94 GHz range is developed, but the GSM850 and WiFi bands are not covered. In [15], a fractal monopole for WLAN and WiMAX function is proposed, and it might be re-designed for RF energy harvesting.

In this chapter, a highly efficient double-ring monopole antenna is proposed for multiband RF energy harvesting. To fully utilize the multitone environment, the proposed antenna has both wideband and multiband features to cover GSM850, GSM900, GSM1800, GSM1900, WiFi, Bluetooth, and LTE communication bands. Multiband feature is created by two annular rings, and wideband feature is inherent from the monopole topology. The design tradeoff of antenna geometry versus return loss bandwidth is investigated, and the total efficiency is preserved while achieving a compact size. The measurement results show return loss < -10 dB in 823$-$917 MHz and 1.26$-$3.09 GHz ranges with stable

omnidirectional radiation patterns and measured efficiency range of 76.7%−93.1%. Area miniaturization of 37% is achieved when compared to the conventional circular monopole with the same lower operating frequency.

2.2 Multiband Monopole Antenna Design

Antenna is the transducer to convert propagating waves in air to the guided waves on printed circuit board. Therefore, antenna is one of the most important components in a RF system. Performance and capability of the antenna directly determines the overall performance of a RF system. The design considerations of a energy harvesting antenna is demonstrated in Fig. 2.1. Assume $P_{incident}$ stands for the power incident to the antenna, and $P_{captured}$ stands for the power captured by the antenna, then the relationship between $P_{incident}$ and $P_{captured}$ is:

$$P_{captured} = P_{incident} \times (1 - S_{11}^2) \times \text{Eff}_{rad} \tag{2.1}$$

where S_{11} is the input reflection coefficient, Eff_{rad} is the radiation efficiency in %. In order to increase the power captured by the antenna, S_{11} must be minimized and Eff_{rad} must be maximized based on equation 2.1.

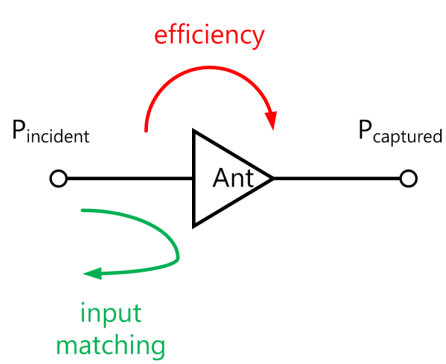

Figure 2.1: Design consideration of an antenna.

Fig. 2.2 shows three typical antennas: a rectangular patch antenna, a dipole antenna, and a circular monopole antenna. The corresponding input return loss simulation is shown in Fig. 2.3. As can be concluded from Fig. 2.3, the circular monopole antenna has the widest operating frequency range with input return loss < -10 dB. Table 2.1 summarizes the simulation results of directivity, return loss bandwidth ($S_{11} < -10$ dB), and dimension of rectangular patch, dipole, and circular monopole antennas. The directivity of rectangular patch antenna is as high as 6.71 dBi, but the return loss bandwidth is only 10 MHz. In the opposite, the simulated directivity of dipole and circular monopole antennas are below 3 dBi, but the return loss bandwidth is much wider, which is 90 MHz and 3400 MHz, respectively. In order to cover GSM850 band to WiFi band ($824-2480$ MHz), circular monopole antenna is more feasible with 3400-MHz bandwidth.

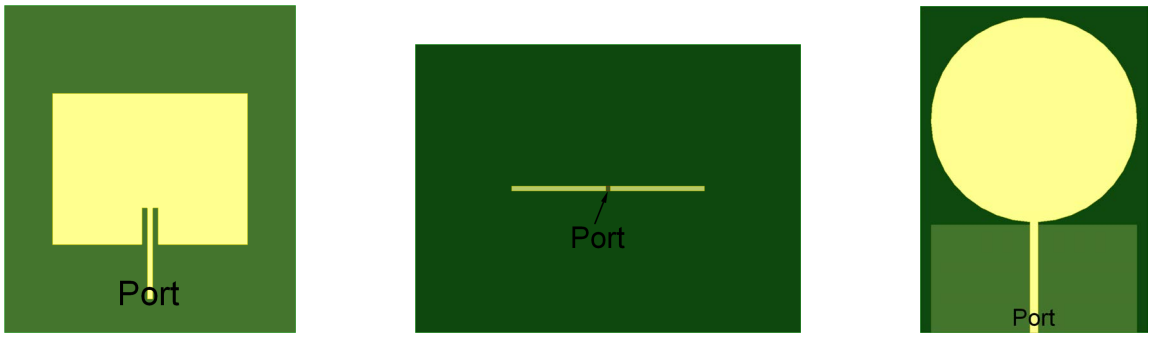

(a) (b) (c)

Figure 2.2: (a) Rectangular patch antenna, (b) dipole antenna, and (c) circular monopole antenna.

The proposed antenna is designed with 50-Ω interface for maximum power transfer to previously designed 800 MHz/1.7 GHz dual-band RF rectifier [16], or 900 MHz receiver assisted by RF blocker energy harvesting [17], or 915 MHz reconfigurable self-startup RF rectifier [18]. Beside the given operating frequency requirements, the proposed antenna is

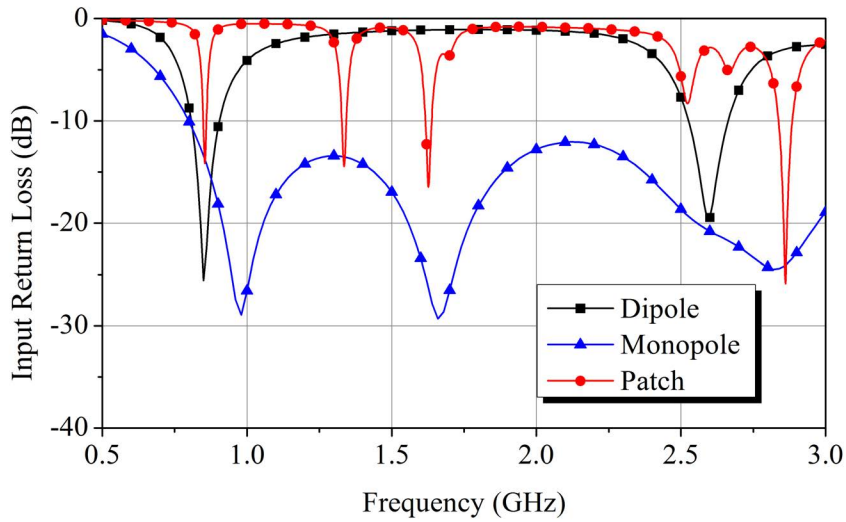

Figure 2.3: Return loss (S_{11}) bandwidth comparison of typical patch, dipole, and monopole antenna.

Table 2.1: Performance comparison of typical antennas.

Topology	Rectangular Patch	Dipole	Circular Monpole
Layout	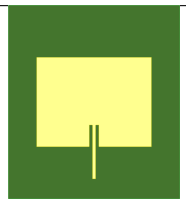		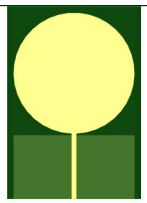
Calculated dimension	10.7×8.4 cm^2	length=9.3 cm	radius=4.0 cm
Simulated dimension	10.7×8.3 cm^2	14.0×0.35 cm^2 cm	radius=4.6 cm
-10 dB S_{11} bandwidth	10 MHz	90 MHz	3400 MHz
Directivity	6.71 dBi	2.28 dBi	2.73 dBi

also designed to operate in GSM850, GSM900, GSM1800, GSM1900, WiFi, Bluetooth, and LTE because the ambient RF signals are ample in these frequency bands.

The design evolution and the corresponding return loss of the proposed antenna is depicted in Fig. 2.4, Fig. 2.5, Fig. 2.6, and Fig. 2.7. The radius a of the circular monopole in Fig. 2.4a can be determined by [19]:

$$a = \frac{3.2}{f_L} - \frac{g}{2.25} \tag{2.2}$$

where f_L is the lower operating frequency with VSWR = 2 (in GHz), g is the gap between the edges of circular monopole and ground plane (in centimeter).

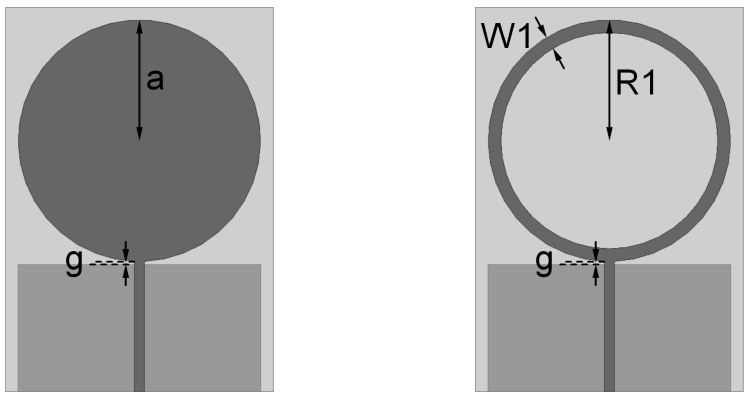

(a) (b)

Figure 2.4: (a) Circular monopole, and (b) annular ring monopole.

The advantage of annular ring monopole in Fig. 2.4b is the lower resonance compared to the circular monopole in Fig. 2.4a with the same dimension. Simulation in Fig. 2.7 shows 17.5% resonance frequency shift between Fig. 2.4a and Fig. 2.4b. Fig. 2.5a and Fig. 2.5b show the design strategy to select the annular ring dimension in Fig. 2.4b at 870-MHz resonance. Parameters $R1$ defines the annular ring radius and $W1$ defines the annular ring strip width in Fig. 2.4b. If the resonance frequency is fixed in Fig. 2.4b, then the larger ring radius with wider strip width ($R1$=48 mm, $W1$=13 mm) achieves wider

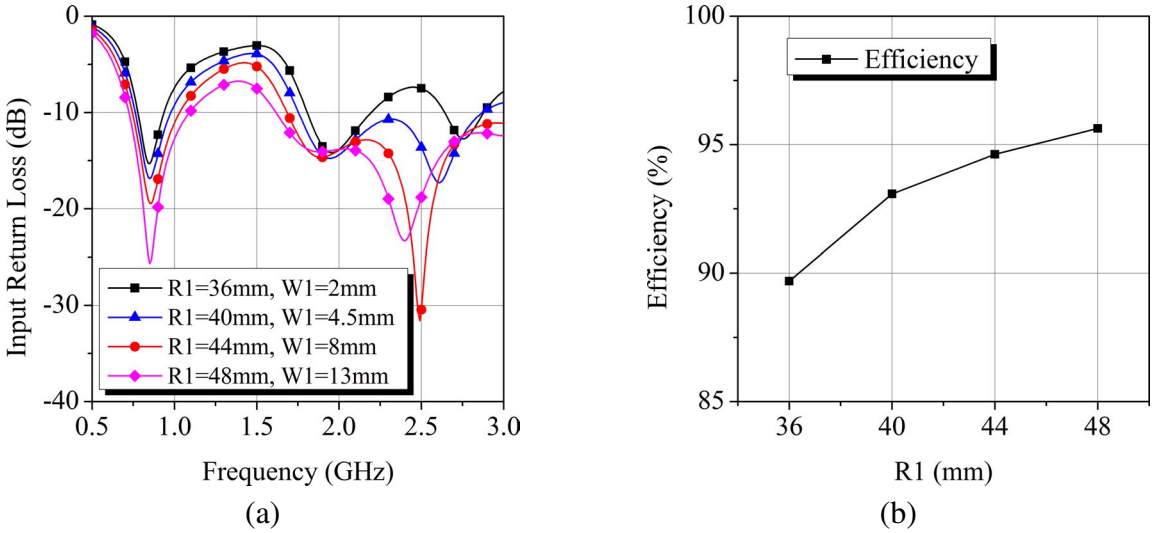

Figure 2.5: (a) return loss bandwidth, and (b) efficiency of the annular ring monopole at 870-MHz resonance.

return loss bandwidth and lower return loss as depicted in Fig. 2.5a, but at the cost of larger antenna dimension. Moreover, larger and wider annular ring has higher efficiency as shown in Fig. 2.5b. The design tradeoff is to reduce ring radius and strip width while maintaining high efficiency and large enough return loss bandwidth with VSWR < 2. The selection here is to achieve return loss < -12 dB in $800-930$ MHz to cover the entire GSM850 and GSM900 bands.

As depicted by Fig. 2.7, the annular ring monopole in Fig. 2.4b is not able to cover GSM1800 and higher frequency bands, thus the double-ring monopole in Fig. 2.6a is developed by adding a second ring inside the first ring. Parameters $R1$ and $R2$ define the annular ring radius, while $W1$ and $W2$ define the annular ring strip width in 2.6a and 2.6b. The second ring creates the resonance at 1.42 GHz and improves the resonance at 1.86 GHz, as shown in Fig. 2.7. Finally, the ground plane of proposed double-ring monopole is notched in Fig. 2.6b to shift the resonance at WiFi band. WGN and LGN specify the size of notched ground in Fig. 2.6b. As shown in Fig. 2.7, The higher order

resonance at 2.68 GHz in Fig. 2.6a is lowered to 2.59 GHz in Fig. 2.6b by notching the ground plane of 5 mm $\times$ 5 mm area.

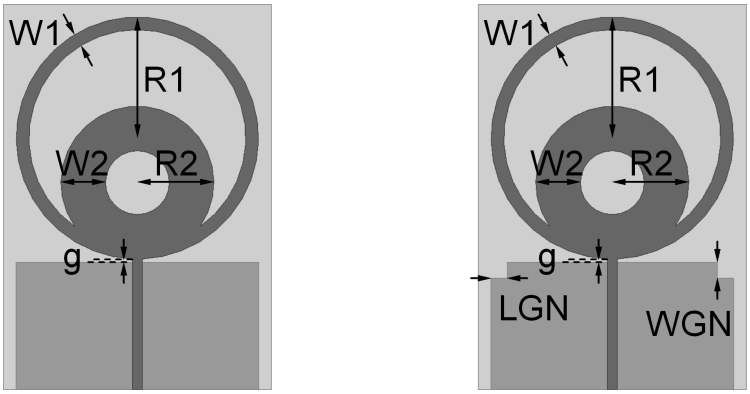

(a) (b)

Figure 2.6: (a) double-ring monopole, (b) proposed double-ring monopole with notched ground.

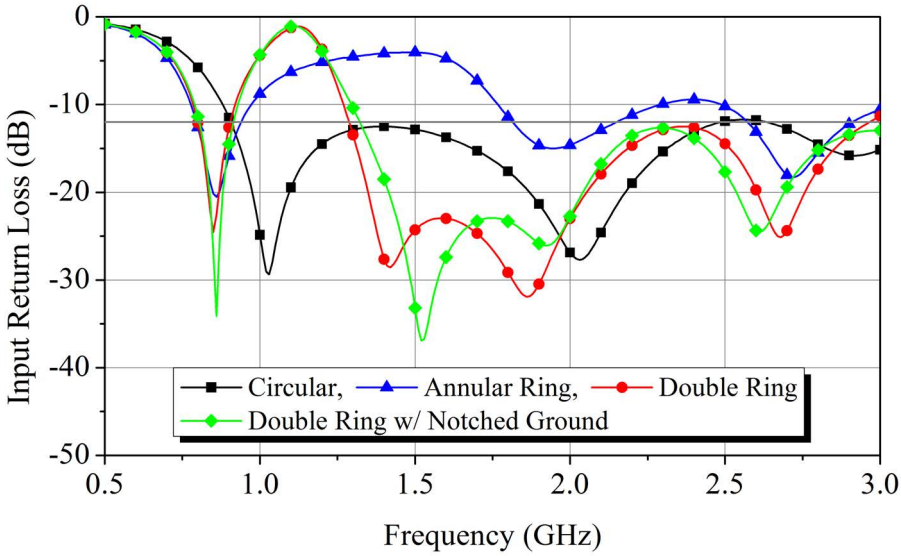

Figure 2.7: Input return loss comparison.

Fig. 2.8a and Fig. 2.8b show the top and $A - A'$ cross section views of the proposed antenna. The photograph of the fabricated antenna is presented in Fig. 2.8c. The antenna is designed on standard FR4 material ($\epsilon_r = 4.4$, $tan\delta = 0.021$), and the substrate thickness h is 1.6 mm. The dimensions of the proposed antenna are listed in Table 2.2. The diameter of main radiator X is 76 mm, the ground length LG is 40 mm, and the gap g between the main radiator and the ground plane is 1 mm. The notched ground area is 5 mm $\times$ 5 mm. Area reduction of 37% is achieved when compared to the circular monopole with the same lower operating frequency.

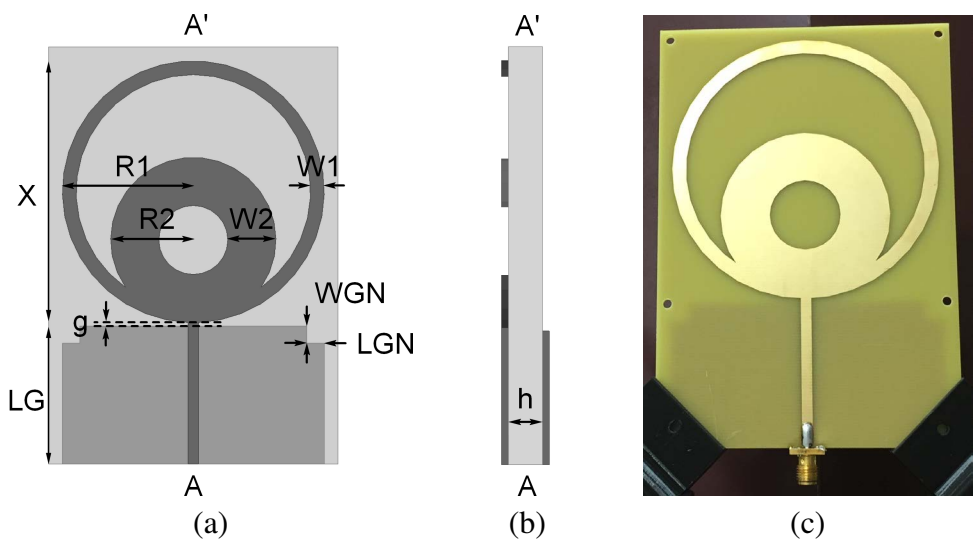

Figure 2.8: (a) Top view and (b) $A - A'$ cross section view of the proposed double-ring monopole antenna, and (c) photograph of the fabricated antenna.

Table 2.2: Geometries of the Proposed Double-Ring Monopole Antenna

R1	W1	R2	W2	g	WGN	LGN
38 mm	4 mm	24 mm	14 mm	1 mm	5 mm	5 mm

The simulated surface current distribution in a wide range of frequencies is presented in Fig. 2.9. For a 870-MHz input, when the current maximum occurs at the end of feeding line as depicted in Fig. 2.9a, the current minimum occurs at the upper edge of outer ring, which confirms that the first resonance is mainly produced by the outer ring. Similarly, the current minimums occur mainly at the outer part of inner ring with a 1.8-GHz input in Fig. 2.9b and at the inner part of inner ring with a 2.44-GHz input in Fig. 2.9c, which produce the second resonance and the third resonance, respectively. The simulated realized gains are 2.60 dBi, 3.03 dBi, and 3.74 dBi at 870-MHz, 1.8-GHz, and 2.44-GHz operating frequencies, respectively. The corresponding simulated total efficiencies are 93.6%, 93.8%, and 89.0%.

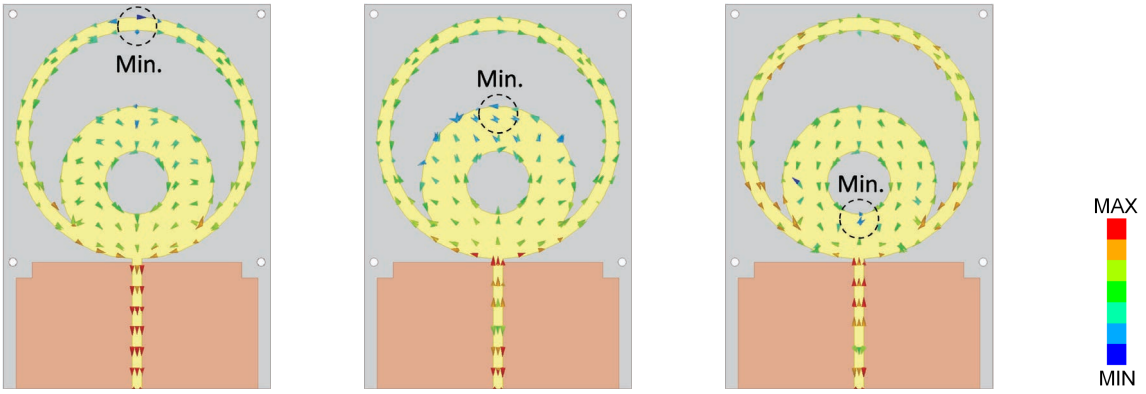

(a) (b) (c)

Figure 2.9: Simulated surface current distribution at (a) 870 MHz, (b) 1.8 GHz, and (c) 2.44 GHz.

2.3 Fabrication and Experimental Results

The return loss of the fabricated antenna is measured via the Agilent N5230A calibrated vector network analyzer (VNA). The realized gain, radiation pattern, and efficiency are measured via the chamber at Texas A&M University. Fig. 2.10 shows the measured

return loss with three resonances. The return loss is lower than -10 dB in 823$-$917 MHz and 1.26$-$3.09 GHz ranges, which depicts wideband/multiband characteristics. The return loss discrepancy in 1.5$-$2.3 GHz range is due to the SMA connector modeling. Modeling the SMA connector directly by measurement results might help to improve the simulation accuracy.

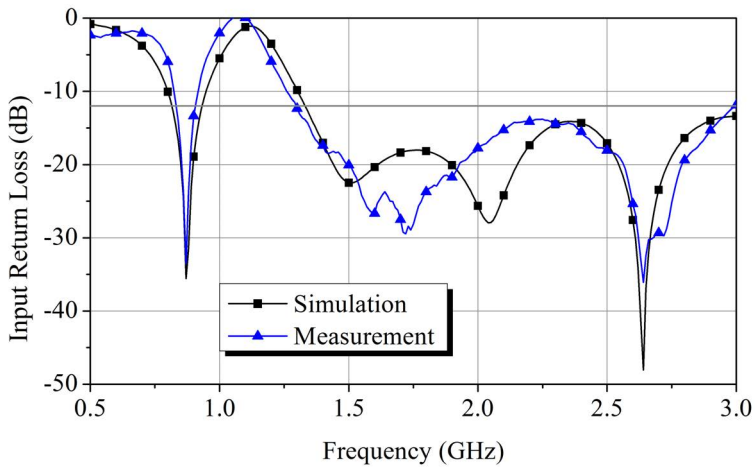

Figure 2.10: Simulated and measured return loss.

The measured normalized H-plane radiation patterns at 880 MHz, 1.7 GHz, and 2.44 GHz are presented in Fig. 2.11a, Fig. 2.11c, and Fig. 2.11e. The simulated normalized E-plane radiation patterns are also plotted in Fig. 2.11b, Fig. 2.11d, and Fig. 2.11f. The antenna is vertically polarized which can capture the ambient RF signals with proper alignment. The measured H-plane co-polarization radiation patterns confirm that the proposed antenna has omnidirectoinal patterns in multiple frequency bands, which is desirable for multiband RF energy harvesting with unspecified sources. The measured realized gains are 1.45 dBi at 860 MHz, 1.73 dBi at 1.8 GHz, and 0.98 dBi at 2.44 GHz, respectively.

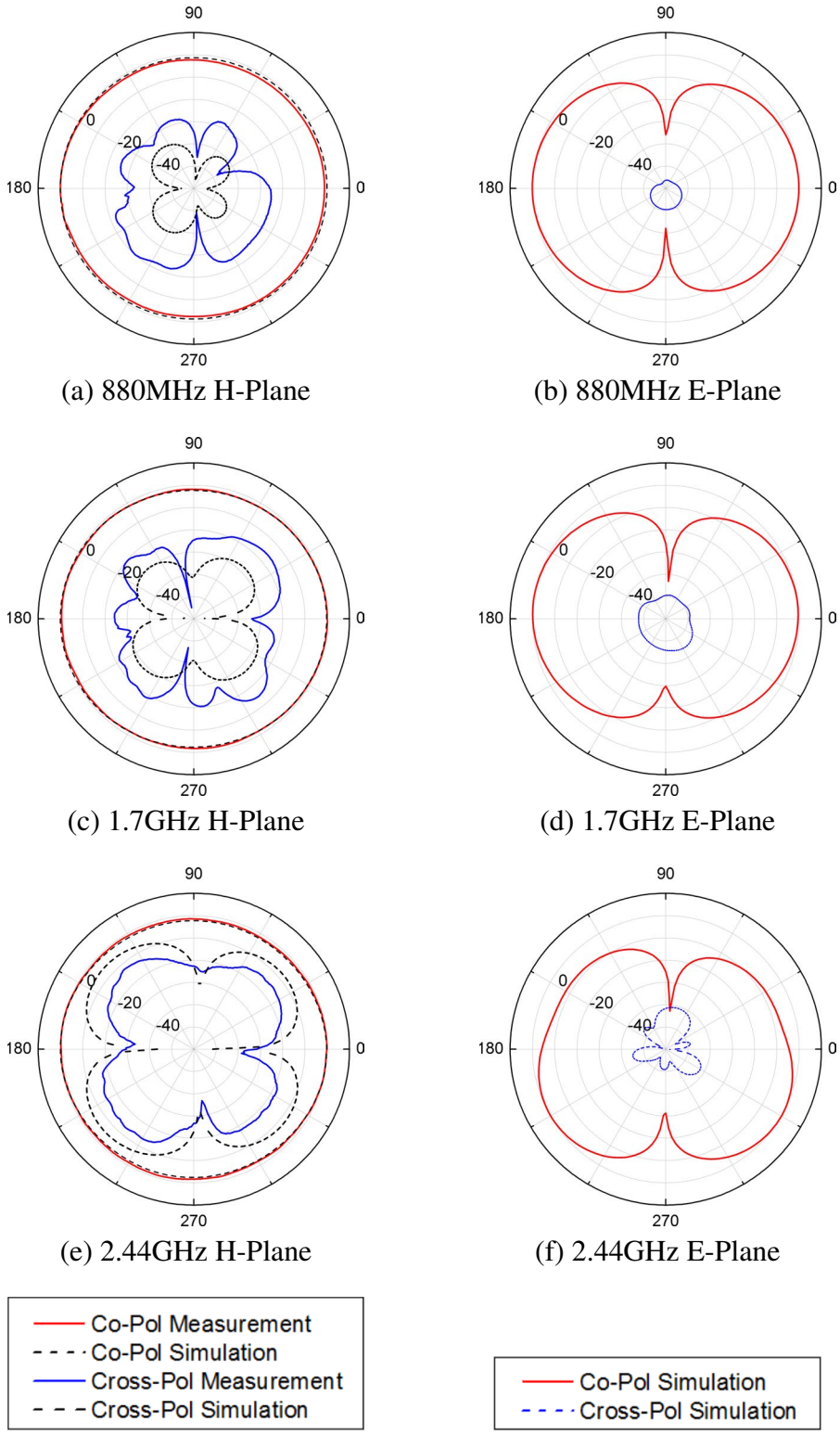

(a) 880MHz H-Plane

(b) 880MHz E-Plane

(c) 1.7GHz H-Plane

(d) 1.7GHz E-Plane

(e) 2.44GHz H-Plane

(f) 2.44GHz E-Plane

Figure 2.11: Normalized measured H-plane and simulated E-plane radiation patterns at 880 MHz, 1.7 GHz, and 2.44 GHz

Table 2.3 lists the measured efficiency in all frequency bands of interest. The measured efficiency varies between 76.7%−93.1% in multiple bands and is 91.8% at 860 MHz, 83.0% at 1.8 GHz, and 78.9% at 2.44 GHz, respectively. The efficiency difference may cause from the PA modules used in the chamber. Table 2.4 summarizes the performance of the proposed double-ring monopole antenna. The lowest operating frequency is defined as the lowest frequency with return loss < -10 dB, and the center operating frequency is defined as the resonance frequency. The impedance bandwidth is calculated for each frequency band with return loss < -10 dB, and the antenna size is reported relative to the effective wavelength at the lowest operating frequency to present a fair comparison. As can be seen, the proposed antenna has the widest impedance bandwidth in triple bands with more isotropic gain, high efficiency, and relatively compact size.

Table 2.3: Measured efficiency of the proposed antenna

Frequency (MHz)	820	860	920
Efficiency (%)	84.7	91.8	84.4
Frequency (MHz)	1700	1800	1900
Efficiency (%)	77.1	83.0	93.1
Frequency (MHz)	2400	2440	2480
Efficiency (%)	87.5	78.9	76.7

Table 2.4: Comparison of Related Works in Literature

	[10]	[11]	[12]	[13]	[14]	**This Work**
Antenna Type	meandered monopole	rectangular monopole	bent triangular monopole	folded dipole	stacked disc	**double-ring monopole**
Substrate Material	ROGER4003 $\epsilon_r = 3.55$ $tan\delta$ =3E-3	cardboard $\epsilon_r = 1.78$ $tan\delta$ =2.5E-2	FR4 $\epsilon_r = 4.4$ $tan\delta$ =2E-2	Arlon 25N $\epsilon_r = 3.38$ $tan\delta$ =2.5E-3	not reported $\epsilon_r = 3.55$ $tan\delta$ =2.7E-3	FR4 $\epsilon_r = 4.4$ $tan\delta$ =2.1E-2
Bands	triple	dual	dual	dual	dual	triple
Lowest Operating Frequency	$\sim$ 920 MHz	600 MHz	850 MHz	$\sim$ 875 MHz	$\sim$ 1.9 GHz	823 MHz
Center Operating Frequency	940 MHz, 1.95 GHz, 2.40 GHz	$\sim$ 670 MHz, $\sim$ 1.30 GHz	$\sim$ 960 MHz, $\sim$ 1.82 GHz	915 MHz, 2.45 GHz	1.95 GHz, 2.45 GHz	870 MHz, 1.72 GHz, 2.64 GHz
Bandwidth (MHz)	$\sim$ 40, $\sim$ 200, $\sim$ 875	$\sim$ 250, $\sim$ 650	$\sim$ 290, $\sim$ 800	$\sim$ 80, $\sim$ 300	97.5, 110.25	94, 990, 1160
Efficiency (%)	not reported	73.0 at 0.8 GHz, 78.6 at 1.0 GHz, 80.5 at 1.2 GHz, 72.6 at 1.5 GHz	$>$ 75 in 0.85$-$1.94 GHz	not reported	90.0 at 1.95 GHz 91.6 at 2.45 GHz	91.8 at 860 MHz, 83.0 at 1.8 GHz, 78.9 at 2.44 GHz
Gain (dBi)	not reported	$>$ 4 at 1.2 GHz	$>$ 2 in 0.85$-$1.94 GHz	1.87 at 915 MHz, 4.18 at 2.45 GHz	8.3 at 1.95 GHz, 7.8 at 2.45 GHz	1.45 at 860 MHz, 1.73 at 1.8 GHz, 0.98 at 2.44 GHz
Size	$\sim 0.50\lambda\times$ 0.22λ	$\sim 0.40\lambda\times$ 0.18λ	$\sim 0.49\lambda\times$ 0.42λ	$\sim 0.60\lambda\times$ 0.60λ	$\sim 0.69\lambda\times$ 0.69λ	$\sim 0.38\lambda\times$ 0.38λ

2.4 Conclusions

A highly efficient double-ring monopole antenna is proposed for multiband RF energy harvesting. In order to increase the harvested RF power in the multitone environment, the proposed antenna has both wideband and multiband features to cover GSM850, GSM900, GSM1800, GSM1900, WiFi, Bluetooth, and LTE communication bands, provided that there are ample RF ambient signals in these frequency bands. Multiband feature is created by two annular rings, and wideband feature is inherent from the monopole topology. The design tradeoff of antenna geometry versus return loss bandwidth is investigated, and

the total efficiency is preserved while achieving a compact size. Area miniaturization of 37% is achieved when compared to the conventional circular monopole with the same lower operating frequency. The antenna measurement confirms wideband and multiband characteristics with return loss < -10 dB in $823-917$ MHz and $1.26-3.09$ GHz ranges. The measured omnidirectional radiation patterns with efficiency range of $76.7\%-93.1\%$ in multiple frequency bands states that the proposed antenna is an attractive candidate for RF energy harvesting.

3. A FOUR-WAY BROADBAND RF ENERGY COMBINER

3.1 Introduction

There are two methods to convert the harvested RF energy from multiple antenna elements to DC energy. The first method as shown in Fig. 3.1a is to convert RF energy to DC energy from each antenna element independently, then the DC energy is combined through the DC energy combiner. The disadvantage of this method is the additional conversion loss in the DC energy combiner. The DC energy combiner needs to convert the DC energy back to RF energy, sum the converted RF energy, then convert the summed RF energy back to DC energy again. The second method as shown in Fig. 3.1b can avoid this additional conversion loss. In Fig. 3.1b, the harvested RF energy from each antenna element is summed through the RF energy combiner then converted to DC energy. Moreover, the most important advantage of using RF energy combiner is the sensitivity relief of RF-DC rectifier. If the harvested ambient RF energy is below the sensitivity of RF-DC rectifier, then no RF energy will be converted to DC energy. As a result, using RF energy combiner can increase the dynamic range of a RF energy harvesting system.

This chapter proposes a highly efficient four-way RF energy combiner for antenna array implementation. The proposed four-way combiner is composed of one Wilkinson combiner, two broadband Wilkinson combiner, and two quarter-wavelength interconnection lines, which can combine four equiphase and equimagnitude inputs below 2.5 GHz due to FR4 substrate loss. The analysis considers the power combining efficiency as the overall effect of return loss, insertion loss, and isolation. The topology selection between Wilkinson combiner or broadband Wilkinson combiner is compared, and the electrical length of interconnection line is analyzed for maximum efficiency.

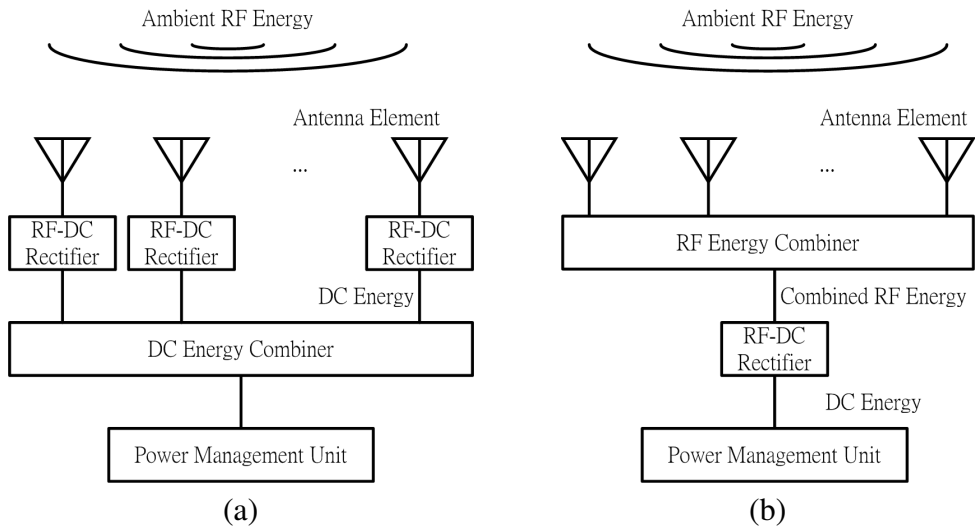

Figure 3.1: Diagram of a RF energy harvesting system with (a) a DC energy combiner, and (b) a RF energy combiner.

3.2 Conventional Power Combiners

3.2.1 Wilkinson Power Combiner

Fig. 3.2 takes a general two-way power combiner as an example to show the design considerations. In Fig. 3.2, two inputs are modeled as sinusoidal sources, and the output port collects the power from both inputs. The desired power flow is directly from the input port to the output port, but part of the input power is reflected as the input matching issue, and part of the input power leaks to another input port as the isolation issue. Therefore, the total combined power at the output port is smaller than the total input power. Normally, the performance of a power combiner is simply determined from the input return loss and the isolation, however, the power combining efficiency should also be taken into account for RF energy harvesting. The power combining efficiency can be defined as:

$$eff = \frac{P_{out}}{P_{input,\,1} + P_{input,\,2}} \tag{3.1}$$

where $P_{input,\ 1}$ is the power at input 1, $P_{input,\ 2}$ is the power at input 2, and P_{out} is the power at output port.

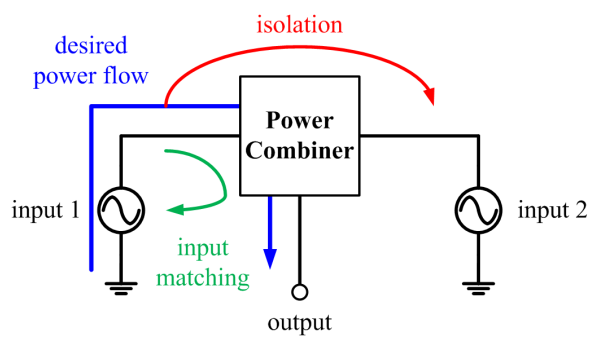

Figure 3.2: Diagram of a two-way power combiner.

Wilkinson power combiner (or divider) is the most widely used interconnection circuit in an antenna array, and the implementation has been thoroughly investigated [20, 4, 3]. The function of a n-way Wilkinson power combiner is to combine n equiphase and equi-magnitude signals into one signal. Fig. 3.3a shows the schematic of a two-way Wilkinson power combiner, which is composed of a pair of quarter-wavelength transmission line and a interconnecting resistor. The characteristic impedance of transmission line is $\sqrt{2Z_0}$, and the impedance of interconnecting resistor is $2Z_0$. The wavelength λ is calculated from the center operating frequency:

$$\lambda = \frac{\frac{c}{f_{center}}}{\sqrt{\epsilon_{eff}}} \tag{3.2}$$

where λ is the wavelength in meter, c is the light speed in meter, f_{center} is the center operating frequency in Hz, and ϵ_{eff} is the effective dielectric constant.

Later, the broadband two-way Wilkinson power combiner is proposed in [4] to increase the bandwidth. Fig. 3.3b shows the schematic of a two-way broadband Wilkinson power

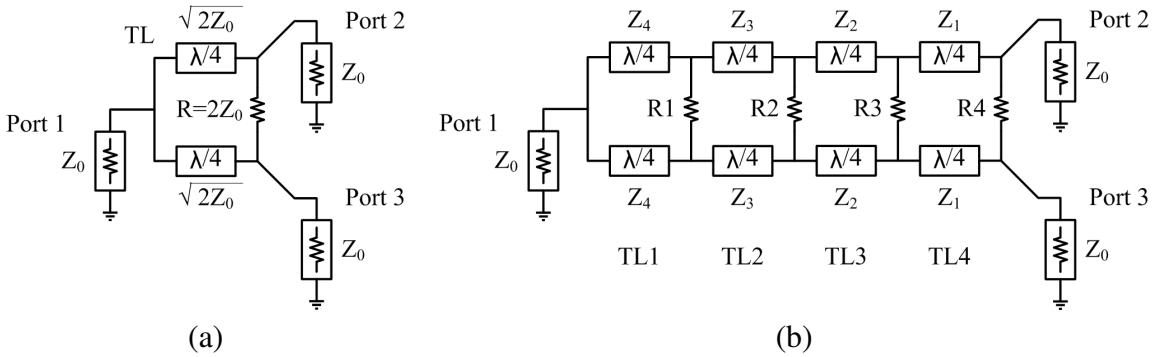

Figure 3.3: Schematic of (a) a two-way Wilkinson power combiner, and (b) a two-way broadband Wilkinson power combiner.

Table 3.1: Adapted from [4] normalized design parameters of the two-way broadband Wilkinson power combiner .

N	3	4	7
f_2/f_1	3.0	4.0	10.0
VSWR$_{Port\ 1}$ (max)	1.105	1.100	1.206
VSWR$_{Port\ 2,\ 3}$ (max)	1.038	1.039	1.098
Isolation$_{min}$, (dB)	27.9	26.8	19.4
Z_1	1.1497	1.1157	1.1274
Z_2	1.4142	1.2957	1.2051
Z_3	1.7396	1.5435	1.3017
Z_4		1.7926	1.4142
Z_5			1.5364
Z_6			1.6597
Z_7			1.7740
R_1	8.0000	9.6432	8.8496
R_2	4.2292	5.8326	12.3229
R_3	2.1436	3.4524	8.9246
R_4		2.0633	6.3980
R_5			4.3516
R_6			2.5924
R_7			4.9652

combiner, which is composed of multiple pairs of quarter-wavelength transmission lines and multiple interconnecting resistors. The characteristic impedance of i-th transmission line is labeled as Z_i, and the impedance of i-th interconnecting resistor is labeled as Z_i. The main advantages of broadband Wilkinson power combiner include lower input return loss, wider impedance bandwidth, and higher isolation than the Wilkinson power combiner. Table 3.1 lists the normalized design parameters of the broadband Wilkinson power combiner. In order to use Table 3.1, the definition of fractional bandwidth is introduced:

$$fractional\ BW = \frac{BW}{f_{center}} = 2\frac{f_2/f_1 - 1}{f_2/f_1 + 1} \tag{3.3}$$

where $fractional\ BW$ is the fractional bandwidth, BW is the bandwidth in Hz, f_{center} is the center operating frequency in Hz, and f_2/f_1 is the look-up parameter in Table 3.1.

The bandwidth requirement of a broadband Wilkinson power combiner is based on the antenna specification. For example, the proposed double-ring monopole antenna operates in 800 MHz $-$2.5 GHz frequency range, thus the center operating frequency is 1.65 GHz and the bandwidth is 1.7 GHz. Choosing N=4 and f_2/f_1=4 from Table 3.1, then the calculated bandwidth is 1.98 GHz, which leaves some margins to cover the entire operating frequency range of the proposed antenna:

$$BW = (1.65 \times 10^9) \times 2(4-1)/(4+1) = 1.98 \times 10^9 \tag{3.4}$$

Table 3.2 shows the characteristic impedance of transmission lines and the interconnecting resistor values of both Wilkinson and four-section broadband Wilkinson power combiners based on standard 50Ω interface. The physical parameters such as microstrip line width (W) and line length (L) can be determined from Table 3.2, and the results are presented in Table 3.3. The corresponding layouts are shown in Fig. 3.4a and Fig. 3.4b.

Table 3.2: Characteristic impedance and interconnecting resistor values of the Wilkinson and broadband Wilkinson power combiners.

Z (Ω)	Wilkinson (N=1)	Broadband Wilkinson (N=4)
TL_1	70.71	86.63
TL_2		77.18
TL_3		64.79
TL_4		55.79
R_1	100	100
R_2		330
R_3		590
R_4		1000

Table 3.3: Microstrip line width and length values of the Wilkinson and broadband Wilkinson power combiners.

	Wilkinson (N=1)	Broadband Wilkinson (N=4)
W_1 (mm)	1.6	1
W_2 (mm)		1.5
W_3 (mm)		2
W_4 (mm)		2.5
$L_{1,2,3,4}$ (mm)	24	24

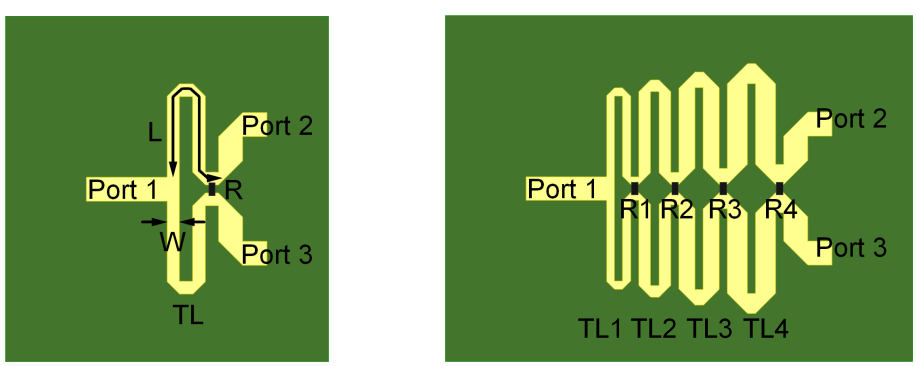

(a) (b)

Figure 3.4: Layout of (a) a two-way Wilkinson power combiner, and (b) a two-way broadband Wilkinson power combiner.

3.2.2 Rat-Race Coupler

Rat-race coupler is also capable of combining RF energy, and the schematic is presented in Fig. 3.5a. The rat-race coupler is a four-port device with two input ports and two output ports, and it can combine either in-phase or out-of-phase inputs. The combined RF energy will go through only one of the two output ports depending on the phase property of two input signals. If the two input signals are in-phase, then the RF energy flows through the Σ port. In the opposite, if the two input signals are out-of-phase, then the RF energy flows through the Δ port. The rat-race coupler is composed of three 1/4 wavelength transmission lines and one 3/4 wavelength transmission line. The characteristic impedance is $\sqrt{2Z_0}$ for all transmission lines. The physical microstrip line width and length parameters can directly refer from Table 3.3. For 1.65-GHz center operating frequency, the quarter-wavelength equals 24 mm, and the 70.71-Ω characteristic impedance requires 1.6-mm thick microstrip line width. The microstrip line layout in Fig. 3.5b adopts circular shape, and the radius is 22 mm.

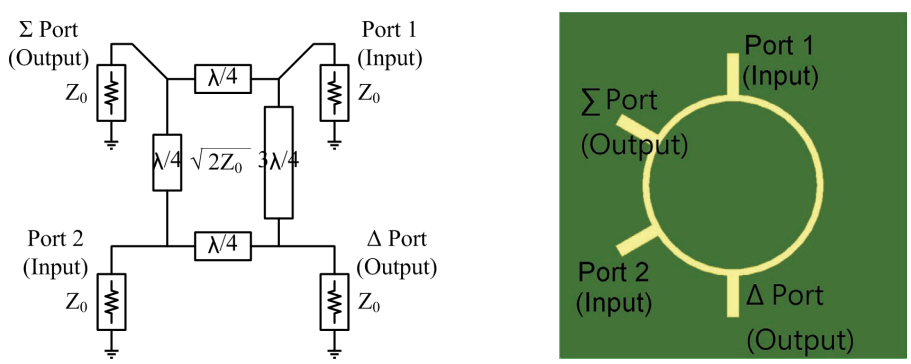

(a) (b)

Figure 3.5: (a) schematic and (b) layout of a rat-race coupler.

The advantage of using the rat-race coupler is the alignment flexibility in an antenna array. The Wilkinson type power combiner can only combine in-phase inputs as shown in Fig. 3.6, but the rat-race type power combiner can combine in-phase or out-of-phase inputs as shown in Fig. 3.7. For large antenna array systems, combining out-of-phase inputs can reduce the interconnection length and therefore reduce the conductor loss in the transmission path. The disadvantage of the rat-race coupler is the additional unused output port, which must be properly terminated to a high quality and broadband 50Ω resistor.

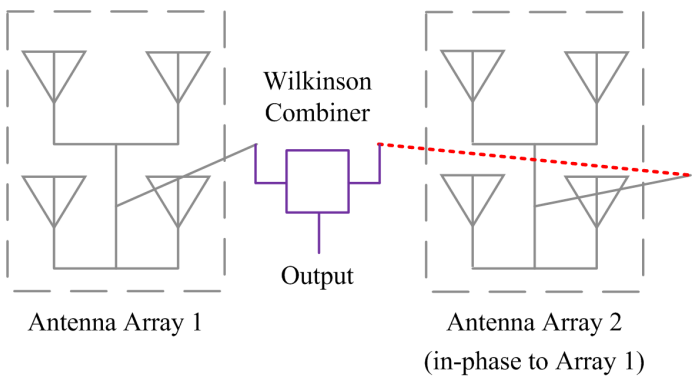

Figure 3.6: Antenna array with a Wilkinson type power combiner.

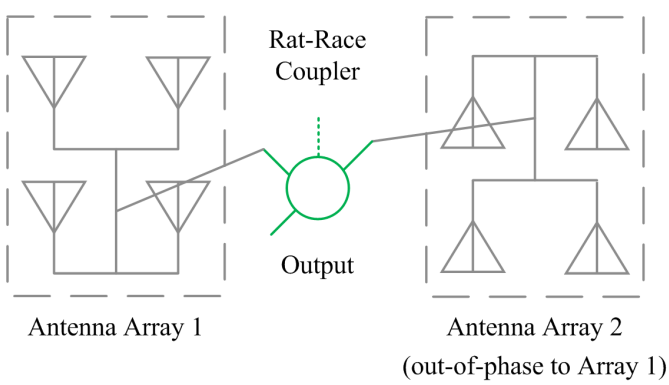

Figure 3.7: Antenna array with a rat-race type power combiner.

3.2.3 Performance Comparison

This section compares the performance of the Wilkinson power combiner, the broadband Wilkinson power combiner, and the rat-race coupler. The return loss simulation results in Fig. 3.8a and Fig. 3.8b together with the isolation simulation result in Fig. 3.9a confirm that the broadband Wilkinson power combiner has lower return loss, wider bandwidth, and higher isolation than the Wilkinson power combiner. The disadvantage of the broadband Wilkinson power combiner is the higher phase imbalance introduced at the output port, as shown in Fig. 3.9b. The phase imbalance is the phase difference between two signals at the output port. The rat-race coupler is inferior to Wilkinson and broadband Wilkinson power combiners in turns of bandwidth as shown in Fig. 3.8a. The design of broadband rat-race coupler can resolve the bandwidth issue, but the fabrication requires either advanced technique or multi-layer dielectrics, and either method is costly. As a result, Wilkinson and broadband Wilkinson power combiners are more attractive candidates to combine RF energy in wider frequency range.

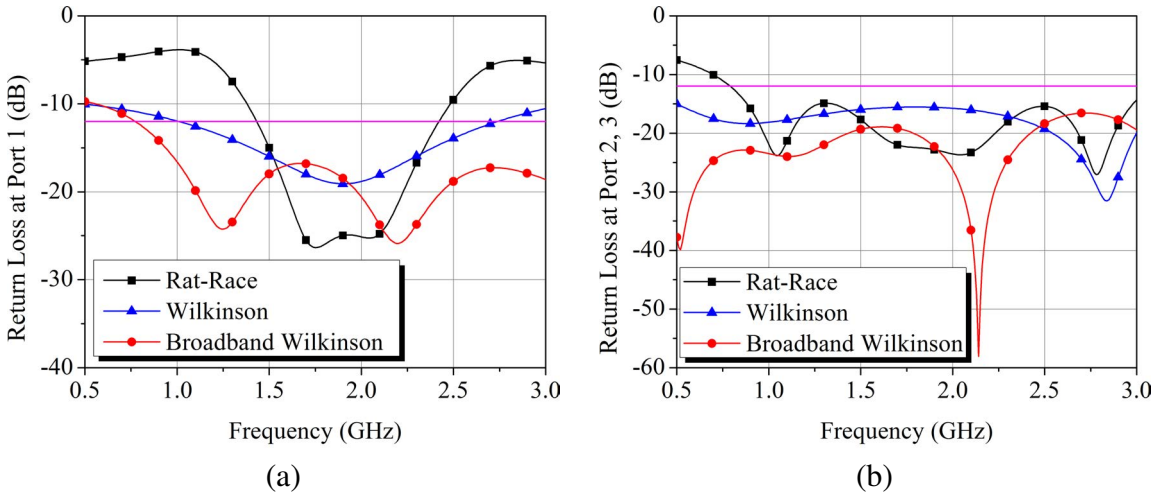

Figure 3.8: Comparison of (a) return loss at output port and (b) return loss at input port in different power combiners.

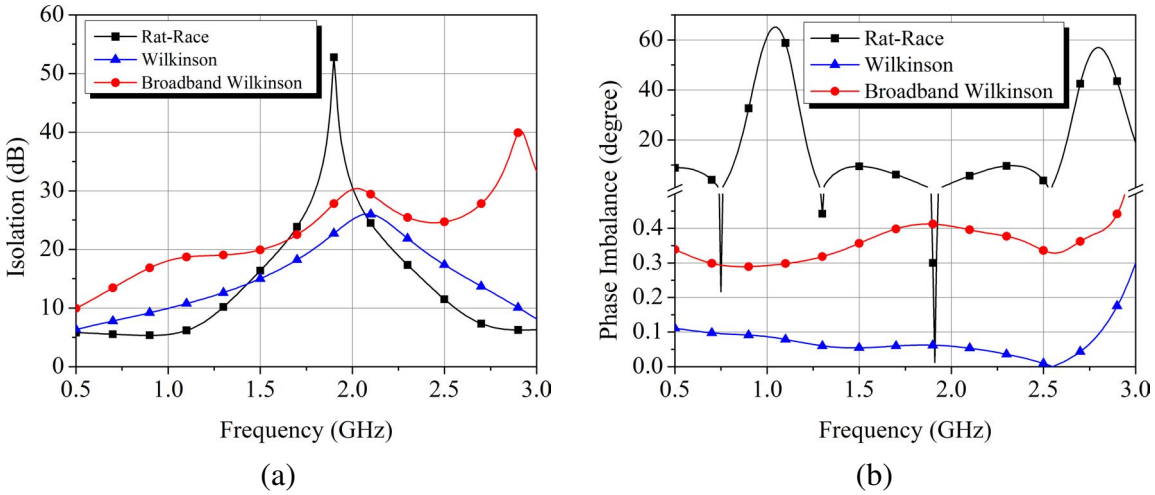

Figure 3.9: Comparison of (a) isolation between input ports, and (b) phase imbalance at output port in different power combiners.

Besides the conventional figure of merits, the power combining efficiency should also be taken into accounts. The simulated efficiency of the Wilkinson power combiner is the highest in 1.25−3.0 GHz frequency range, as shown in Fig. 3.10. The reason behinds it is the path loss. Because the total transmission line length of the four-section broadband Wilkinson power combiner is four times of the Wilkinson power combiner, the RF power flow experiences four times path loss. The path loss is also proportional to the RF signal frequency, thus the efficiency drops when the input frequency increases. In 0.77−1.25 GHz range, the broadband Wilkinson power combiner has the highest simulated efficiency as 91.85%, but the simulated efficiency difference between Wilkinson and broadband Wilkinson power combiners is only 1% in this frequency range. While in 1.25−3.0 GHz range, the Wilkinson power combiner has the highest simulated efficiency as 93.11%. Therefore, the Wilkinson power combiner is more suitable for RF energy harvesting purpose.

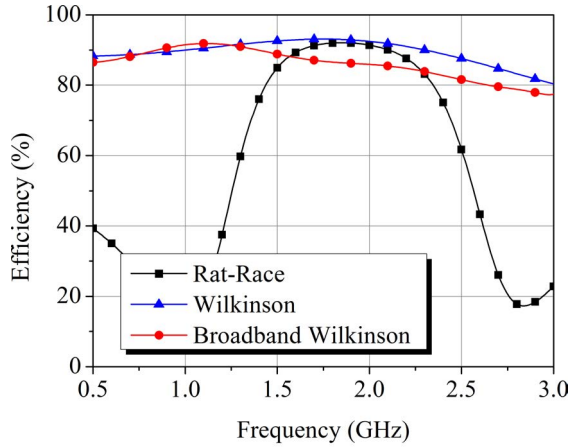

Figure 3.10: Comparison of power combining efficiency in different power combiners.

3.3 Proposed Four-Way Broadband RF Energy Combiner

In [3], the author demonstrates how to design a multiway power divider by the broadband two-way Wilkinson power dividers. As shown in Fig. 3.11, a four-way power divider is implemented by interconnecting three two-way Wilkinson power dividers, and the effect of interconnecting transmission lines is investigated. The S_{11} simulation in [3] ststes that using the quarter-wavelength ($\theta = \pi/2$) 50-Ω interconnecting transmission line achieves the widest return loss bandwidth. The S_{22} and the S_{23} simulations in [3] show that the interconnection has little effect on them. This section extends the concept in [3] to further investigate the efficiency of the four-way RF energy combiner based on Wilkinson type power combiners.

The diagram of the proposed four-Way broadband RF energy combiner is presented in Fig. 3.12. Three building blocks and two interconnecting transmission lines form the four-way Wilkinson power combiner. N_1 represents the sections of the two-way power combiner which connects to the output port (port 1), and N_2 represents the sections of the two-way power combiner which connects to two input ports (Port 2 and Port 3 or Port 4

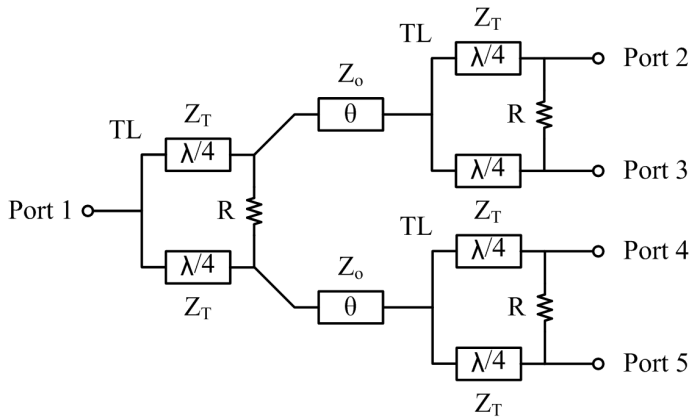

Figure 3.11: Adapted from [3] schematic of the four-way Wilkinson power divider by interconnecting three two-way Wilkinson power dividers .

and Port 5). Each building block can be either the Wilkinson power combiner (N=1) or the four-section broadband Wilkinson power combiner (N=4). Choosing four-section design is the trade-off between return loss bandwidth and power combining efficiency. As can be inferred from Table 3.1 and Fig. 3.10, more sections has wider return loss bandwidth but lower power combining efficiency. In order to cover the operating frequency range (0.8−2.5 GHz) of the proposed antenna, at least four sections are required.

The implementation of the proposed four-Way Wilkinson power combiner with different N_1 and N_2 values are displayed in Fig. 3.13. The layout considers four possible combinations: $(N_1,\ N_2) = (1,\ 1),\ (1,\ 4),\ (4,\ 1),\ (4,\ 4)$. Because the four-way power combiner is used in an antenna array, the distance between four inputs is kept constant for fair comparison, and the design here sets the horizontal distance to 275 mm. Fig. 3.14 and Fig. 3.15a to Fig. 3.15d show the simulation results of the proposed four-way power combiner with different N_1 and N_2 combinations. Consider the findings in [3], the electrical length of the interconnecting transmission line is set to quarter wavelength ($\theta = \pi/2$) for wider return loss bandwidth. The optimum power combining efficiency is achieved when choosing $N_1 = 1$ and $N_2 = 4$, as shown in Fig. 3.14. Select $N_1 = 1$ and $N_2 = 1$

only has competitive efficiency at frequency below 1.8 GHz. It is also found that smaller N_1 value is desirable in turns of power combining efficiency. The return loss simulation in Fig. 3.15a and Fig. 3.15b, and the isolation simulation in Fig. 3.15c and Fig. 3.15d follow the conclusion in [4] that the power combiner with more sections has wider return loss bandwidth and higher isolation. As a result, the combination of $N_1 = 4$ and $N_2 = 4$ is the best choice to divide signals in consideration of return loss and isolation, but the combination of $N_1 = 1$ and $N_2 = 4$ is the optimum choice for RF energy harvesting in consideration of power combining efficiency.

The main reason behinds the efficiency drops versus increasing frequency in Fig. 3.14 is the transmission line loss. Table 3.4 summarizes the transmission line loss on FR4 PCB versus frequency. For every 10-mm long 50Ω line, the loss at 0.86 GHz, 1.8 GHz, and 2.44 GHz is 0.023dB, 0.058dB, and 0.081dB, respectively. The higher loss at high frequency degrades the efficiency of the four-way power combiner, however, as long as the efficiency is higher than 25%, the total output power is still higher than single input power.

The effect of interconnecting transmission lines on the power combining efficiency is also investigated for $(N_1,\ N_2) = (1,\ 4)$ combination. Three electrical length, $\theta = \pi/6$, $\pi/2$, and π, are selected for demonstration. The corresponding layouts are shown in Fig. 3.16a, Fig. 3.16b, and Fig. 3.16c, respectively. The simulated efficiency in Fig. 3.17 states that $\theta = \pi/2$ is the optimum electrical length for interconnecting transmission line.

Table 3.4: Simulated 50Ω line loss on FR4 substrate.

Frequency (GHz)	0.86	1.80	2.44
Loss (dB/10 mm)	0.023	0.058	0.081

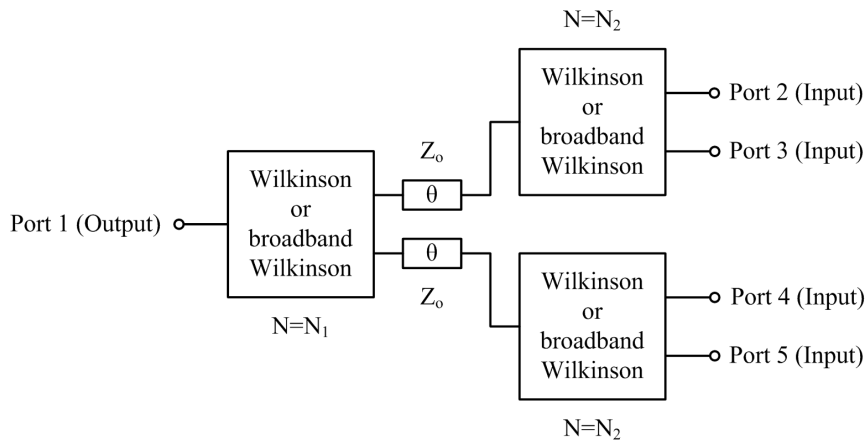

Figure 3.12: Structure of the proposed four-way broadband RF energy combiner.

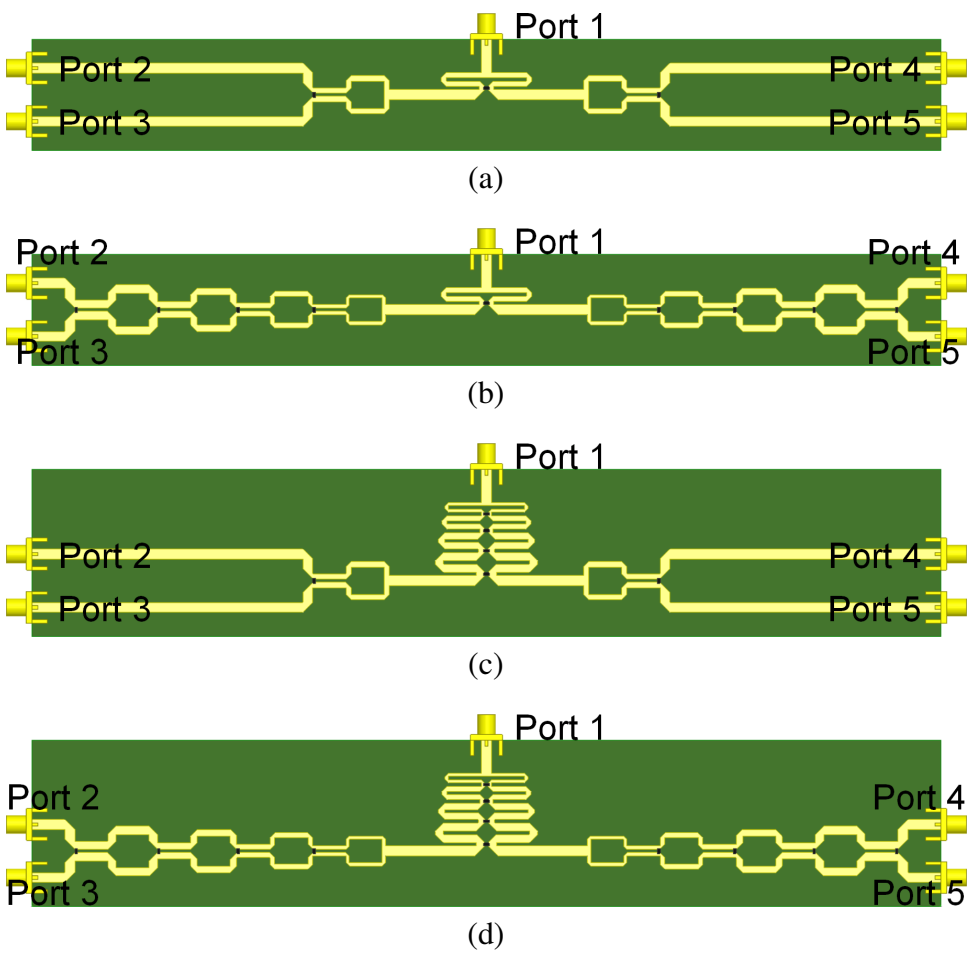

Figure 3.13: Layout with $\theta = \pi/2$ and (a) $(N_1,\ N_2) = (1,\ 1)$, (b) $(N_1,\ N_2) = (1,\ 4)$, (c) $(N_1,\ N_2) = (4,\ 1)$, and (d) $(N_1,\ N_2) = (4,\ 4)$.

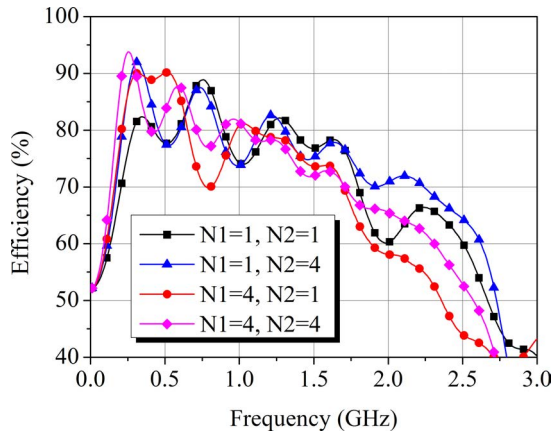

Figure 3.14: Efficiency simulation results with $\theta = \pi/2$.

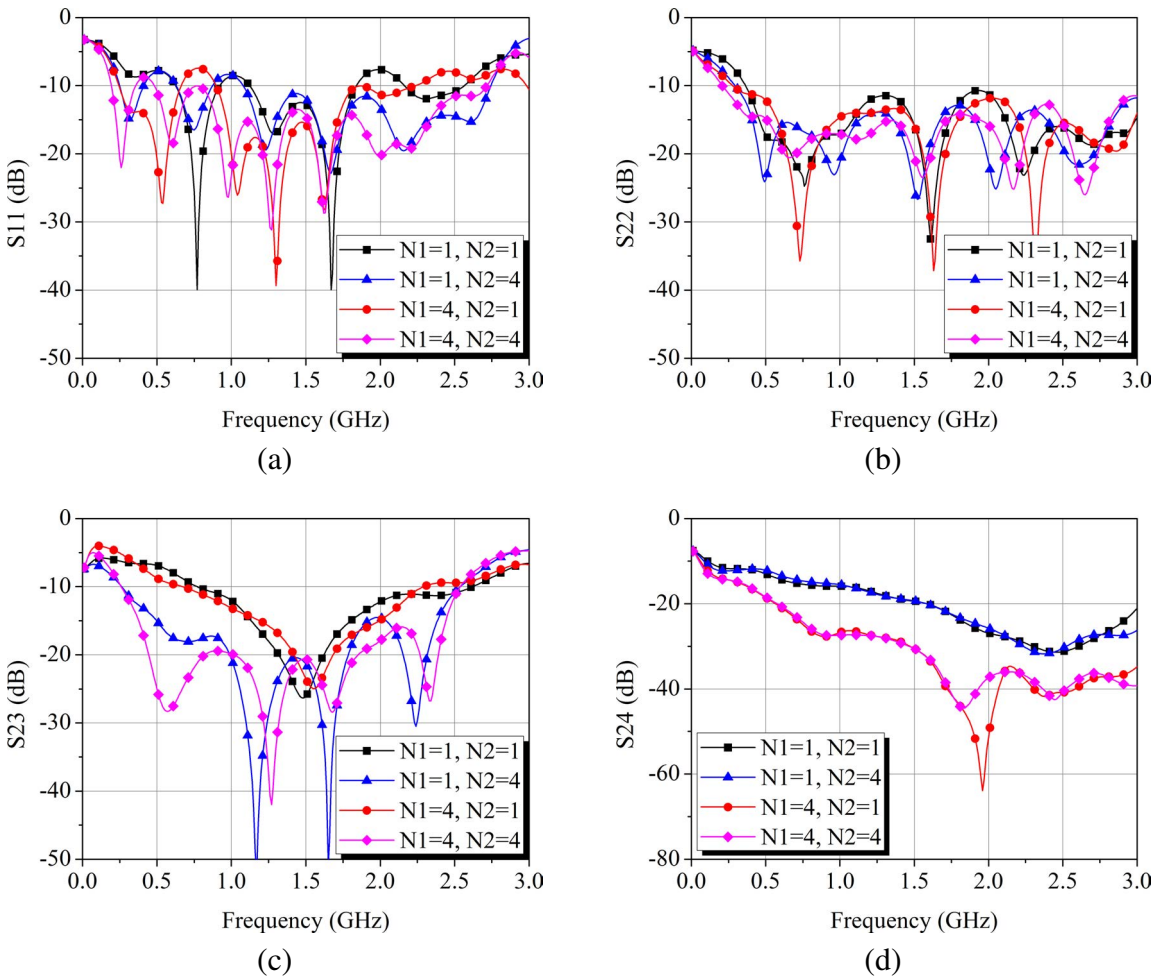

Figure 3.15: (a) S_{11}, (b) S_{22}, (c) S_{23}, and (d) S_{24} simulation results with $\theta = \pi/2$.

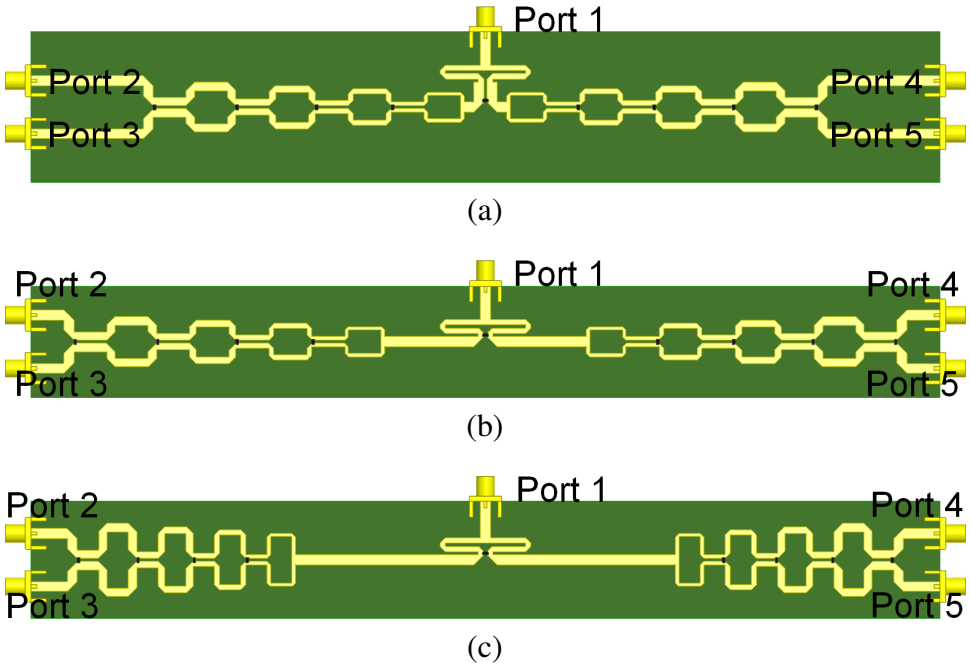

Figure 3.16: Layout with $(N_1,\ N_2) = (1,\ 4)$ and (a) $\theta = \pi/6$, (b) $\theta = \pi/2$, and (c) $\theta = \pi$.

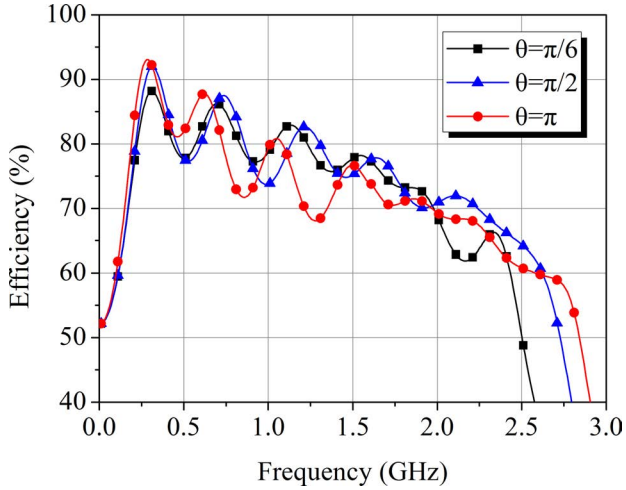

Figure 3.17: Efficiency simulation results with $(N_1,\ N_2) = (1,\ 4)$.

3.4 Fabrication and Experimental Results

The schematic and photograph of the proposed four-way broadband RF energy combiner are shown in Fig. 3.18a and Fig. 3.18b, respectively. The four-way combiner is designed on standard FR4 material ($\epsilon_r = 4.4$, $tan\delta = 0.021$), and the substrate thickness h is 1.6 mm. The transmission line widths, line lengths, and the isolation resistors of the proposed four-way combiner are listed in Table 3.5. The measured scattering parameters are shown in Fig. 3.19. The output and input ports achieve VSWR < 2 in 0.5−2.67 GHz range as depicted in Fig. 3.19a and Fig. 3.19b, respectively. Fig. 3.19c demonstrates the measured insertion loss between output port and input port at port 2, and the insertion loss varies between 6.68−8.35 dB in 0.5−2.5 GHz range. Because the circuit is symmetric, the insertion loss between any input port and the output port is identical. The measured isolation between any two input ports is greater than 10 dB in 0.5−2.5 GHz range, as shown in Fig. 3.19d and Fig. 3.19e. The measured efficiency varies between 53.5%−90.9% in 0.5−2.5 GHz, and the measurement follows the simulation results with variation < 10%, as shown in Fig. 3.19f.

Table 3.5: Parameters of the proposed four-way RF energy combiner.

W_1	1.6 mm	L_1	24 mm	R_1	100Ω
W_2	1 mm	L_2	24 mm	R_2	100Ω
W_3	1.5 mm	L_3	24 mm	R_3	330Ω
W_4	2 mm	L_4	24 mm	R_4	590Ω
W_5	2.5 mm	L_5	24 mm	R_5	1000Ω
W_6	3 mm	L_6	27 mm		

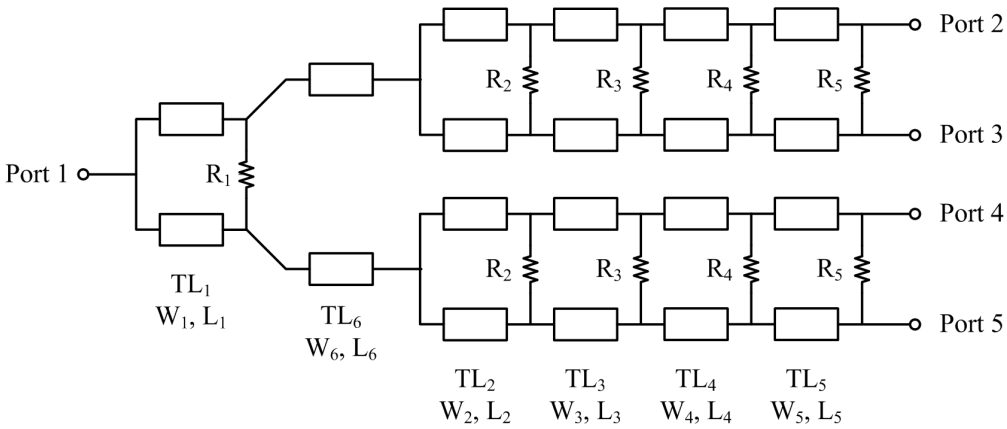

(a)

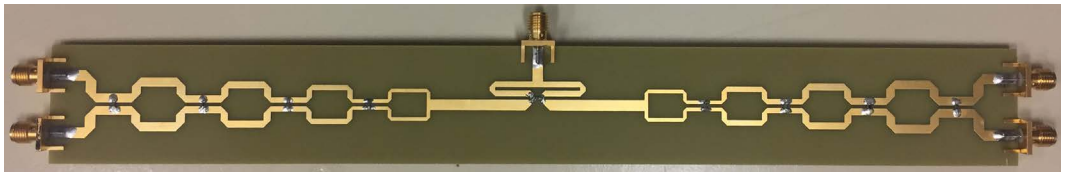

(b)

Figure 3.18: (a) Schematic, and (b) photograph of the fabricated four-way broadband RF energy combiner.

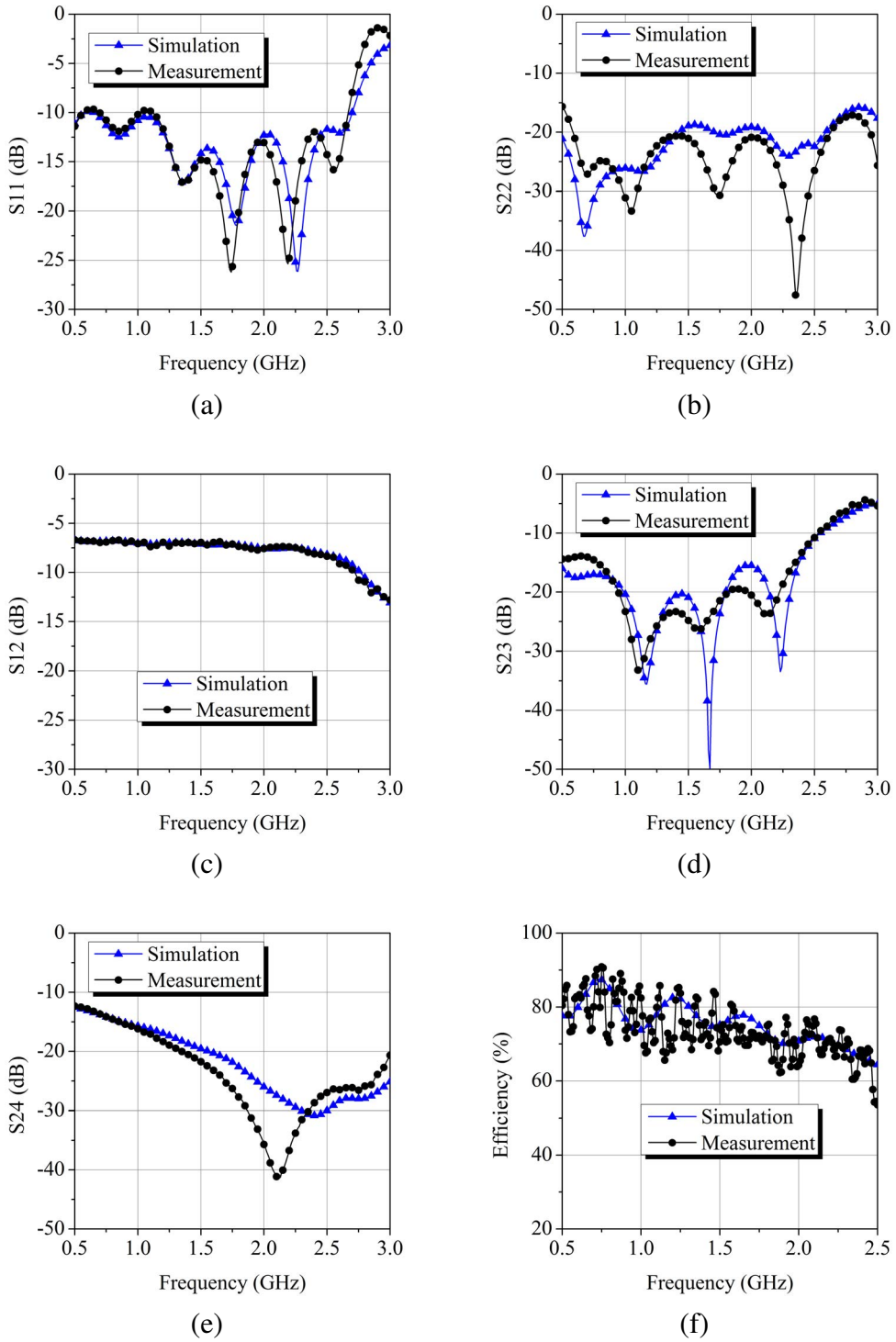

Figure 3.19: (a) Output return loss, (b) input return loss, (c) insertion loss between input and output ports, (d) isolation between adjacent input ports, (e) isolation between non-adjacent input ports, and (f) efficiency of the proposed four-way RF energy combiner.

3.5 Conclusions

A four-way RF energy combiner is proposed to connect four antenna elements with equiphase and equimagnitude inputs. The target operating frequency is below 2.5 GHz due to the FR4 substrate loss. The proposed four-way combiner is composed of one Wilkinson combiner, two broadband Wilkinson combiners, and two quarter-wavelength interconnection lines. The power combining efficiency is considered as the whole effect of input return loss, insertion loss, and isolation. The topology selection between Wilkinson combiner or broadband Wilkinson combiner is compared, and the electrical length of interconnection line is analyzed for maximum efficiency. The measured power combining efficiency varies between $53.5\% - 90.9\%$ in $0.5 - 2.5$ GHz, and the measurement follows the simulation results with variation $< 10\%$.

4. MUTUAL COUPLING COMPENSATED MULTIBAND LINEAR ANTENNA ARRAYS OF DOUBLE-RING MONOPOLES

4.1 Introduction

Friis transmission equation states that the captured/radiated RF power is proportional to the antenna gain, thus high gain antenna is more attractive for RF energy harvesting/transfer. Antenna array is the most commonly used technique to increase antenna gain, but high gain means more directive so that the antenna array can only harvest/transfer RF energy from/to limited directions. In contrast, low gain antenna has more isotropic gain and can operate in wider range of directions. However, the lower harvested/transfered RF power from low gain antenna degrades the efficiency of RF-DC rectifier. Beam-steering technique increases the operating ranges of antenna array by sweeping the antenna beam toward the desired directions. This technique makes antenna array more practical in RF energy harvesting/transfer applications.

Mutual coupling is the electromagnetic interaction between antenna elements in an antenna array, which is an undesirable effect. The phenomenon of mutual coupling has been throughly investigated in [21, 22, 23] and key conclusions have been summarized: Mutual coupling changes the radiation patterns, the received voltages on antenna elements, and the input impedances of antenna elements in an antenna array. Moreover, mutual coupling effect is different in transmitting and receiving antenna arrays. Researchers have put a lot of efforts to compensate mutual coupling effect either by mathematical computation [21, 22, 23, 24, 25] or by physical compensation structure [26, 27, 28, 29].

The conventional mutual-impedance model is proposed for transmitting-mode antenna array in [24], while the receiving mutual-impedance model is derived for receiving-mode antenna array in [21]. HFSS simulation is based on transmitting mode, however, the pro-

posed antenna arrays are operated in receiving mode, thus the simulation discrepancy between transmitting mode and receiving mode should be investigated. In [25], the conventional mutual-impedance model and the calibration model are compared, and the findings show that the conventional mutual-impedance model is accurate in consideration of antenna main beam. Because the design of RF energy harvesting/transfer antenna array focuses mostly on the antenna main beam, the transmitting mode simulation by HFSS is accurate enough to emulate the receiving mode operation.

Several physical structures have been investigated to compensate mutual coupling effects. In [26], using ground baffle as compensation for dipole array is proposed, but the 3D structure is bulky. In [27], slotted-complementary split-ring resonators on ground plane is proposed to reduce mutual coupling, but the return loss is worsen and the radiation patterns show no improvement after compensation. In [28], double-layer electromagnetic band gap (EBG) structure for broadband mutual coupling reduction is presented, but the fabrication requires 55-μm thick dilectric layer, which is costly compared to standard FR4 PCB fabrication. In [29], spatial multiplexing is applied to reduce mutual coupling between patch antennas, but multiplexing antennas reduces the harvested RF energy since only one antenna is connected at any instant of time.

Many works in rectenna/antenna arrays have been designed for RF energy harvesting/transfer [30, 31, 32, 33, 34, 35, 2], but none of them applies mutual coupling compensation, and none of them achieves triple-band operation. Besides, only the designs in [35, 2] are antenna array plus RF-DC rectifier, while other designs are rectenna arrays (rectenna is antenna plus RF-DC rectifier). Rectenna arrays in [32, 30, 33, 34, 31] harvests RF energy from individual antennas, rectifies RF energy with individual RF-DC rectifiers, and then sums the DC energy either by directly DC series connection without consideration of different DC levels at rectenna elements [30, 31] or by continuous power-consuming power management unit [32, 33, 34]. In spite of the DC power combining

issue, more severe problems are the strict sensitivity and efficiency curve of the RF-DC rectifier. In most cases none of the harvested ambient RF energy will be rectified because the ambient RF signal is too small to pass the rectifier threshold, or the system will suffer from extremely low efficiency. On the other hand, antenna array with RF-DC rectifier harvests RF energy from individual antennas, sums the RF energy first and then rectifies RF energy. The continuous power consumption from power management unit can be waived, and the efficiency of RF-DC rectifier can be maintained with higher RF input power. As a result, combining RF energy from antenna array is more practical in real applications.

In this chapter, mutual coupling compensated linear antenna arrays of two and of four double-ring monopoles are proposed for multiband RF energy harvesting/transfer applications. Ground baffles are inserted between antenna elements to compensate mutual coupling, while the effective gain is defined to determine the optimum antenna spacing. Radiation patterns are synthesized at both multiband and wideband frequencies at the cost of return loss matching at each antenna feeding port. The base double-ring monopoles are rematched to 50Ω with the aid of broadband matching networks. The proposed two-element array shows return loss < -10 dB in $726-924$ MHz, $1.24-1.87$ GHz, and $2.01-2.53$ GHz ranges with realized gain between $2.39-6.18$ dBi and 3 dB bandwidth between $32^\circ-86^\circ$. The proposed linear four-element array shows return loss < -10 dB in $790-953$ MHz, $1.20-1.88$ GHz, and $1.98-2.59$ GHz ranges with realized gain between $2.96-7.70$ dBi and 3dB bandwidth between $15^\circ-41^\circ$. To the best of authors' knowledge, the proposed linear antenna arrays are the first triple-band designs with mutual coupling compensation.

4.2 Mutual Coupling Compensated Linear Antenna Array of Two Double-Ring Monopoles

4.2.1 Mutual Coupling Compensation

Fig. 4.1a shows the typical layout for microstrip antenna array, while Fig. 4.1b shows the layout of proposed array with mutual coupling compensation. The mutual coupling is compensated by inserting a ground baffle between two antenna elements in Fig. 4.1b. The compensation effect of ground baffle structure has been reported in [26] based on three dimensional dipole arrays, while the research here applies the ground baffle structure to planar microstrip monopole arrays. The simulated insertion loss (S_{12}) between two monopoles with and without ground baffles is compared in Fig. 4.2, and the simulation result shows that ground baffle lowers the insertion loss in 630 MHz$-$3.0 GHz range. The demonstration here sets the spacing D between two antennas to 120 mm and the edge E between antenna element and ground baffle to 10 mm, respectively.

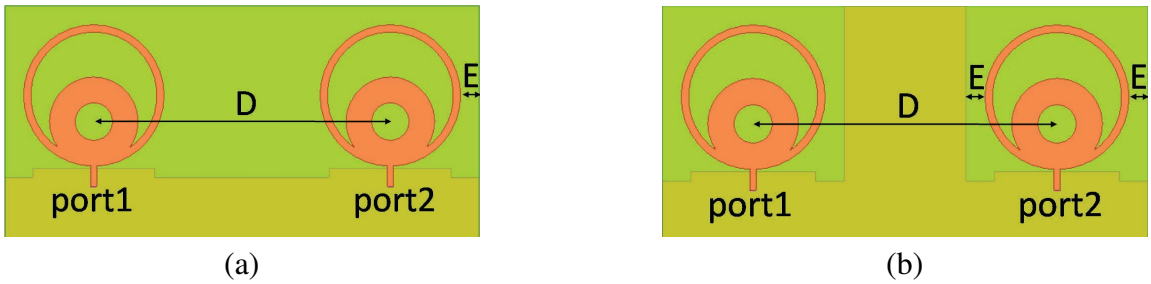

(a) (b)

Figure 4.1: Antenna array of two double-ring monopoles (a) without ground baffle, and (b) with ground baffle.

Less mutual coupling helps to synthesize radiation patterns in multiple frequency bands. Fig. 4.3a and Fig. 4.3b depict the directivity of two-element monopole array without and with ground baffles, respectively. The simulation here sets the edge E between

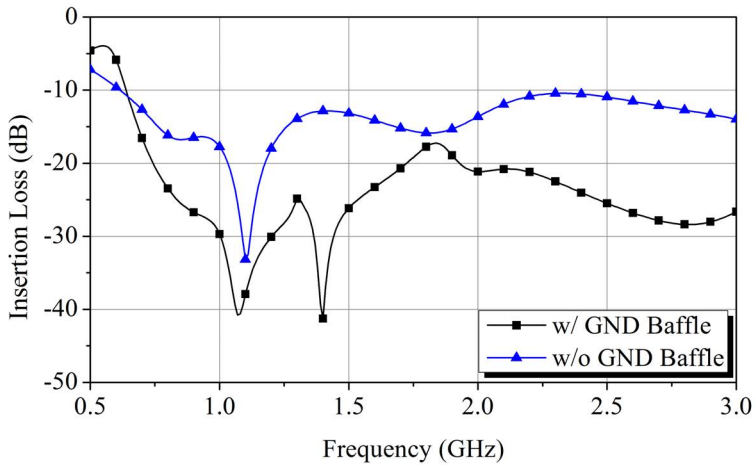

Figure 4.2: Insertion loss (S_{12}) of array of two double-ring monopoles. (D=120 mm, and E=10 mm)

antenna element and ground baffle to 10 mm. In Fig. 4.3, the maximum antenna gain in a particular direction is labeled as Maximum, while the antenna gain in the proposed receiving direction is labeled as Theta = 0. It can be seen that the array structure without ground baffle in Fig. 4.3a can not operate in the proposed receiving direction (Theta = 0) in triple frequency bands, and the directivity fluctuates significantly versus antenna spacing. In contrast, the discrepancy is smaller between the maximum directivity and the directivity in proposed receiving direction, and the directivity versus antenna spacing is more uniform in triple frequency bands, as shown in Fig. 4.3b.

Mutual coupling compensation enables multiband operation but also raises issue in return loss matching. Fig. 4.4 presents the simulated return loss at two antenna terminals, which is identical for both antenna elements due to symmetry. The demonstration here sets the antenna spacing D and the edge E to 120 mm and 10 mm, respectively. The double-ring monopoles in the two-element array with ground baffle has worse return loss, as shown in Fig. 4.4. Fig. 4.5a and Fig. 4.5b studies the impact of edge E on the return loss at antenna terminals and on the synthesized radiation patterns at 2440 MHz.

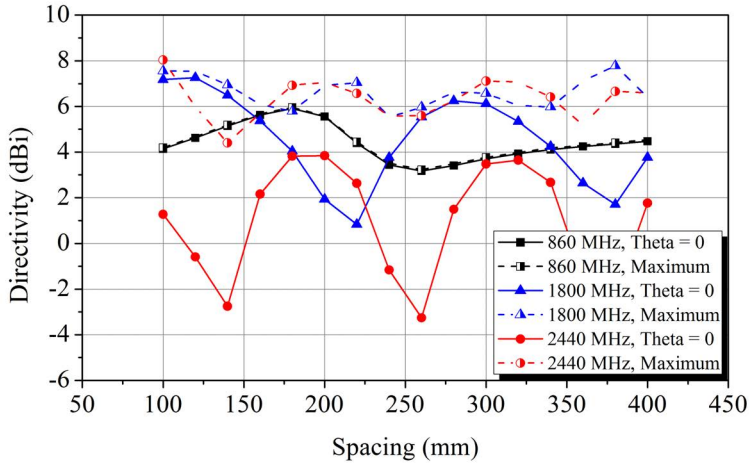

(a)

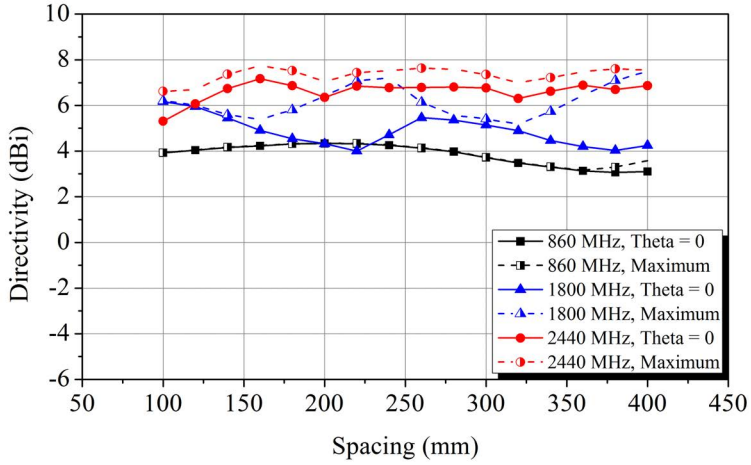

(b)

Figure 4.3: Directivity of array of two double-ring monopoles (a) without ground baffle, and (b) with ground baffle at 860, 1800, and 2440 MHz. (E=10 mm)

When the edge E increases and the ground baffle becomes thinner, the effect of mutual coupling compensation reduces, so the return loss improves as supported in Fig. 4.5a, but the directivity at 2440 MHz reduced in the proposed receiving direction (Theta = 0) as shown in Fig. 4.5b. Here the edge E is chosen as 10 mm to trade-off -10-dB return loss in GSM850/GSM900 frequency bands and directivity at 2440 MHz.

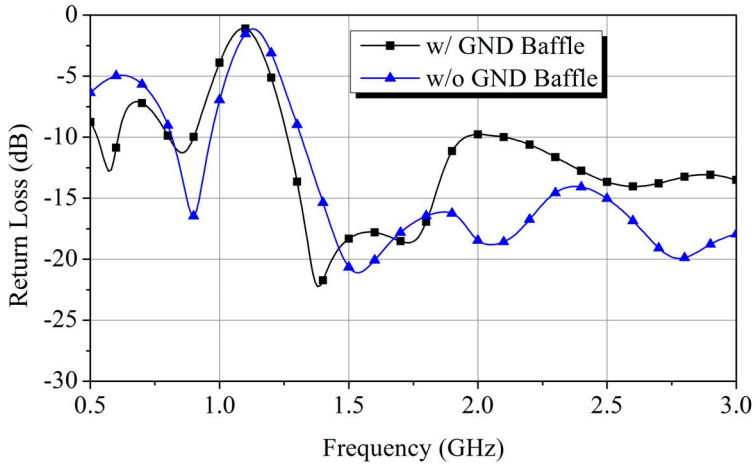

Figure 4.4: Return loss (S_{11}) of array of two double-ring monopoles. (D=120 mm, and E=10 mm)

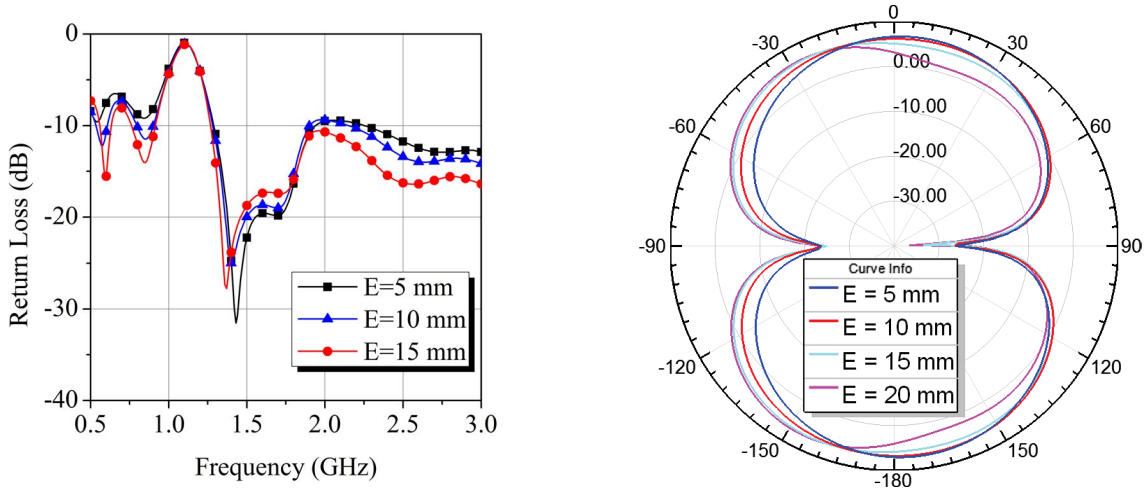

(a) (b)

Figure 4.5: (a) return loss (S_{11}) and (b) directivity at 2440 MHz operating frequency of array of two double-ring monopoles with ground baffle. (D=120 mm)

4.2.2 Effective Directivity

In order to determine the antenna gain fairly, Fig. 4.6 considers the interconnection loss by the additional transmission line with different antenna spacing. The effective directivity

is defined by substracting the directivity from the additional transmission line loss, and the results are plotted in Fig. 4.7. When the spacing in Fig. 4.7 increases in range of 100−160 mm, the effective directivity increases at 2440 MHz but decreases at 1800 MHz. At 860 MHz, the effective directivity changes little in spacing range of 100−260 mm. As a resutl, the antenna spacing D is chosen as 120 mm to trade-off effective directivity in triple frequency bands.

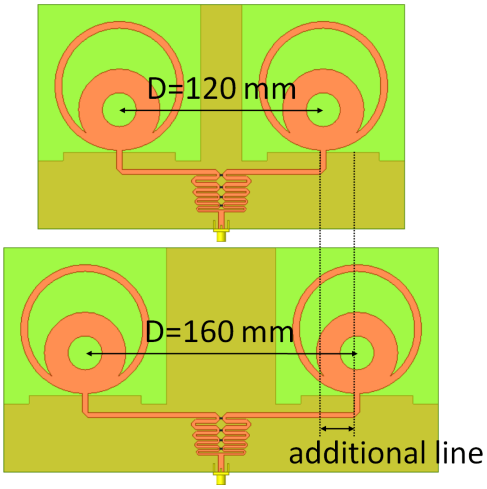

Figure 4.6: Additional transmission line due to different antenna spacing.

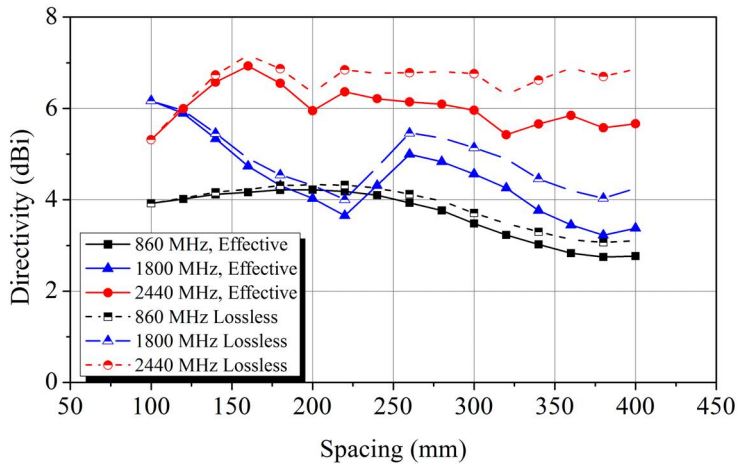

Figure 4.7: Effective directivity versus antenna spacing of array of two double-ring monopoles with ground baffle. (E=10 mm)

4.2.3 Return Loss Matching

Fig. 4.8 shows the schematic of the proposed multiband matching network for the antenna array of two double-ring monopoles, and the layout is shown in Fig. 4.9. The multiband matching network is composed of two short stubs (TL_1), four interconnecting transmission lines (TL_2, TL_3, TL_5), two open stubs (TL_4), and a two-way broadband Wilkinson power combiner. The triple-band return loss matching flows in 820−920 MHz, 1.7−1.9 GHz, and 2.40−2.48 GHz frequency ranges are demonstrated in Fig. 4.10. Fig. 4.11 plots the return loss of the proposed array of two double-ring monopoles with multiband matching. The simulated return loss is lower than −10 dB in 775−955 MHz and 1.25−2.59 GHz frequency ranges. Table 4.1 lists the dimension of the proposed multiband matching network, and the dimension of the broadband Wilkinson power combiner can refer from Table 3.3.

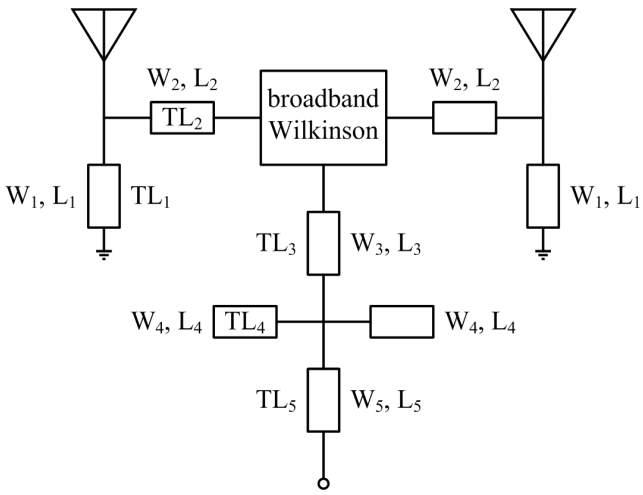

Figure 4.8: Schematic of the proposed two-way multiband matching network.

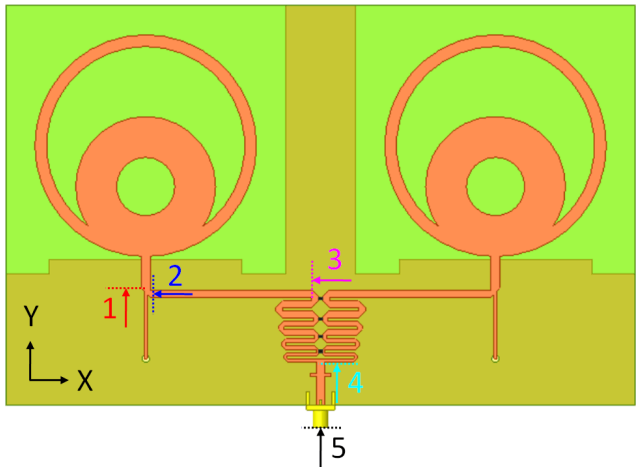

Figure 4.9: Layout of the proposed array of two double-ring monopoles.

Table 4.1: Parameters of the two-way multiband matching network.

TL_1	W_1	1 mm	L_1	27 mm
TL_2	W_2	3 mm	L_2	55 mm
TL_3	W_3	3 mm	L_3	4 mm
TL_4	W_4	1 mm	L_4	2 mm
TL_5	W_5	3 mm	L_5	10 mm

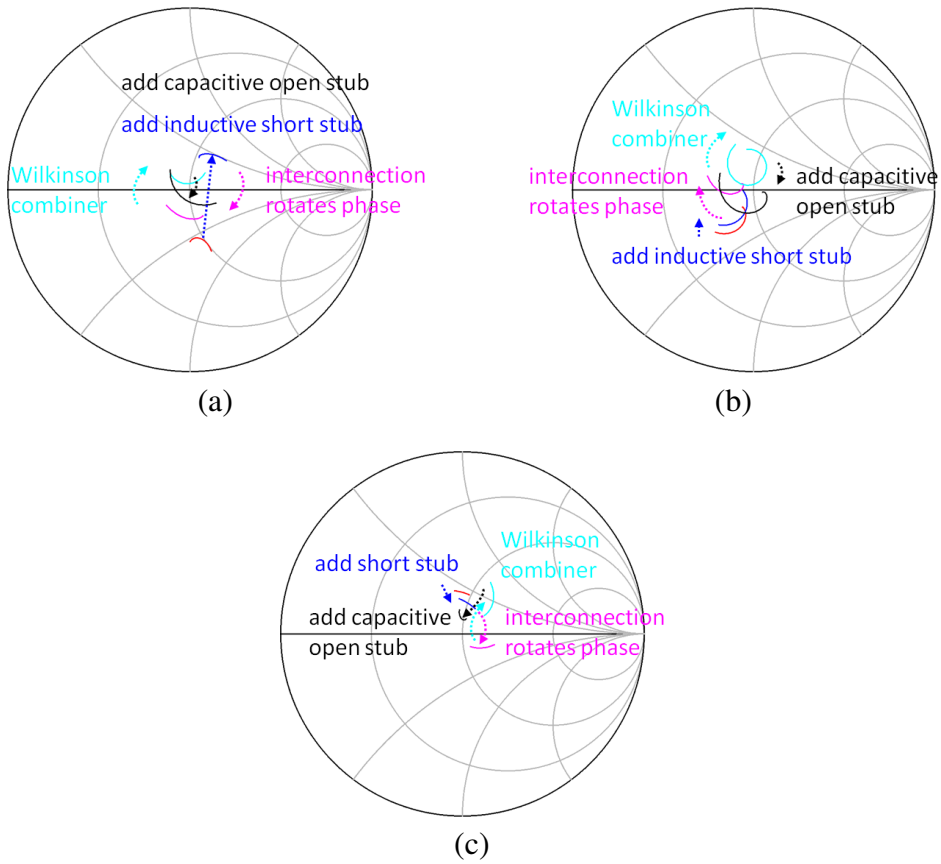

Figure 4.10: Return loss matching flow in (a) 820−920 MHz, (b) 1.7−1.9 GHz, and (c) 2.40−2.48 GHz frequency ranges

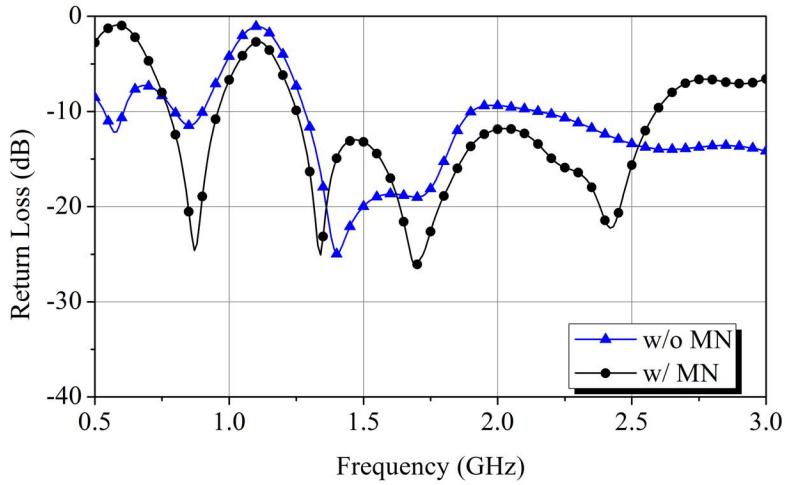

Figure 4.11: Return loss of the proposed array of two double-ring monopoles.

4.2.4 Radiation Patterns

The mutual coupling compensation by ground baffle structure synthesizes radiation patterns toward Z axis in triple frequency bands, as shown in Fig. 4.12, Fig. 4.13, and Fig. 4.14, respectively. The antenna is placed on the XY plane as shown in Fig. 4.9. The simulated total realized gain is 3.58 dBi, 4.99 dBi, and 4.16 dBi at 860 MHz, 1800 MHz, and 2440 MHz, respectively. The simulated efficiency is 86.1% at 860 MHz, 77.0% at 1800 MHz, and 70.1% at 2440 MHz. Table 4.2 lists simulation results at start frequency, center frequency, and stop frequency of triple frequency bands. The disadvantage by ground baffle structure is the synthesized gain toward Z axis at 1.9 GHz, which is 2.93 dBi.

Table 4.2: Simulated performance of the proposed array of two double-ring monopoles.

Frequency (GHz)	Gain at Z axis (dBi)	Return Loss (dB)	Efficiency (%)
0.82	3.18	-14.95	84.70
0.86	3.58	-22.93	86.12
0.92	3.92	-14.90	83.80
1.70	5.48	-26.08	80.45
1.80	4.99	-18.87	76.95
1.90	2.93	-13.65	72.32
2.40	3.92	-21.43	70.35
2.44	4.16	-21.53	70.09
2.48	4.35	-17.53	68.56

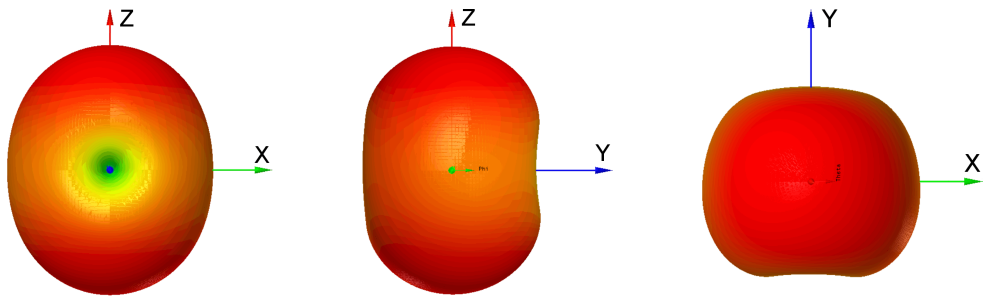

(a) (b) (c)

Figure 4.12: Realized gain at 860 MHz in (a) XZ plane, (b) YZ plane, and (c) XY plane

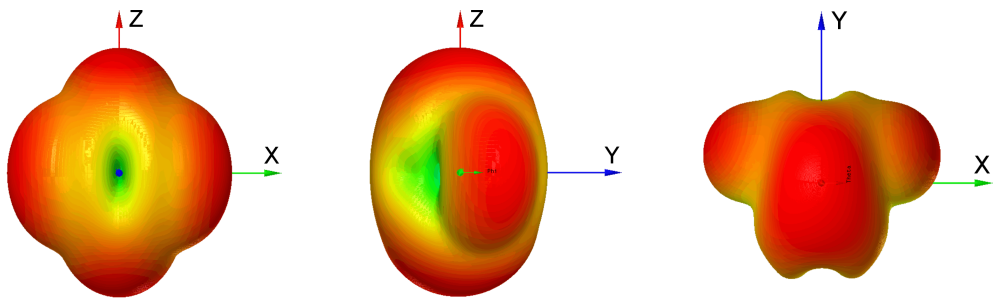

(a) (b) (c)

Figure 4.13: Realized gain at 1800 MHz in (a) XZ plane, (b) YZ plane, and (c) XY plane

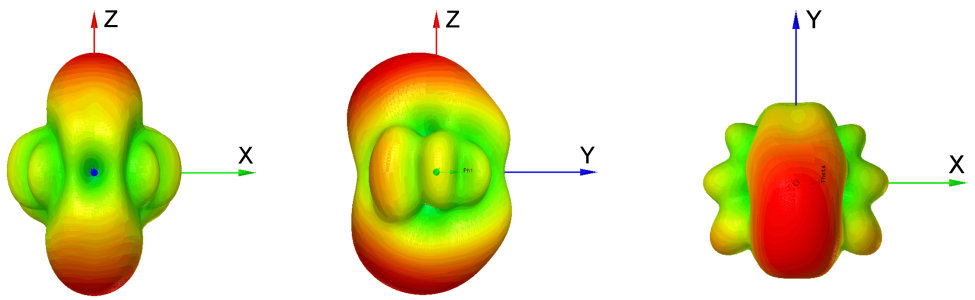

(a) (b) (c)

Figure 4.14: Realized gain at 2440 MHz in (a) XZ plane, (b) YZ plane, and (c) XY plane

4.3 Mutual Coupling Compensated Linear Antenna Array of Four Double-Ring Monopoles

4.3.1 Mutual Coupling Compensation

Similar to the design of array of two double-ring monopoles, ground baffle structure is applied to the proposed linear antenna array of four double-ring monopoles, as shown in Fig. 4.15. The demonstration here sets the spacing D to 120 mm and the edge E to 10 mm. Mutual coupling effect varies according to the location of antenna element. Generally, the mutual coupling between non-adjacent ports (port1 and port4 or port2 and port4) is weaker, while the mutual coupling between adjacent ports (port1 and port2 or port2 and port3) is stronger. The simulated insertion loss between all combinations of ports is shown in Fig. 4.16a and Fig. 4.16b, which confirms that inserting ground baffle between antenna elements compensates mutual coupling.

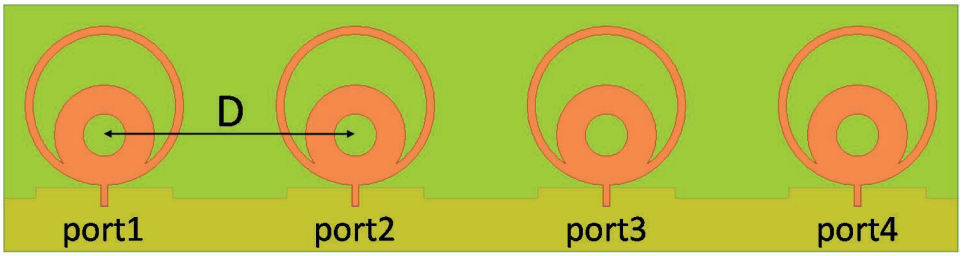

(a)

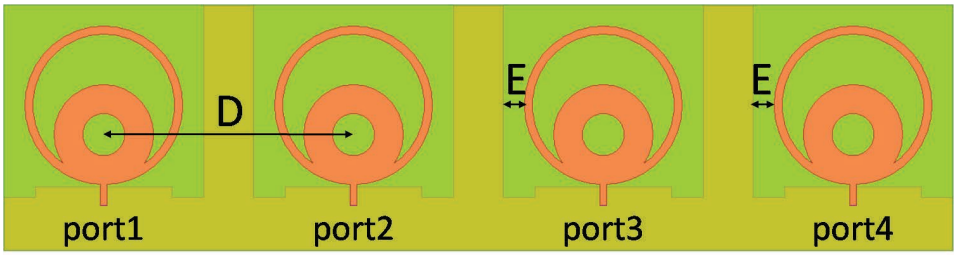

(b)

Figure 4.15: Linear antenna array of four double-ring monopoles (a) without ground baffle, and (b) with ground baffle.

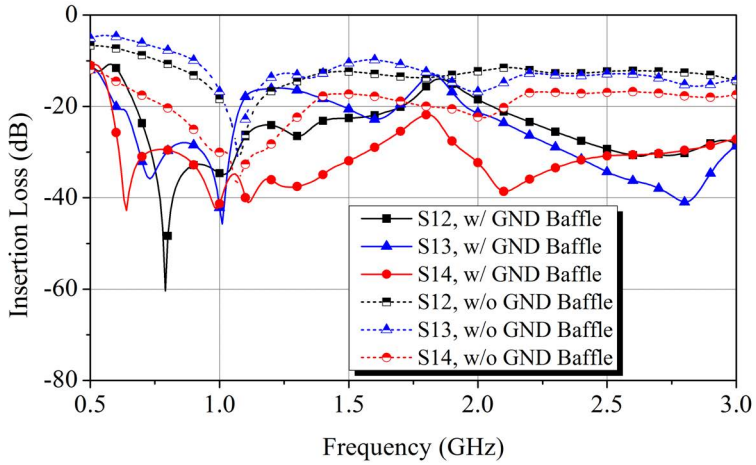

(a)

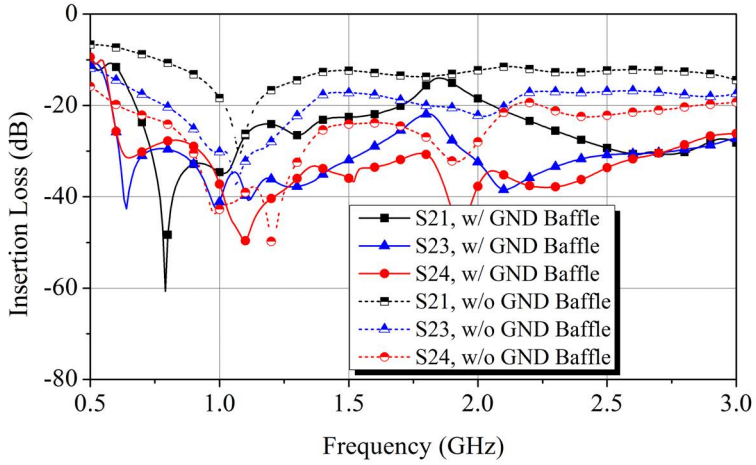

(b)

Figure 4.16: Insertion loss of four double-ring monopoles in a linear array at (a) port 1, and (b) port 2. (D=120 mm, and E=10 mm)

Fig. 4.17 shows the return loss at terminals of four double-ring monopoles in a linear array, and the simulation here sets the spacing D to 120 mm. Because the antenna array is symmetric, the return loss at port 1 is equivalent to the one at port4, and the return loss at port 2 is equivalent to the one at port 3. Based on the results in Fig. 4.17, the edge E is chosen as 10 mm for -10 dB return loss at port 2 in GSM850/GSM900 frequency bands.

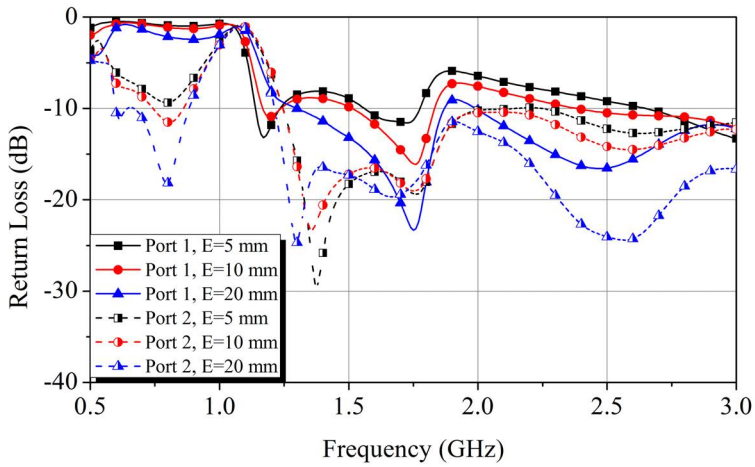

Figure 4.17: Return loss at port 1 and port 2 of four double-ring monopoles in a linear array. (D=120 mm)

Mutual coupling compensation on radiation patterns at different operating frequencies is discussed in Fig. 4.18. The definition of directivity difference is introduced to compare the directivity before and after compensation:

$$D_{\text{diff}} = D_{\text{w/ GND baffle}} - D_{\text{w/o GND baffle}} \tag{4.1}$$

where D_{diff} is the directivity difference (in dB), $D_{\text{w/ GND baffle}}$ is the directivity with ground baffle along $\theta = 0$ direction (in dBi), and $D_{\text{w/o GND baffle}}$ is the directivity without ground baffle along $\theta = 0$ direction (in dBi). As shown in Fig. 4.18, the directivity difference is > 0 dB in spacing range of 100−400 mm at 2440 MHz and in spacing ranges of 100−120 mm and 160−400 mm at 1800 MHz, while the directivity difference is < 0 dB at 860 MHz except in spacing range of 280−360 mm. Consequently, ground baffle structure helps to synthesize radiation patterns in triple frequency bands in spacing range of 280−360 mm.

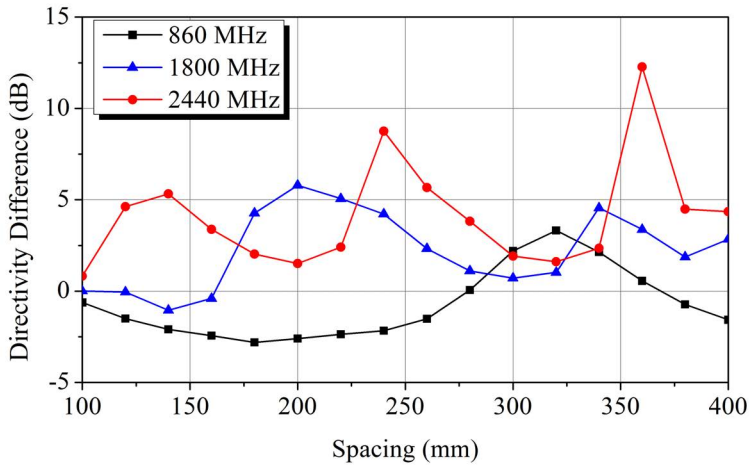

Figure 4.18: Directivity difference between linear array of four double-ring monopoles with and without ground baffle.

4.3.2 Effective Directivity

The effective directivity in consideration of the additional interconnection loss due to different antenna spacing is shown in Fig. 4.19. According to the results in Fig. 4.19, the antenna spacing D is chosen as 120 mm for the maximum effective directivity in triple frequency bands. Fig. 4.20 compares the effective directivity between array of two elements and linear array of four elements. As shown in Fig. 4.20, the directivity improvement with array of four elements varies between 1.3−4.1 dB, thus the linear array of four elements can harvest more RF ambient power compared to the array of two elements.

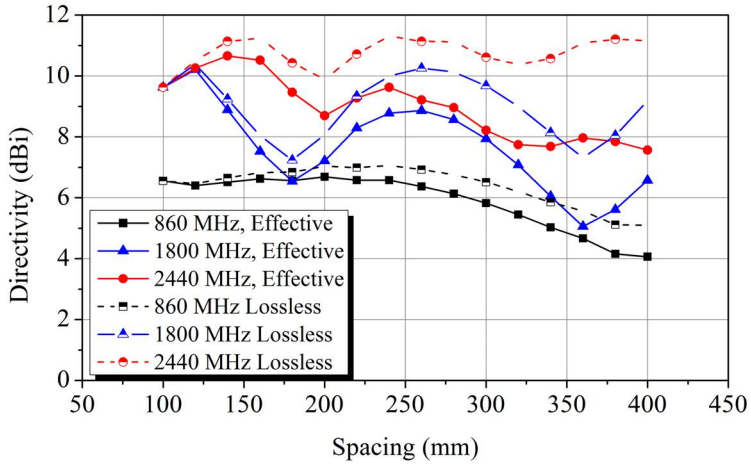

Figure 4.19: Effective directivity of array of four double-ring monopoles with ground baffle. (E=10 mm)

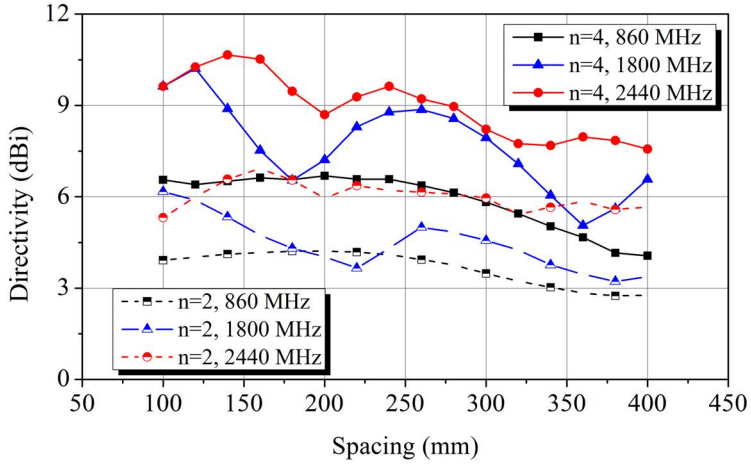

Figure 4.20: Effective directivity of mutual coupling compensated arrays of two (n=2) and of four (n=4) double-ring monopoles. (E=10 mm)

4.3.3 Return Loss Matching

The schematic of the proposed multiband matching network for the antenna array of four double-ring monopoles is shown in Fig. 4.8, and the layout is shown in Fig. 4.9. The

multiband matching network is composed of eight short stubs (TL_1, TL_3), ten interconnecting transmission lines (TL_2, TL_4, TL_5, TL_7), two open stubs (TL_6), and a four-way RF energy combiner. The simulated return loss is lower than -10 dB in $815-955$ MHz, $1.22-1.92$ GHz, and $2.08-2.56$ GHz frequency ranges. Table 4.3 lists the dimension of the proposed multiband matching network, and the dimension of the four-way RF energy combiner is listed in Table 3.5.

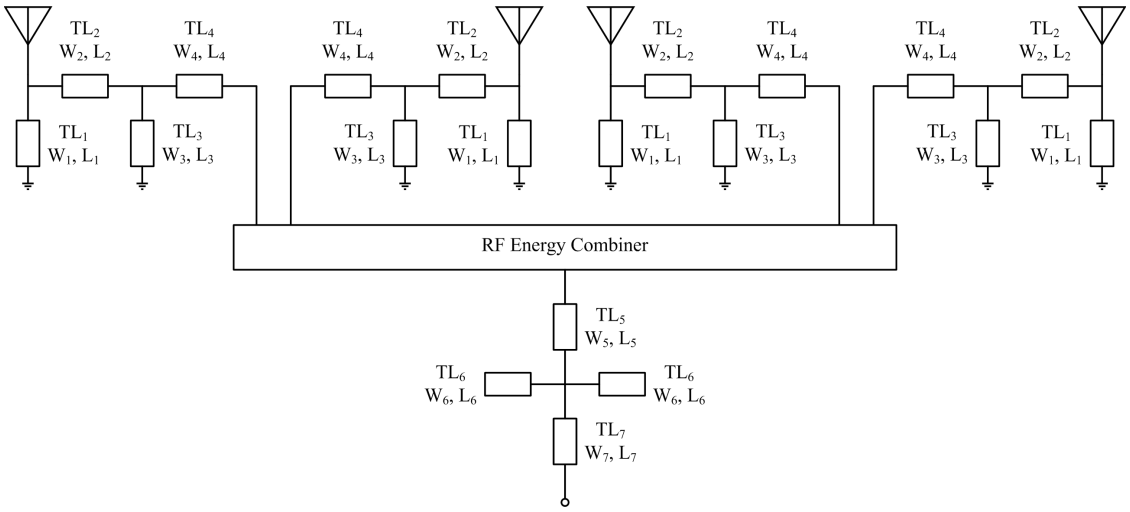

Figure 4.21: Schematic of the proposed four-way multiband matching network.

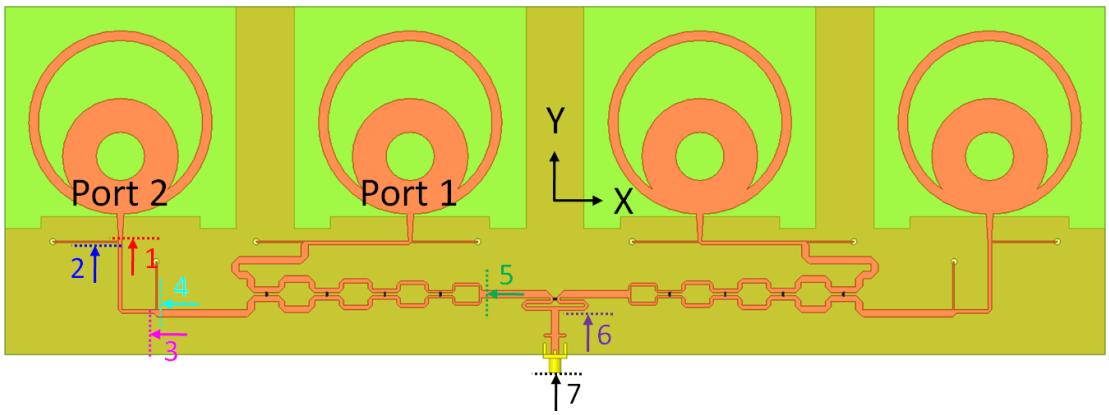

Figure 4.22: Layout of the proposed linear array of four double-ring monopoles.

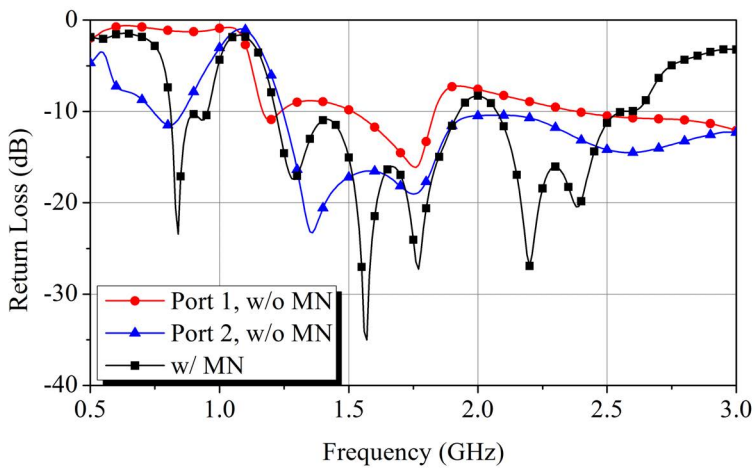

Figure 4.23: Return loss of the proposed array of four double-ring monopoles with multi-band matching.

Table 4.3: Parameters of the four-way multiband matching network.

TL_1	W_1	0.5 mm	L_1	27 mm
TL_2	W_2	1.5 mm	L_2	43 mm
TL_3	W_3	0.5 mm	L_3	19 mm
TL_4	W_4	3 mm	L_4	40.25 mm
TL_5	W_5	3 mm	L_5	10 mm
TL_6	W_6	1 mm	L_6	3 mm
TL_7	W_7	3 mm	L_7	7.5 mm

4.3.4 Radiation Patterns

Fig. 4.24, Fig. 4.25, and Fig. 4.26 plot the radiation patterns toward Z axis in triple frequency bands. The antenna array is placed on the XY plane as shown in Fig. 4.22. The simulated total realized gain is 5.02 dBi, 7.60 dBi, and 5.90 dBi at 860 MHz, 1800 MHz, and 2440 MHz, respectively. The simulated efficiency is 61.22% at 860 MHz, 61.26% at 1800 MHz, and 48.75% at 2440 MHz. Table 4.4 lists simulation results at start frequency, center frequency, and stop frequency of triple frequency bands. The disadvantage by ground baffle structure is the low synthesized gain toward Z axis at 0.82 GHz and 1.9 GHz.

Table 4.4: Simulated performance of the proposed array of four double-ring monopoles.

Frequency (GHz)	Gain at Z axis (dBi)	Return Loss (dB)	Efficiency (%)
0.82	3.15	-14.73	51.89
0.86	5.02	-13.22	61.22
0.92	5.81	-10.19	62.91
1.70	8.42	-16.91	64.56
1.80	7.60	-24.93	61.26
1.90	2.95	-13.06	47.00
2.40	6.33	-21.23	50.96
2.44	5.90	-15.59	48.75
2.48	5.61	-11.89	45.66

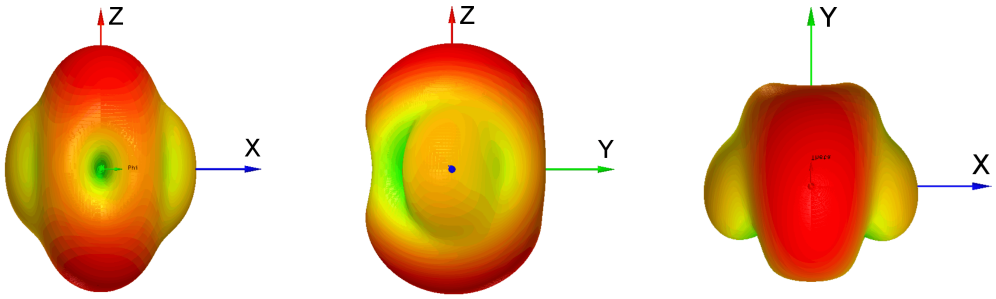

(a) (b) (c)

Figure 4.24: Realized gain at 860 MHz in (a) XZ plane, (b) YZ plane, and (c) XY plane

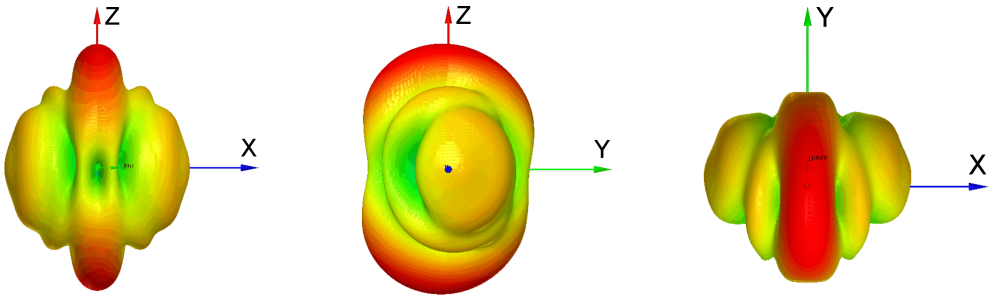

(a) (b) (c)

Figure 4.25: Realized gain at 1800 MHz in (a) XZ plane, (b) YZ plane, and (c) XY plane.

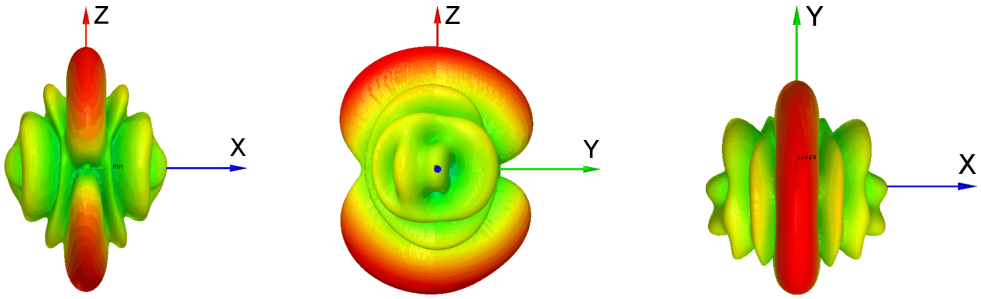

(a) (b) (c)

Figure 4.26: Realized gain at 2440 MHz in (a) XZ plane, (b) YZ plane, and (c) XY plane.

4.4 Fabrication and Experimental Results

Photographs of the fabricated antenna arrays are shown in Fig. 4.27a and Fig. 4.27b. The antenna arrays are designed on standard FR4 material ($\epsilon_r = 4.4$, $tan\delta = 0.021$), and the substrate thickness is 1.6 mm. The dimension of two-element array is 216 mm $\times$ 137 mm, which can perfectly fit to the ipad mini by cutting out excessive outer edges. The dimension of four-element array is 456 mm $\times$ 147 mm, which is slightly longer than 17.3" laptops. The return loss of the fabricated antenna arrays is measured via the Agilent N5230A calibrated vector network analyzer (VNA), and the results are shown in Fig. 4.28a and Fig. 4.28b, respectively. The proposed two-element array shows return loss < -10 dB in 726$-$924 MHz, 1.24$-$1.87 GHz, and 2.01$-$2.53 GHz ranges, while the proposed four-element array shows return loss < -10 dB in 790$-$953 MHz, 1.20$-$1.88 GHz, and 1.98$-$2.59 GHz ranges. Return loss measurement of the proposed two antenna arrays in Fig. 4.28 depicts wideband/multiband features, and the return loss discrepancy around 2.4 GHz diminishes with larger ground area.

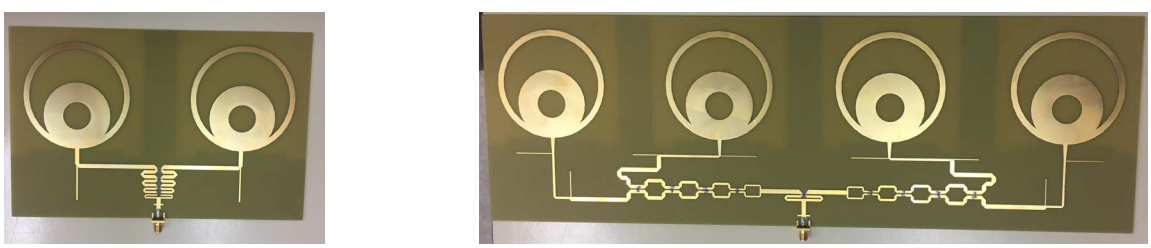

(a) (b)

Figure 4.27: Photographs of (a) the proposed array of two elements, and (b) the proposed linear array of four elements.

The realized gain, radiation pattern, and efficiency are measured via the chamber at Texas A&M University. The antenna arrays are placed on XY plane with longer sides

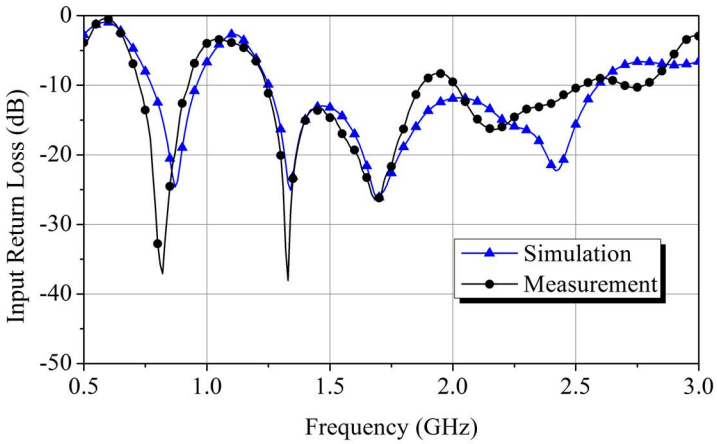

(a)

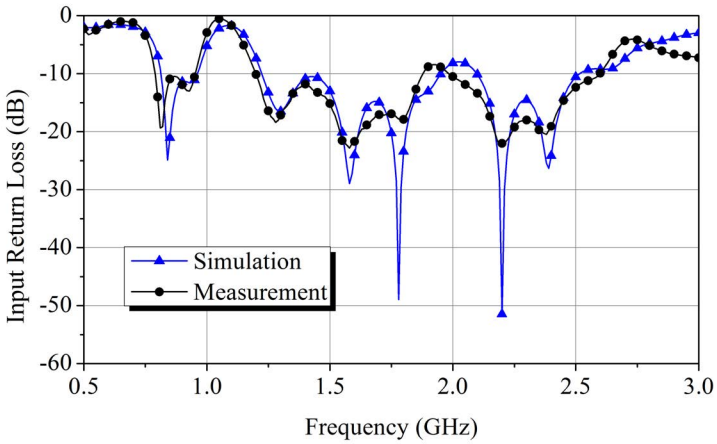

(b)

Figure 4.28: Measured return loss of (a) the proposed array of two elements, and (b) the proposed linear array of four elements.

aligned to X axis, and the antenna elements are polarized along Y axis. The normalized radiation patterns in XZ-plane and YZ-plane at 860 MHz, 1.8 GHz, and 2.44 GHz of the proposed two-element array are plotted in Fig. 4.29, and the corresponding ones of the proposed four-element array are plotted in Fig. 4.30. The measured co-polarization (Co-Pol) patterns follow simulation results very accurate for both two-element array and four-element array, while the discrepancy between measured and simulated cross-polarization

(X-Pol) patterns in YZ-plane is mainly due to the physical alignment issue. The cross-polarization simulation in YZ-plane assumes perfect PCB alignment, and only one degree mismatch can introduce up to 20-dB gain increment. Both laser level and bubble level are applied in the measurement setup to improve alignment accuracy, but the inherent PCB curve due to fabrication is not able to calibrate. The measured XZ-plane and YZ-plane co-polarization patterns as shown in Fig. 4.29 and Fig. 4.30 confirm that the synthesized array main beams are toward Z axis in multiple frequency bands. The measured realized gains of the proposed two-element array are 2.46 dBi at 860 MHz, 3.58 dBi at 1.8 GHz, and 6.18 dBi at 2.44 GHz with corresponding 3 dB bandwidth of 86°, 34°, and 32°, respectively. The measured realized gains of the proposed four-element array are 3.96 dBi at 860 MHz, 7.52 dBi at 1.8 GHz, and 7.70 dBi at 2.44 GHz with corresponding 3 dB bandwidth of 41°, 18°, and 15°, respectively. Table 4.5 compares the realized gain of single antenna, array of two elements, and array of four elements. Generally, the four-element array achieves the highest gain. The gain difference defined in Table 4.5 is the maximum realized gain at a particular direction minus the realized gain at Z axis, thus low gain difference means that the maximum gain is aligned to the designated operating direction. The measured efficiencies of the proposed two-element array are 81.7% at 860 MHz, 91.2% at 1.8 GHz, and 75.7% at 2.44 GHz, while the corresponding values of the proposed four-element array are 82.7%, 62.4%, and 48.9%, respectively. The low efficiency of the proposed four-element array is due to FR4 substrate loss via longer interconnection, and the proposed antenna arrays can achieve higher realized gains if using low loss substrate material such as Rogers. Detailed efficiency measurement results are listed in Table 4.6.

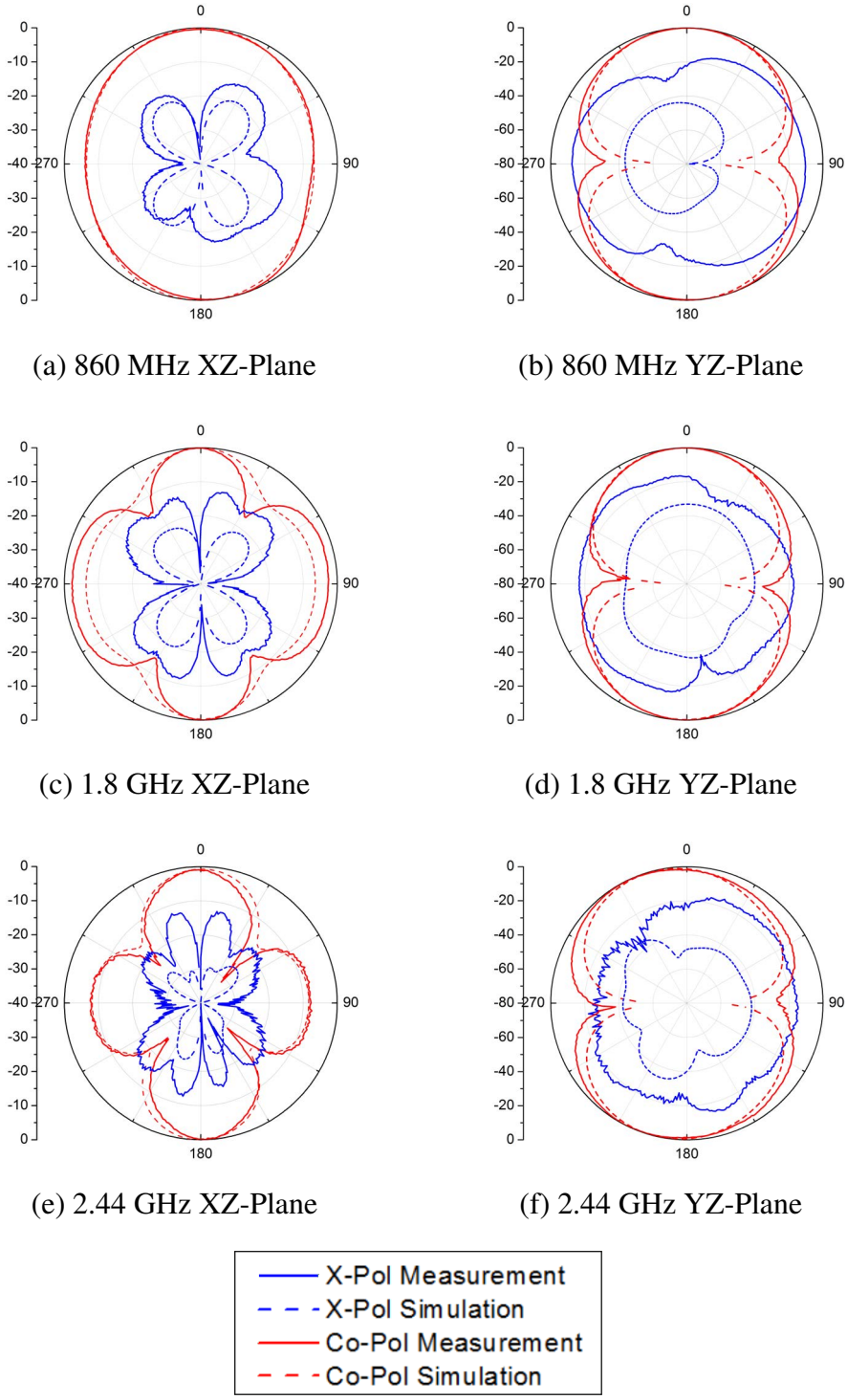

(a) 860 MHz XZ-Plane

(b) 860 MHz YZ-Plane

(c) 1.8 GHz XZ-Plane

(d) 1.8 GHz YZ-Plane

(e) 2.44 GHz XZ-Plane

(f) 2.44 GHz YZ-Plane

Figure 4.29: Normalized XZ-plane and YZ-plane radiation patterns of two-element array at 860 MHz, 1.8 GHz, and 2.44 GHz

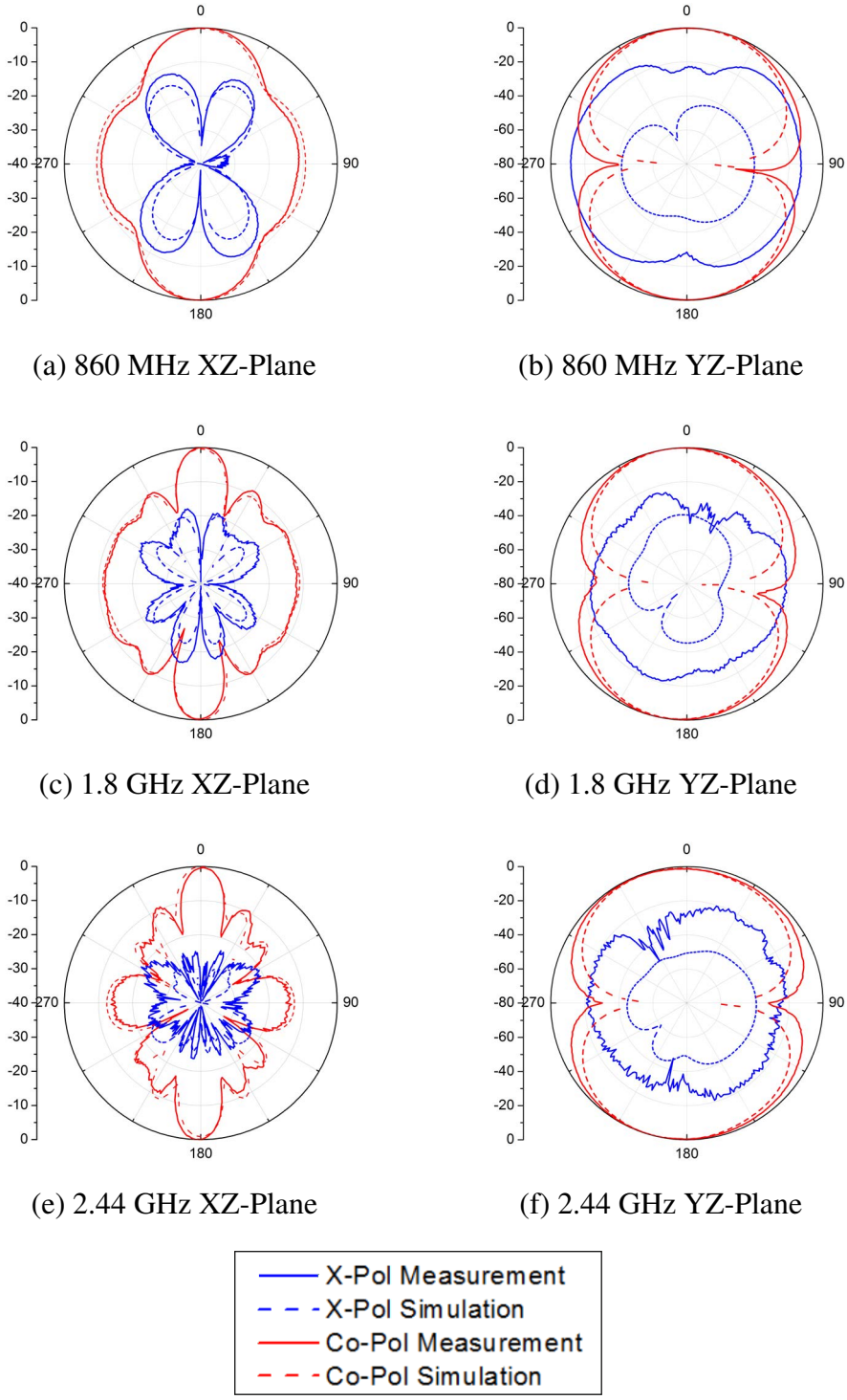

(a) 860 MHz XZ-Plane

(b) 860 MHz YZ-Plane

(c) 1.8 GHz XZ-Plane

(d) 1.8 GHz YZ-Plane

(e) 2.44 GHz XZ-Plane

(f) 2.44 GHz YZ-Plane

Figure 4.30: Normalized XZ-plane and YZ-plane radiation patterns of four-element array at 860 MHz, 1.8 GHz, and 2.44 GHz

Table 4.5: Realized Gain of Single Double-Ring Monopole, Array of Two Double-Ring Monopoles, and Linear Array of Four Double-Ring Monopoles

Element	1	2	4	1	2	4	1	2	4	1	2	4
Frequency (MHz)	Measured Realized Gain (G_{max}, dBi)			Simulated Realized Gain (G_{max}, dBi)			Measured Gain Difference ($G_{max-\theta=0^\circ}$, dB)			Simulated Gain Difference ($G_{max-\theta=0^\circ}$, dB)		
820	1.36	2.41	3.65	2.20	3.34	3.09	0	0.67	0.19	0	0.16	0.01
860	1.45	2.46	3.96	2.57	3.66	5.02	0.77	0.51	0	0	0.08	0.01
920	1.09	2.39	4.61	2.62	3.91	5.82	0.26	0.43	0.02	0	0	0.05
1700	1.16	4.51	7.23	3.07	5.71	9.05	0.09	0	0.04	0.44	0.23	0.70
1800	1.73	3.58	7.52	3.27	5.01	7.78	1.10	0.11	0	0.45	0.02	0.30
1900	2.07	3.63	2.96	3.41	3.12	3.97	0.01	0.23	1.00	0.52	0.19	0.93
2400	1.06	5.34	7.29	3.59	5.56	6.86	N.A.	1.04	0.62	5.58	1.64	0.95
2440	0.98	6.18	7.70	3.63	5.74	6.99	N.A.	1.06	0.49	5.23	1.58	1.50
2480	1.32	6.00	7.05	3.60	5.86	7.02	N.A.	0.65	0.51	4.62	1.51	1.68

Table 4.6: Efficiency of Single Double-Ring Monopole, Array of Two Double-Ring Monopoles, and Linear Array of Four Double-Ring Monopoles

Element	1	2	4	1	2	4
Frequency (MHz)	Measured Efficiency (%)			Simultaed Efficiency (%)		
820	84.7	80.9	75.2	90.6	84.7	51.9
860	91.8	81.7	82.7	94.8	86.1	61.2
920	84.4	86.5	70.5	90.1	83.8	62.9
1700	77.1	80.7	53.3	92.5	80.5	64.6
1800	83.0	91.2	62.4	92.2	77.0	61.3
1900	93.1	79.5	62.5	92.5	72.3	47.0
2400	87.5	73.8	48.6	87.6	70.4	51.0
2440	78.9	75.7	48.9	87.9	70.1	48.8
2480	76.7	74.5	45.9	88.6	68.6	45.7

4.5 Conclusions

Antenna array can increase the captured or radiated RF power with proper physical alignment, matched polarization, high directivity, and high efficiency. Mutual coupling compensated linear antenna arrays of two and of four double-ring monopoles are proposed to synthesize radiation patterns in triple frequency bands for multiband RF energy harvesting/transfer applications. Ground baffles are inserted between antenna elements to compensate mutual coupling, while the effective gain is defined to determine the optimum antenna spacing. Radiation patterns are synthesized at triple frequency bands at the cost of return loss matching at each antenna terminal, and the base antennas are re-matched to 50Ω by broadband matching networks. The proposed two-element array shows return loss < -10 dB in $726-924$ MHz, $1.24-1.87$ GHz, and $2.01-2.53$ GHz ranges with realized gain varying between $2.39-6.18$ dBi and 3 dB bandwidth varying between $32^\circ-86^\circ$. The proposed four-element linear array shows return loss < -10 dB in $790-953$ MHz, $1.20-1.88$ GHz, and $1.98-2.59$ GHz ranges with realized gain varying between $2.96-7.70$ dBi and 3 dB bandwidth varying between $15^\circ-41^\circ$. To the best of authors' knowledge, the proposed linear antenna arrays are the first aim for triple-band RF energy harvesting/transfer.

5. A SIX-STAGE TRIPLE-BAND AND WIDEBAND RF-DC RECTIFIER

5.1 Circuit Design

A matching approach is introduced in [36] to design multiband RF-DC rectifier. The proposed technique allows independent design of resonance frequencies, but the return loss bandwidth of the implemented circuit is limited, and the power conversion efficiency in multitone operation is not reported. Therefore, a both triple-band and wideband six-stage RF-DC rectifier is proposed for multitone RF energy harvesting application. Fig. 5.1a uses a two-stage Dickson charge pump with LC matching to demonstrate the resonance frequency design. Different from the conventional Dickson charge pump, an inductor L is inserted in series with the stage capacitor, as shown in Fig. 5.1a. Two capacitors C and the inductor L forms a series LC tank, and the lower resonance frequency can be determined by:

$$f_{\text{rsc}} = \frac{1}{2\pi\sqrt{2LC}} \tag{5.1}$$

where f_{rsc} is the lower resonance frequency (in Hz), L is the inductance (in H), and C is the capacitance (in F). The stage capacitor in Fig. 5.1a acts as AC short and has no influence on the resonance frequency if large enough value is chosen. The implementation of capacitance C can be either the parasitic from diode or the real capacitor.

Fig. 5.1b presents the proposed circuit topology to generate triple resonances with a three-stage Dickson charge pump. The capacitor C in Fig. 5.1a is realized by diode's parasitic capacitor or C_2 in Fig. 5.1b. RF Schottky diode HSMS-285C made by Broadcom/Avago is selected for circuit implementation. L_1 with C_2, L_2 with C_2, and L_3 with C_2 contribute to three lower resonances, respectively. The electrical length of interconnec-

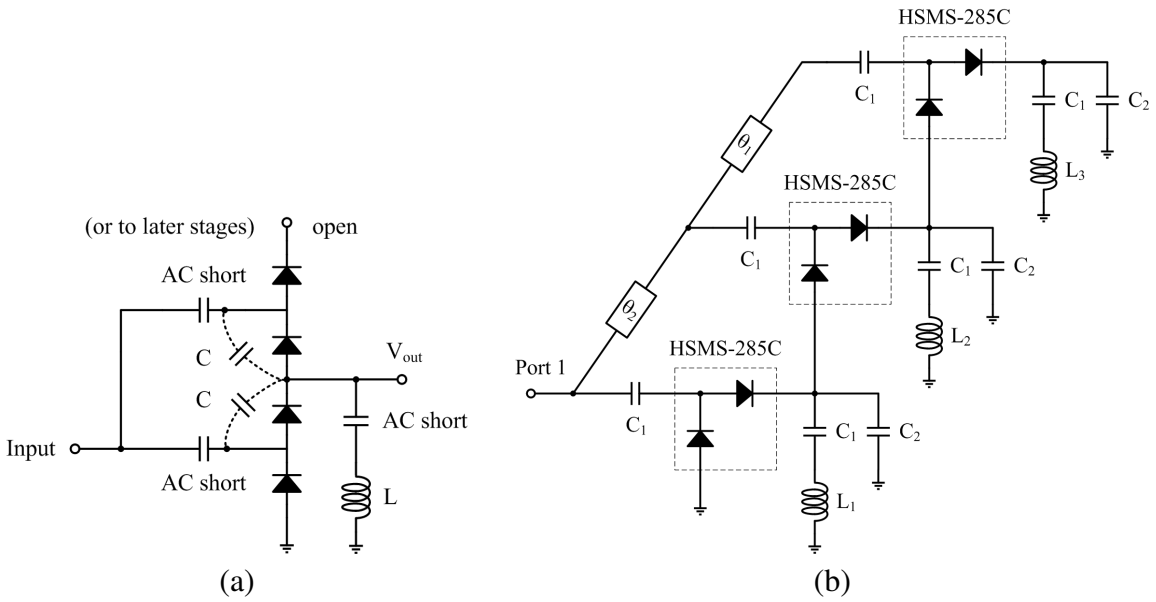

Figure 5.1: (a) Two-stage Dickson charge pump with LC matching, and (b) proposed Dickson charge pump topology with LC matching.

Table 5.1: LC values of the 3-stage Dickson charge pump.

	without C_2	$C_2 = 0.5pF$	$C_2 = 3pF$
L_1	58.7 nH	31.4 nH	9.8 nH
L_2	13.4 nH	7.2 nH	2.2 nH
L_3	12.3 nH	5.1 nH	1.3 nH

tion lines θ_1 and θ_2 is another parameter that affects the return loss, but the analysis here does not put this effect into consideration. Fig. 5.2a shows the return loss evolution with parasitic capacitors (C_2 is open) and different number of inductors. The first resonance frequency is set to 860 MHz with L_1 of 58.7 nH only while L_2 and L_3 are shorted. The dual resonances at 860 MHz and 1800 MHz are generated with L_1 and L_2 of 13.4 nH while L_3 is shorted, and the resonance at 860 MHz is remained intact. Similarly, triple resonances at 860 MHz, 1800 MHz, and 2440 MHz are generated with L_1, L_2, and L_3 of

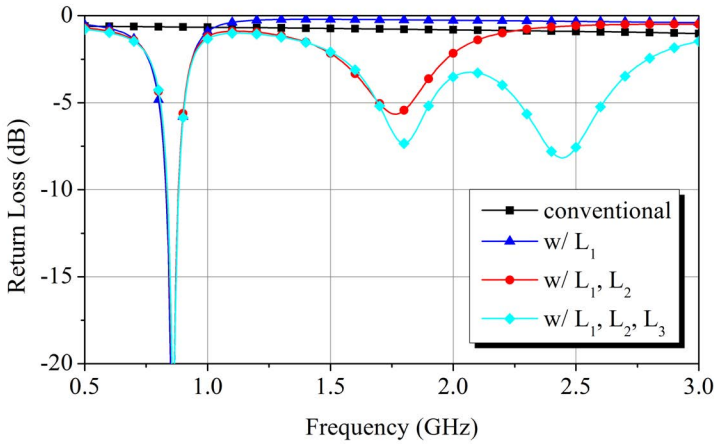

(a)

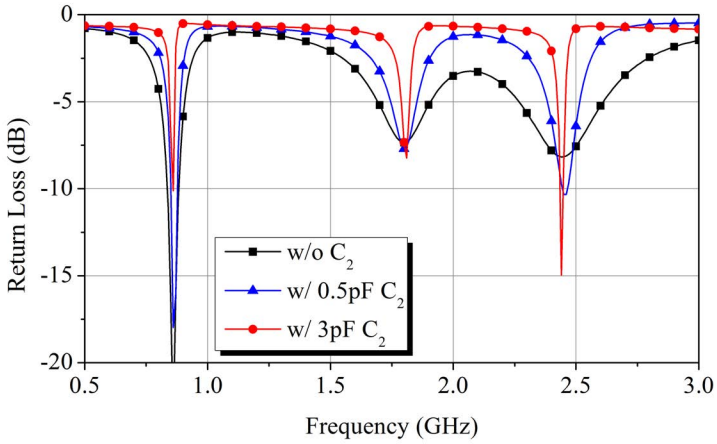

(b)

Figure 5.2: (a) Triple resonances design flow without C_2, and (b) comparison of triple resonances with and without C_2.

12.3 nH as shown in Fig. 5.2a. The simulated parasitic capacitance from HSMS-285C is 327 fF, and C_1 of 200 pF is the stage capacitor which can be omitted in the return loss analysis.

The capacitor C_2 in Fig. 5.1b can reduce the required inductance with the same resonance frequency, thus this approach can be directly applied to IC technology. Fig. 5.2b compares the generated triple resonances with and without C_2, and the simulation re-

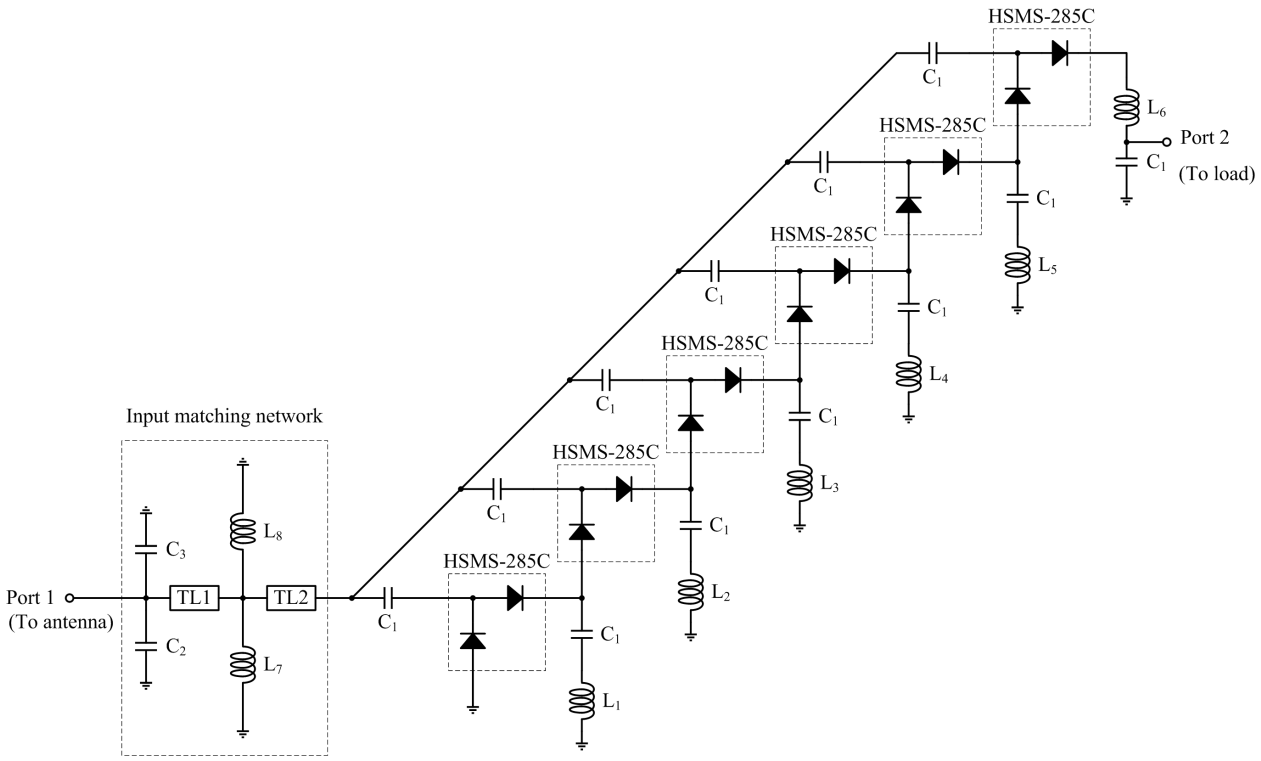

Figure 5.3: Schematic of the proposed six-stage triple-band and wideband RF-DC rectifier.

sult shows that the required inductance can reduce 6.1 times with C_2 of 3pF. However, the design here choose to utilize parasitic capacitor from diodes due to the commercial availability of discrete inductors with ultra small inductance. Table 5.1 summarized the required inductor values for triple resonances at 860 MHz, 1800 MHz, and 2440 MHz.

The schematic of the proposed six-stage triple-band and wideband RF-DC rectifier is presented in Fig. 5.3. Wideband feature is created by generating two resonances which are closer to each other. The lower and higher resonances in 860 MHz band are created by L_5 and L_3, respectively. The lower resonance in 1800 MHz band is generated by L_2 and L_4, while the higher resonance in 1800 MHz band is determined by L_6. L_1 produces the resonance at 2440 MHz. Fig. 5.4a demonstrates the simulated input return loss, and Table 5.2 lists the component values which meet the commercial availability. L_1 of 4.35

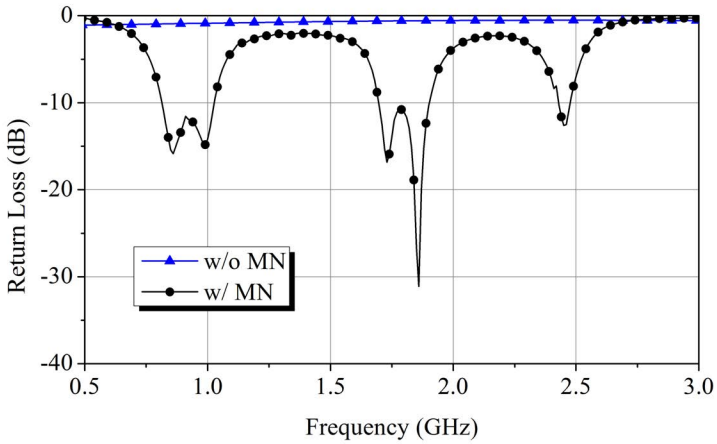

(a)

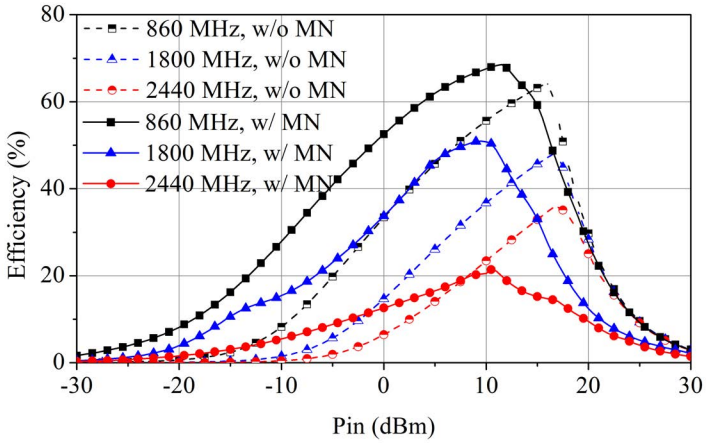

(b)

Figure 5.4: (a) Return loss, and (b) efficiency with and without matching.

nH in Table 5.2 is implemented by two 8.7-nH inductors in parallel. Fig. 5.4b compares the simulated power conversion efficiency (PCE) with and without matching. The most important reason for matching is the sensitivity improvement. As shown in Fig. 5.4b, there is up to 21.2% efficiency boosting for rectifier with matching compared to the rectifier without matching at the same input power level. The co-design of antenna and rectifier with matching has been thoroughly investigated in [37].

Table 5.2: Component values of the proposed six-stage RF-DC rectifier.

	L_1	L_2	L_3	L_4	L_5
Meas.	4.35 nH	9.3 nH	30 nH	9.3 nH	39 nH
Sim.	3.3 nH	9.1 nH	27 nH	9.1 nH	36 nH
	L_6	L_7	L_8	C_1	C_2
Meas.	13 nH	7.5 nH	7.5 nH	200 pF	0.7 pF
Sim.	12 nH				
	C_3	W_{TL1}	L_{TL1}	W_{TL2}	L_{TL2}
Meas. Sim.	0.7 pF	1 mm	7 mm	7 mm	6 mm

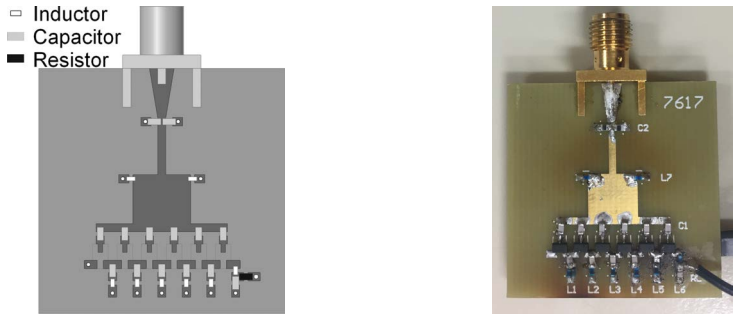

(a) (b)

Figure 5.5: (a) Layout, and (b) photograph of the fabricated rectifier.

5.2 Fabrication and Measurement Results

The layout and the fabricated circuit are shown in Fig. 5.5a and Fig. 5.5b, respectively. The white rectangle in Fig. 5.5a represents the SMD inductor of 0402 series, the grey rectangle denotes the SMD capacitor of 0603 series, and the black rectangle represents the SMD resistor of 0603 series. The size of the proposed rectifier circuit is 30 mm $\times$ 30 mm, and the load resistor is fixed to 15 KΩ. Fig. 5.6a plots the measured input return loss, and the measurement is different from the simulation under the same LC component values.

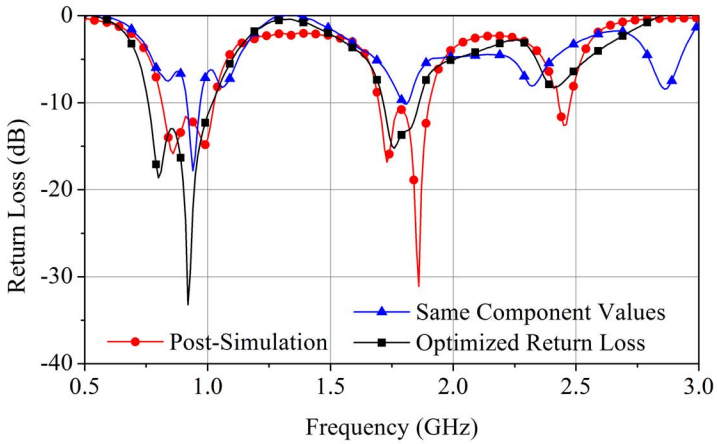

(a)

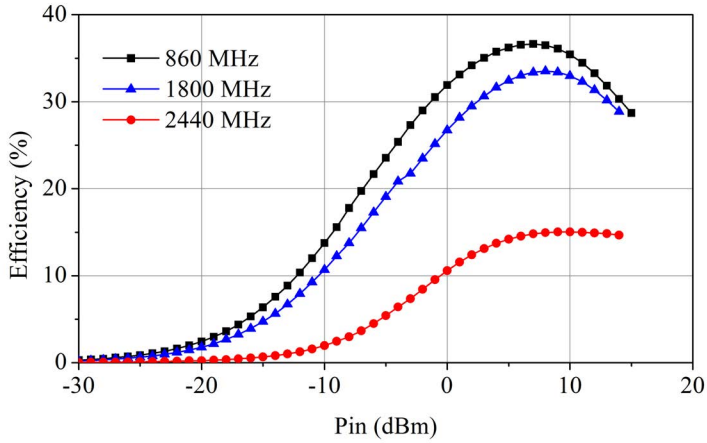

(b)

Figure 5.6: (a) Measured return loss, and measured efficiency at (b) 860 MHz, (c) 1800 MHz, and (d)2440 MHz.

The discrepancy between measurement and simulation is mainly due to the real parasitic capacitance and the reference plane of the diode model, but the resonance frequency can be tuned back by changing $L_1 - L_6$ values. The optimized return loss is < -10 dB in $760-1020$ MHz and $1.71-1.87$ GHz ranges and is < -7 dB in $2.4-2.48$ GHz, as shown in Fig. 5.6a. The measured efficiency with single frequency tone at 860 MHz, 1800 MHz, and 2440 MHz is depicted in Fig. 5.6b. The peak efficiency is 36.6% at 860 MHz, 33.5% at

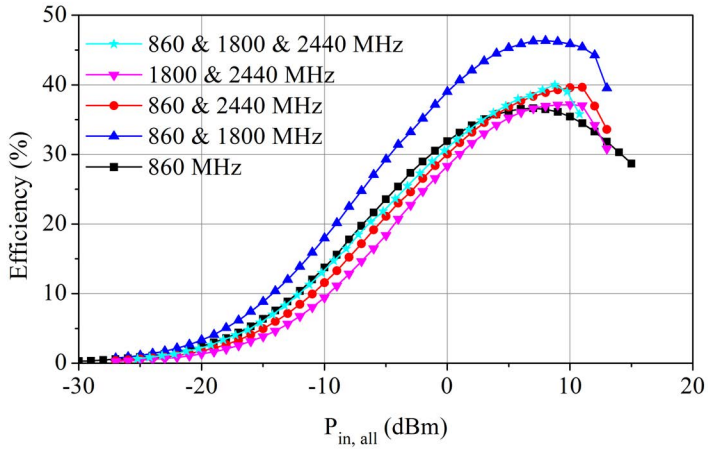

(a)

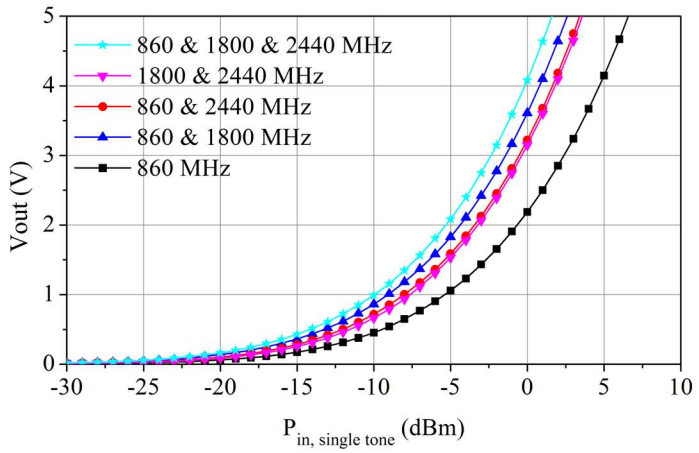

(b)

Figure 5.7: (a) Measured return loss, and measured efficiency at (b) 860 MHz, (c) 1800 MHz, and (d)2440 MHz.

1800 MHz, and 15.0% at 2440 MHz, respectively. The rectifier efficiency is boosted with dual frequency tones at 860/1800 MHz, and the peak efficiency reaches 46.3% as shown in Fig. 5.7a. The measured efficiency with triple frequency tones at 860/1800/2440 MHz is roughly equal to the measurement at 860-MHz single tone. The maximum efficiency drop with dual frequency tones at 860/2440 MHz or 1800/2440 MHz is less than 5.2% compared to single-tone operation at 860 MHz.

Table 5.3: Measured efficiency and sensitivity at V_{out} = 1 V.

Number of Tones	Frequency (MHz)	Efficiency (%)	P_{in} (dBm/tone)	$P_{in,all}$ (mW)
Single	820	21.77	-5.14	0.31
	860	22.90	-5.36	0.29
	920	23.17	-5.41	0.29
	1700	20.55	-4.89	0.32
	1800	18.96	-4.54	0.35
	1900	15.31	-3.61	0.44
	2400	10.84	-2.11	0.62
	2440	9.14	-1.37	0.73
	2480	7.41	-0.46	0.90
Dual	860/1800	26.78	-9.05	0.25
	860/2440	21.03	-8	0.32
	1800/2440	19.27	-7.62	0.35
Triple	860/1800/2440	21.92	-9.94	0.30

The rectifier's capability of multitone operation relieves the sensitivity requirement for RF energy harvesting. Fig. 5.7b presents the DC output voltage at the load resistor (V_{out}), and the rectifier sensitivity is improved up to 5 dB with the same V_{out} for triple inputs operation. Table 5.3 lists the required input power of each frequency tone to generate 1-V DC output voltage (V_{out} = 1 V) and the corresponding efficiency. The measured efficiency is 22.9% and the input power reaches 0.29 mW when V_{out} = 1 V for single-tone operation at 860 MHz, however, the measured efficiency increases to 26.78% with 0.25 mW total input power for 860/1800 dual-tone operation under the same output condition. Even the triple-tone operation obtains lower efficiency and requires higher total input power, the rectifier sensitivity still improves 4.58 dB.

5.3 Conclusions

A six-stage triple-band and wideband RF-DC rectifier is proposed. Multiband characteristic is generated by inserting LC matching at the output of Dickson charge pump. Wideband feature is created by generating two resonances which are close to each other. The effect of capacitance on return loss bandwidth is investigated, and the improvement of rectifier sensitivity with LC matching is analyzed. The optimized return loss is < -10 dB in $760-1020$ MHz and $1.71-1.87$ GHz ranges and is < -7 dB in $2.4-2.48$ GHz. The measured peak power conversion efficiency with single frequency tone is 36.6% at 860 MHz, 33.5% at 1800 MHz, and 15.0% at 2440 MHz, respectively. The power conversion efficiency is boosted with dual frequency tones at 860/1800 MHz, and the peak value reaches 46.3%. The measured power conversion efficiency is 22.9% with 0.29-mW input power when V_{out} = 1 V for single-tone operation at 860 MHz, however, the measured power conversion efficiency increases to 26.78% with 0.25-mW total input power for 860/1800 dual-tone operation under the same output condition. Even the triple-tone operation obtains lower efficiency and requires higher total input power, the rectifier sensitivity still improves 4.58 dB compared to single-tone operation at 860 MHz. The rectifier's capability of multitone operation relieves the sensitivity requirement for RF energy harvesting.

6. DEMONSTRATION OF MULTIBAND RF ENERGY HARVESTING AND TRANSFER

6.1 Experimental Results

This section demonstrates the performance of RF energy transmitting and harvesting with the proposed mutual coupling compensated linear antenna arrays and the proposed six-stage LC matched RF-DC rectifier. The demo purpose is to mimic the entire energy flow from RF energy transmitter to local IoT sensors. The measurement setup is shown in Fig. 6.1. Three signal generators (Agilent E8267D, E4432B, and N5171B) are served as triple frequency tones at 860 MHz, 1800 MHz, and 2440 MHz, respectively. Three power spliters (Mini Circuits ZFSC-2-372-S+) are used to combine triple frequency tones. Three power amplifiers (Mini Circuits ZHL-2010+, ZRL-2300+, and ZRL-3500+) are inserted between signal generators and power spliters to amplify signal amplitude. The source power level is tuned to 10 mW for each frequency tone (P_{source} = 10 mW/tone), and the source power is fed to the transmitting antenna. Multiband operation is verified by feeding single frequency tone (P_{source} = 10 mW), dual frequency tones (P_{source} = 20 mW), or triple frequency tones (P_{source} = 30 mW) to the transmitting antenna. The radiated power pass through the lossy air path and then be captured by the receiving antenna. The captured RF power is rectified and consumed by the resistive load (P_{out}). The demonstration here sets the load resistor to 15 KΩ.

Table 6.1 summarizes the continuous power consumed by 15-KΩ load with different antenna combinations at both transmitting and receiving sides. The antenna at transmitting or receiving side can be either the single double-ring monopole (Single Antenna), the proposed two-element antenna array (Array of 2 Antennas), or the proposed four-element antenna array (Array of 4 Antennas). In Table 6.1, the setup A (Reference) use the single

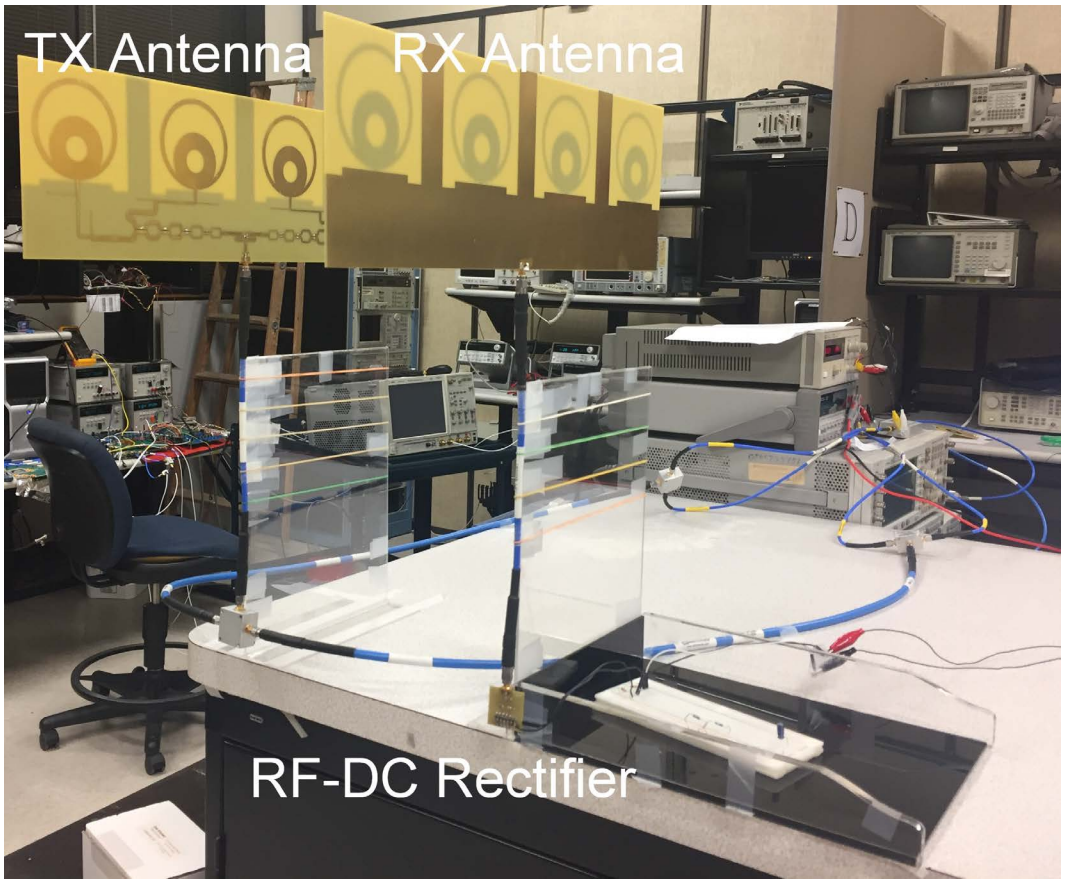

Figure 6.1: Measurement setup.

antenna at both transmitting and receiving sides. Setup B and C (RF Energy Transfer) use antenna array for directive antenna gain at the transmitting side and use omnidirectional antenna for unconstrained sensor placement at the receiving side. In contrast, setup D and E (RF Energy Harvesting) use omnidirectional antenna to mimic ambient RF sources at the transmitting side and use antenna array for higher antenna gain at the receiving side. The bold text in Table 6.1 means that the measured power consumed by the load in a particular setup is equal or better than the measurement in Setup A.

RF energy harvesting/transmitting at operating frequency above 3 GHz is naturally unfavorable due to both low power conversion efficiency of RF-DC rectifier and air path

Table 6.1: Performance of RF Energy Harvesting/Transfer

Setup			A	B	C	D	E
TX Antenna			Single Antenna	Array of 2 Antennas	Array of 4 Antennas	Single Antenna	Single Antenna
RX Antenna			Single Antenna	Single Antenna	Single Antenna	Array of 2 Antennas	Array of 4 Antennas
P_{source} (mW)	Frequency (MHz)	Distance (cm)	Reference P_{out} (μW)	**RF Energy Transmitting** P_{out} (μW)		**RF Energy Harvesting** P_{out} (μW)	
10	860	30	19.95	15.75	7.09	7.13	13.38
		60	1.08	**2.83**	**3.65**	0.38	0.66
		120	0.052	0.013	**0.265**	0.010	**0.138**
	1800	30	0.68	**2.41**	**1.48**	**2.02**	**1.22**
		60	0.17	**0.48**	**0.61**	**0.45**	**0.91**
		120	0.00073	**0.015**	**0.038**	**0.011**	**0.06**
	2440	30	0.047	0.029	**0.052**	0.031	**0.091**
		60	0.0012	**0.0020**	**0.0054**	**0.0024**	**0.0108**
		120	0.00042	**0.00042**	**0.00202**	**0.00049**	**0.00427**
20	860/1800	30	24.81	**25.05**	13.02	14.23	19.95
		60	2.16	**5.30**	**6.70**	1.71	**3.20**
		120	0.068	0.06	**0.54**	0.042	**0.401**
	860/2440	30	21.97	16.93	8.64	8.26	15.81
		60	1.16	**2.97**	**4.03**	0.46	0.91
		120	0.064	0.017	**0.327**	0.015	**0.202**
	1800/2440	30	1.20	**3.05**	**2.21**	**2.67**	**2.11**
		60	0.21	**0.55**	**0.76**	**0.52**	**1.14**
		120	0.002	**0.019**	**0.06**	**0.015**	**0.101**
30	860/1800/2440	30	26.46	26.46	14.79	15.75	22.27
		60	2.21	**5.49**	**7.13**	1.82	**3.59**
		120	0.082	0.068	**0.627**	0.052	**0.505**

loss. Referring from Fig. 5.6b, the measured single-tone power conversion efficiency at 2440 MHz is 4 dB less than the efficiency at 860 MHz when V_{out} = 1 V. Air path loss is more severe and it is proportional to the operating frequency and the distance between transmitting and receiving antennas:

$$APL \propto 20log(d) + 20log(f) \tag{6.1}$$

where APL is the air path loss (in dB), d is the distance between transmitting and receiving antennas (in meter), and f is the signal frequency (in MHz). As setups A−E shown in

Table 6.1, P_{out} at 2440 MHz is at least 13.3 times smaller than P_{out} at 860 MHz or 1800 MHz.

Dual-tone or triple-tone operations nonlinearly boosts P_{out} in all cases (Setup A$-$E). In Table 6.1, the summed P_{out} with 860-MHz single tone and 1800-MHz single tone is less than P_{out} with 860/1800-MHz dual tones. Even if P_{out} is negligible with 2440-MHz single tone, P_{out} increment with 860/2440-MHz dual tones is at least 26.6 times higher than P_{out} with 2440-MHz single tone. As a result, the proposed system can provide nonlinearly boosted output power in a multitone environment.

System measurement results in Table 6.1 state that not only the antenna gain but also the radiation pattern affects the total captured RF power. Referring from the measured realized gain at 1800 MHz in Table 4.5, single antenna achieves 1.73 dBi, two-element antenna array achieves 3.58 dBi, and four-element antenna array achieves 7.52 dBi. However, setup A equipped with single antennas achieves higher P_{out} than setup B$-$E at 30 cm distance. This discrepancy from Friis transmission equation is due to the shape of radiation patterns at both transmitting and receiving sides. The entire energy flow is not only determined by maximum realized gain or 3 dB beamwidth.

Setup A, Setup B, and Setup C are tested for RF energy transmitting application. Comparisons between Setup A and Setup C at distance of 60 cm and 120 cm indicate that using four-element array with directive gain at the transmitting side achieves higher P_{out} than using single antenna with omnidirectional gain. Similarly, comparisons between Setup A and Setup B shows that using two-element array at the transmitting side achieves higher P_{out} at distance of 60 cm and 120 cm with 860-MHz or 2440-MHz single tone or 860/2440-MHz dual tones.

Setup A, Setup D, and Setup E are tested for RF energy harvesting application. Comparisons between Setup A and Setup E at distance of 60 cm and 120 cm suggest that using four-element array at the receiving side receives higher P_{out} if the antenna array is prop-

erly aligned to RF sources. Similarly, comparisons between Setup A and Setup D shows that using two-element array at the receiving side receives higher P_{out} at distance of 60 cm and 120 cm with 860-MHz or 2440-MHz single tone or 860/2440-MHz dual tones.

Table 6.2 compares the proposed RF energy harvesting/transmitting system with previously published works. The proposed antenna array is implemented on cheap and lossy FR-4 material but yet achieves realized gain of $3.0-7.7$ dBi in $0.82-2.48$ GHz range. Moreover, the proposed antenna array applies mutual coupling compensation to synthesize radiation patterns in triple frequency bands. The co-designed 6-stage RF-DC rectifier uses LC matching at each output stage to achieve both multiband and wideband features. The rectifier sensitivity and efficiency is further boosted with dual or triple frequency tones. To the best of author's knowledge, the proposed array is the first work tackling mutual coupling compensation for triple-band operation.

Table 6.2: Comparison with Previously Published Works

Work		TMTT 2016 [34]	AWPL 2016 [35]	TMTT 2017 [2]	IMS 2013 [36]	**This Work**
Substrate Material		FR-4 $tan\delta = 0.01$	Rogers 4350B $tan\delta$ =3.7E-3	FR-4 1.0T	**ROGER4003 $tan\delta = 0.003$	FR-4 $tan\delta = 0.021$
Frequency Band		single	single	single	triple	**triple**
Operating Frequency		868 MHz	5.8 GHz	2.45 GHz	0.94 GHz, 1.95 GHz, 2.44 GHz	**0.86 GHz, 1.8 GHz, 2.44 GHz**
Antenna	Topology	single antenna	1×4 array	1×4 array	single antenna	**1×4 array**
	Combiner	×	RF	hybrid	×	**RF**
	Mutual Coupling Compensation	×	No	No	×	**Yes**
	S_{11} Bandwidth	17.2%	4.80%	3.20%	∼ 4.3%, ∼ 10.3%, ∼ 36.5%	**18.4%, 44.2%, 26.5%**
	Gain	2 dBi	not reported	6.6−9.7 dBi	not reported	**3.0−7.7 dBi**
	3 dB Beamwidth	not reported	39.3°	not reported	not reported	**15°−41°**
	Size	not reported	30×129 mm^2	100×240 mm^2	90×40 mm^2 (∼0.50λ×0.22λ)	147×456 mm^2 (∼0.74λ×2.3λ)
Rectifier	Diode	HSMS-285C	HSMS-2860	HSMS-2852	HSMS-285C	HSMS-285C
	Topology	1-stage Dickson	single diode	1-stage Dickson	4-stage output LC matched Dickson	**6-stage output LC matched Dickson**
	S_{11} Bandwidth	8.50%	not reported	∼ 4−12.2%	∼ 12.5%, ∼ 10%, ∼ 6.2%	**29.2%, 8.1%, ****6.2%**
	PCE	44.2% at P_{in}=−10 dBm	70.1% at P_{in}=15.2 dBm	55.3% at P_{in}=−4 dBm	80% at P_{in}=10 dBm, f=0.94 GHz; 47% at P_{in}=8 dBm, f=1.95 GHz; 43% at P_{in}=16 dBm, f=2.44 GHz	46.3% at dual tones: P_{in}=5 dBm, f=0.86 GHz; P_{in}=5 dBm, f=1.8 GHz
	Load	9.53 KΩ	400 Ω	10 MΩ−6.2 KΩ	12 KΩ	15 KΩ
	V_{out}	649 mV at P_{in}=−10 dBm	not reported	not reported	not reported	**1 V at triple tones: P_{in}=−9.9 dBm/tone**
Rectenna	Distance	not reported	not reported	5 m	***90−150 cm	30−120 cm
	P_{source} or P_{in} Density	0.1 μW/cm^2	1.276 mW/cm^2	1 W	10 mW/tone	10 mW/tone
	Output	*1.97 V at 3×1 rectenna array	∼ 25 mW	∼ 0.1 mW	7.06 μW at triple tones	Setup C: 0.6−14.8 μW Setup E: 0.5−22.3 μW

*: measured with open circuit load. **: rectifier is fabricated on FR-4 substrate ($tan\delta = 0.02$). ***: 0.94-GHz source at 150 cm, 1.95-GHz source at 120 cm, and 2.44-GHz source at 90 cm. ****: −6 dB return loss bandwidth.

6.2 Conclusions

Four-element antenna array is preferable to be installed at the transmitting side for RF energy transfer because of directive power radiation, while the omnidirectional antenna is preferable to be installed at the receiving side for both RF energy harvesting and transfer in consideration of IoT sensor size and physical placement. However, in the application such as bridge monitoring where plenty of receiving area is available, the rectenna array composed of four-element arrays and RF-DC rectifiers can be applied for RF energy harvesting.

7. SUMMARY AND FUTURE WORK

A multiband RF energy harvesting/transfer system consisted of mutual coupling compensated linear antenna arrays and six-stage LC matched RF-DC rectifier is presented. The system is designed to operate in standard communication bands such as GSM850, GSM900, GSM1800, GSM1900, WiFi, Bluetooth, and LTE since ample RF ambient signals are present and numerous IoT sensors are operated in these frequency bands.

Chapter 2 shows a highly efficient double-ring monopole antenna. The proposed antenna has both wideband and multiband features to cover the target operating frequencies. Multiband feature is created by two annular rings, and wideband feature is inherent from monopole topology. The design tradeoff of antenna geometry versus return loss bandwidth is investigated, and the total efficiency is preserved while achieving a compact size.

Chapter 3 presents a four-way RF energy combiner to connect up to four antenna elements with equiphase and equimagnitude inputs. The proposed combiner is composed of one Wilkinson combiner, two broadband Wilkinson combiners, and two quarter-wavelength interconnection lines. The building block selection between Wilkinson combiner or broadband Wilkinson combiner is compared, and the electrical length of interconnection line is analyzed for maximum power combining efficiency.

Chapter 4 shows how to synthesize triple-band radiation patterns in monopole arrays by mutual coupling compensation. Mutual coupling compensated linear arrays of two/four double-ring monopoles are proposed to enhance the captured/radiated RF power. Ground baffles are inserted between antenna elements to compensate mutual coupling, while the effective gain is defined to determine the optimum antenna spacing. Radiation patterns at both multiband and wideband frequencies are synthesized at the cost of return loss matching at base antenna terminals, and base antenna elements are re-matched to 50Ω by

broadband matching network and four-way RF energy combiner.

Chapter 5 presents a six-stage triple-band and wideband RF-DC rectifier. Multiband characteristic is generated by inserting LC matching at the output of Dickson charge pump, while wideband feature is created by generating two resonances which are close to each other. The effect of capacitance on return loss bandwidth is investigated, and the improvement of rectifier sensitivity with LC matching is analyzed. The power conversion efficiency is boosted with dual frequency tones compared to single-tone operation.

Finally, Chapter 6 demonstrates triple-band RF energy harvesting/transfer measurement results with the proposed double-ring monopole arrays and RF-DC rectifier. Different antenna setups at transmitting and receiving sides are tested, and the measurement results show that not only the antenna gain but also the radiation pattern affects the total captured RF power. Generally, array of four elements is favorable to be installed at the transmitting side for RF energy transfer, while the single antenna is preferable to be installed at the receiving side for RF energy harvesting. If the receiving area is not limited, then the rectenna array composed of four-element arrays and RF-DC rectifiers can be applied for RF energy harvesting.

The future works include three parts: the investigation on mutual coupling compensated patch antenna array for more directive array gain, the integrated circuit implementation on multiband LC matched RF-DC rectifier, and the research on beam steering control circuit and phase shifter for RF energy transfer. Implement antenna arrays on transparent and flexible substrate material is also another popular research aspect.

REFERENCES

[1] S. Kitazawa, H. Ban, and K. Kobayashi, "Energy Harvesting from Ambient RF Sources," in *IEEE IMWS-IWPT2012*, pp. 39–42, Oct. 2012.

[2] D.-J. Lee, S.-J. Lee, I.-J. Hwang, W.-S. Lee, and J.-W. Yu, "Hybrid Power Combining Rectenna Array for Wide Incident Angle Coverage in RF Energy Transfer," *IEEE Trans. Microw. Theory Techn.*, vol. pp, no. 99, pp. 1–11, 2017.

[3] J. Zhou, K. A. Morris, and M. J. Lancaster, "General Design of Multiway Multi-section Power Dividers by Interconnecting Two-Way Dividers," *IRE Trans. Microw. Theory Techn.*, vol. 55, no. 10, pp. 2208–2215, 2007.

[4] S. B. Cohn, "A Class of Broadband Three-Port TEM-Mode Hybrids," *IEEE Trans. Microw. Theory Techn.*, vol. 16, no. 2, pp. 110–116, 1968.

[5] P. Middleton, P. Kjeldsen, and J. Tully, "Forecast: The Internet of Things," tech. rep., Gartner, 2013.

[6] H. J. Visser, A. C. Reniers, and J. A. Theeuwes, "Ambient RF Energy Scavenging: GSM and WLAN Power Density Measurements," in *IEEE European Microwave Conference*, pp. 721–724, Oct. 2008.

[7] S. Kim, R. Vyas, J. Bito, K. Niotaki, A. Collado, A. Georgiadis, and M. M. Tentzeris, "Ambient RF Energy-Harvesting Technologies for Self-Sustainable Standalone Wireless Sensor Platforms," *Proceedings of the IEEE*, vol. 102, pp. 1649–1666, Nov. 2014.

[8] M.-Y. Huang, T. Chi, F. Wang, and H. Wang, "An all-passive negative feedback network for broadband and wide field-of-view self-steering beam-forming with zero dc power consumption," *IEEE J. Solid-State Circuits*, vol. pp, no. 99, pp. 1–14, 2017.

[9] J. A. Hagerty, F. B. Helmbrecht, W. H. McCalpin, R. Zane, and Z. B. Popović, "Recycling Ambient Microwave Energy With Broad-Band Rectenna Arrays," *IEEE Trans. Microw. Theory Techn.*, vol. 52, pp. 1014–1024, Mar. 2004.

[10] B. L. Pham and A.-V. Pham, "Triple Bands Antenna and High Efficiency Rectifier Design for RF Energy Harvesting at 900, 1900 and 2400 MHz," in *IEEE MTT-S Int. Microw. Symp. Dig.*, pp. 1–3, June 2013.

[11] H. Saghlatoon, T. B. Baghini, L. Sydänheimo, M. M. Tentzeris, and L. Ukkonen, "Inkjet-Printed Wideband Planar Monopole Antenna on Cardboard for RF Energy-Harvesting Applications," *IEEE Antennas Wireless Propag. Lett.*, vol. 14, pp. 325–328, Feb. 2015.

[12] M. Arrawatia, M. S. Baghini, and G. Kumar, "Broadband Bent Triangular Omnidirectional Antenna for RF Energy Harvesting," *IEEE Antennas Wireless Propag. Lett.*, vol. 15, pp. 36–39, Feb. 2016.

[13] K. Niotaki, SangkilKim, S. Jeong, A. Collado, A. Georgiadis, and M. M. Tentzeris, "A Compact Dual-Band Rectenna Using Slot-Loaded Dual Band Folded Dipole Antenna," *IEEE Antennas Wireless Propag. Lett.*, vol. 12, pp. 1634–1637, Dec. 2013.

[14] M. Aboualalaa, A. B. Abdel-Rahman, A. Allam, H. Elsadek, and R. K. Pokharel, "Design of Dual Band Microstrip Antenna with Enhanced Gain for Energy Harvesting Applications," *IEEE Antennas Wireless Propag. Lett.*, vol. PP, pp. 1–4, Jan. 2017.

[15] J. Pourahmadazar, C. Ghobadi, J. Nourinia, and H. Shirzad, "Multiband Ring Fractal Monopole Antenna for Mobile Devices," *IEEE Antennas Wireless Propag. Lett.*, vol. 9, pp. 863–866, Sept. 2010.

[16] M. A. Abouzied and E. Sánchez-Sinencio, "Low-Input Power-Level CMOS RF Energy-Harvesting Front End," *IEEE Trans. Microw. Theory Techn.*, vol. 63,

pp. 3794–3805, Nov. 2015.

[17] O. Elsayed, M. Abouzied, and E. Sánchez-Sinencio, "A 540 W RF Wireless Receiver Assisted by RF Blocker Energy Harvesting for IoT Applications with +18 dBm OB-IIP3," in *IEEE RFIC Symp. Dig.*, pp. 230–233, July 2016.

[18] M. A. Abouzied, K. Ravichandran, and E. Sánchez-Sinencio, "A Fully Integrated Reconfigurable Self-Startup RF Energy-Harvesting System With Storage Capability," *IEEE J. Solid-State Circuits*, vol. PP, pp. 1–16, Dec. 2016.

[19] G. Kumar and K. P. Ray, *Broadband Microstrip Antennas*. Norwood, Massachusetts: Artech House, 2002.

[20] E. J. Wilkinson, "An N-Way Hybrid Power Divider," *IRE Trans. Microw. Theory Techn.*, vol. 8, no. 1, pp. 116–118, 1960.

[21] H. T. Hui, "A New Definition of Mutual Impedance for Application in Dipole Receiving Antenna Arrays," *IEEE Antennas Wireless Propag. Lett.*, vol. 3, pp. 364–367, Sept. 2004.

[22] H.-S. Lui, H. T. Hui, and M. S. Leong, "A Note on the Mutual-Coupling Problems in Transmitting and Receiving Antenna Arrays," *IRE Trans. Microw. Theory Techn.*, vol. 51, pp. 171–176, Oct. 2009.

[23] H. T. Hui, "Mutual Coupling in Antenna Arrays," tech. rep., National University of Singapore, 2014.

[24] I. J. Gupta and A. A. Ksienski, "Effect of mutual coupling on the performance of adaptive arrays," *IEEE Trans. Antennas Propag.*, vol. 31, pp. 785–791, Sept. 1983.

[25] S. Henault, S. K. Podilchak, S. M. Mikki, and Y. M. M. Antar, "A Methodology for Mutual Coupling Estimation and Compensation in Antennas," *IEEE Trans. Antennas Propag.*, vol. 61, pp. 1119–1131, Mar. 2013.

[26] S. Edelberg and A. A. Oliner, "Mutual Coupling Effects in Large Antenna Arrays II: Compensation Effects," *IRE Trans. Antennas Propag.*, vol. 8, pp. 360–367, July 1960.

[27] M. M. Bait-Suwailam, O. F. Siddiqui, and O. M. Ramahi, "Mutual Coupling Reduction Between Microstrip Patch Antennas Using Slotted-Complementary Split-Ring Resonators," *IEEE Antennas Wireless Propag. Lett.*, vol. 9, pp. 876–878, Sept. 2010.

[28] Q. Li, A. P. Feresidis, M. Mavridou, and P. S. Hall, "Miniaturized Double-Layer EBG Structures for Broadband Mutual Coupling Reduction Between UWB Monopoles," *IEEE Trans. Antennas Propag.*, vol. 63, pp. 1168–1171, Mar. 2015.

[29] J. D. Fredrick, Y. Wang, and T. Itoh, "Smart Antennas Based on Spatial Multiplexing of Local Elements (SMILE) for Mutual Coupling Reduction," *IEEE Trans. Antennas Propag.*, vol. 52, pp. 106–114, Jan. 2004.

[30] T. S. Almoneef, H. Sun, and O. M. Ramahi, "A 3-D Folded Dipole Antenna Array for Far-Field Electromagnetic Energy Transfer," *IEEE Antennas Wireless Propag. Lett.*, vol. 15, pp. 1406–1409, Dec. 2015.

[31] F. Erkmen, T. S. Almoneef, and O. M. Ramahi, "Electromagnetic Energy Harvesting Using Full-Wave Rectification," *IEEE Trans. Microw. Theory Techn.*, vol. pp, no. 99, pp. 1–9, 2017.

[32] M. Piñuela, P. D. Mitcheson, and S. Lucyszyn, "Ambient RF Energy Harvesting in Urban and Semi-Urban Environments," *IEEE Trans. Microw. Theory Techn.*, vol. 61, pp. 2715–2726, July 2013.

[33] J. D. Fredrick, Y. Wang, and T. Itoh, "Hybrid FSS and Rectenna Design for Wireless Power Harvesting," *IEEE Trans. Antennas Propag.*, vol. 64, pp. 2038–2042, May 2016.

[34] S. D. Assimonis, S.-N. Daskalakis, and A. Bletsas, "Sensitive and Efficient RF Harvesting Supply for Batteryless Backscatter Sensor Networks," *IEEE Trans. Microw. Theory Techn.*, vol. 64, pp. 1327–1338, Apr. 2016.

[35] H. Sun and W. Geyi, "A New Rectenna Using Beamwidth-Enhanced Antenna Array for RF Power Harvesting Applications," *IEEE Antennas Wireless Propag. Lett.*, vol. pp, pp. 1–4, Dec. 2016.

[36] B. L. Pham and A.-V. Pham, "Triple bands antenna and high efficiency rectifier design for rf energy harvesting at 900, 1900 and 2400 mhz," in *IEEE MTT-S Int. Microw. Symp. Dig.*, pp. 1–3, June 2013.

[37] M. Stoopman, S. Keyrouz, H. J. Visser, K. Philips, and W. A. Serdijn, "Co-design of a cmos rectifier and small loop antenna for highly sensitive rf energy harvesters," *IEEE J. Solid-State Circuits*, vol. 49, pp. 622–634, Mar. 2014.